June
2019

The Use of Common-Offset and Multiple-Offset GPR methods for Forensic Investigations

BSC APPLIED EARTH SCIENCE – BACHELOR END PROJECT

FREDERIKKE STORM HANSEN (4531639)

IN COOPERATION WITH	CLAIRE MULDER (4435729)
SUPERVISORS TU DELFT	DR.IR. D.J.M. NGAN-TILLARD
	DR.IR. D.S. DRAGANOV
SUPERVISOR NFI	W.C. NIENABER

Abstract

This thesis is part of a longer series of research into the use of geophysical methods for investigation for forensic purposes, a collaboration between the Delft University of Technology (TU Delft) and the Netherlands Forensic Institute (NFI). In this investigation, the difference between a grave containing a human body and a refilled empty pit is explored at the Amsterdam Research Initiative for Subsurface Taphonomy and Anthropology (ARISTA) facility, using common-offset GPR data collection. In addition, common-offset data is gathered at a test site at TU Delft, in order to redefine the locations of previously buried targets. Multiple-offset GPR datasets are also collected at both sites, one of which is processed using electromagnetic interferometry (EMI) and adaptive subtraction (AS) in an attempt to remove direct waves.

The positions of the targets at the TU Delft site were redefined, but with some questions as to whether the site has been altered in the past year without the knowledge of the author. High levels of interference in the ARISTA facility data due to close proximity to various metal and plastic objects makes it difficult to determine the true differences caused by the presence of the cadaver. The author suggests using a 500-MHz antenna for further investigations at the site due to high wave velocity which leads to a low resolution when using a 250-MHz antenna, and due to more homogeneous soil at the ARISTA facility. The optimal procedure for EMI+AS is discussed, and suggested to be the use of a bandpass filter to remove very high and low frequencies from the raw data prior to EMI. The method is shown to be reasonably effective, especially when the data is strongly impacted by the presence of direct waves, where simply topmuting the data would remove too much information. A script was prepared in MATLAB which has been optimised for the application of EMI to GPR data, and further scripts were prepared for use in Seismic Unix for the purpose of AS, in the hopes that others may find these a useful beginning to further applications of this method.

Preface

This report constitutes a continuation of previous work on the use of geophysical surveying tools for forensic analysis of the shallow subsurface, and builds upon research performed in 2018 by Koen Harms and Annika Vroom. The data acquisition was carried out with the help of Claire Mulder, who has produced a separate report with the results of her analysis, which mainly concerns electrical resistivity surveying. Dominique Ngan-Tillard and Deyan Draganov were the supervisors for this investigation, and Coen Nienaber was our contact from the Netherlands Forensic Institute.

The data collection described in this thesis is extensive, and some of the data was not analysed due to time constraints. This additional data will be placed on the TU Delft data repository *4TU – Centre for Research Data* such that anyone may continue the research.

We would like to thank Coen, Dominique, and Deyan for the opportunity to partake in this project, and for all the help they offered during the data acquisition and processing. In addition, Florencia Balestrini and Jianhuan Liu supported this project by providing scripts for applying electromagnetic interferometry and adaptive subtraction, and guiding us through the editing of these such that they suited our project. We would like to extend special thanks to Juan Chavez Olalla, who spent several hours helping us get acquainted with the equipment, collecting data, and processing the data.

Frederikke Storm Hansen
June 2019

Table of Contents

1. Introduction

Geophysical tools are increasingly proving their benefits to police and forensic investigators as the field of forensic geophysics grows. Clandestinely buried objects or corpses can be detected even by untrained personnel using tools such as ground penetrating radar (GPR) and other electromagnetic instruments (e.g. EM 38 and GEM). These tools are often faster, less invasive, and less expensive alternatives to classical forensic methods such as excavation, as they can narrow down search areas (Killam, 2004). Unfortunately, a scarcity of studies examining the use of these methods precisely for forensic purposes often results in a misunderstanding of the best practices for using the equipment, or even misinterpreted results. Delft University of Technology (TU Delft) therefore began a collaboration with the Netherlands Forensic Institute in 2018 with the goal of developing a new research into the use of geophysical methods for forensic purposes in the Netherlands.

Previous work has been done at the university looking at the responses recorded by GPR, EM 38, and GEM instruments to plastic barrels buried in soil under wet and dry conditions. For the results of these investigations, the reader may refer to the 2018 bachelor theses of Annika Vroom and Koen Harms. This study is a continuation of their work, and will address the use of two GPR setups (common offset and multiple offset) to characterise clandestine burials of human corpses. Research on this topic is very limited, often performed in climates different than that of the Netherlands, or using pig corpses as substitutes for human targets. With regard to the latter, recent work has called into question the appropriateness of this substitution, as the decomposition of pigs differs considerably from that of humans (Hayman & Oxenham, 2016). The Amsterdam Research Initiative for Subsurface Taphonomy and Anthropology (ARISTA) facility opened in 2017, as the first forensic cemetery in Europe, allowing great strides to be made in research on geophysical methods for locating clandestine graves. This investigation will be performed at this facility.

The most common use of the GPR is in common-offset geometry, which allows for easy and quick data collection and simple processing. However, it is also possible to collect multiple-offset data with the GPR, which contains velocity information and offers several other benefits over common-offset data (Berard & Maillol, 2007). In this investigation, both methods will be evaluated. A combination of electromagnetic interferometry (EMI) and adaptive subtraction (AS), which has proven useful for removing direct waves in seismic data using seismic interferometry, will be applied to the multiple-offset GPR data in an attempt to remove the direct waves that often mask the reflections from objects located at shallow depths.

In summary, this investigation will attempt to answer the central research question:

> *How may common-offset GPR and multiple-offset GPR surveys be used*
> *to determine the difference between empty pits and clandestine burials?*

Several sub-questions will be examined in order to answer this research question:

- Which differences in common-offset GPR response are noticeable between a clandestine burial of a human body and a refilled empty pit?
- Which procedure of direct wave isolation prior to EMI, and which AS parameters give the best result of supressed direct waves?
- How effective is the removal of direct waves from multiple-offset GPR data using the principles of EMI and AS?
- What further steps should be taken along this line of research?

In addition to the study at the ARISTA facility, the test site at TU Delft will be investigated using common-offset GPR acquisition in an effort to support the possibilities for long-term research at the site. Though this is not the main focus of this thesis, the results of this additional data collection will be presented and discussed as a way to centralise information for the project as a whole. This “side investigation” will address the following sub-questions:

- How can the locations of the targets at the TU Delft investigation site be redefined according to a new grid?
- What distinctions could be made for the 250-MHz common-offset GPR images in sandy soil vs silty/clayey soil?

The general theory of the GPR will be presented in chapter two, which also contains an introduction to EMI and AS, and human taphonomy. Chapter three describes the sites that have been investigated and the methods used at each location. The fourth chapter explains the data processing and presents the results. Chapter five provides a discussion of the findings, and chapter six concludes the thesis.

2. Theory and Equipment

This chapter outlines the theory behind the methods and equipment used in the investigation. Since taphonomy is an important factor for the exploration at the ARISTA facility, subchapter 2.3 will present some general information on the topic.

2.1 Ground Penetrating Radar

GPR is a popular tool for shallow geophysical investigations due to its non-invasiveness and capacity for real-time data analysis (Pringle, Jervis, Cassella, & Cassidy, 2008).

The principle of GPR is the reflection of electromagnetic pulses at boundaries between objects differing in electric and magnetic properties (Møller, 2006). The most relevant of these properties are electrical conductivity and dielectric permittivity, with magnetic permeability being less important (Daniels, 2004). Waves of a known frequency, usually between 10 to 2000 MHz, are sent into the subsurface by a transmitter, and a receiver records the time taken for the waves to reach it, as well as the amplitude of the received signal. The frequency used for a survey may be chosen based on an initial evaluation and comparison of several options, as the best frequency depends on individual site conditions, including soil type, moisture content, and target material and depth (Pringle et al., 2008). Generally, a higher-frequency antenna will support a higher resolution, as the resolution is theoretically ¼ of the wavelength at a maximum (Møller, 2006), where the wavelength is directly related to the bandwidth of the emitted signal, which is usually equal to the central frequency (Jol, 2009). However, a higher frequency will also attenuate faster and penetrate less deep (Bradford, 2007). GPR gives the best results when used in low-conductivity soils such as dry sands (Hansen, Pringle, & Goodwin, 2014).

Figure 2.1 shows the theoretical common-offset GPR response to a square trench with a pipe in it (Goodman & Piro, 2013). This is assumed to be similar to a trench with a human corpse in it, though the hyperbola in the centre of the image would be larger in the case of a cadaver.

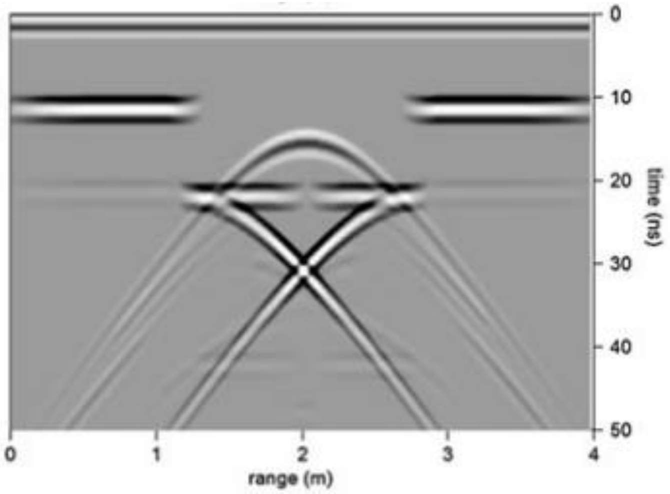

Figure 2.1: Theoretical common-offset GPR response to a square trench with a metal pipe in it (Goodman & Piro, 2013).

Most often, the transmitter and receiver are located in a fixed geometry, the so-called common-offset setup. This setup is easy to use and can be interpreted directly or with minimal processing (Berard & Maillol, 2007). However, several studies show the benefits of using a multiple-offset GPR setup, where multiple receiver positions are used for each transmitter position. Such a setup has the benefits of increased signal to noise ratio and more quantitative information (e.g. velocity data), but has the downside of tedious data acquisition (Berard & Maillol, 2007; Forte & Pipan, 2017). In the processing of multiple-offset data, the principles of EMI and AS may be applied, just as in multiple-offset seismic datasets. The following section provides a brief description of EMI and AS.

2.1.1 Electromagnetic Interferometry and Adaptive Subtraction

Seismic/electromagnetic interferometry is a data-driven method of estimating seismic/electromagnetic responses through the cross-correlation of observations at different receivers (Wapenaar, Draganov, Snieder, Campman, & Verdel, 2010). In the case of observations from separate sources, the cross-correlation is followed by summation over the sources. From this process, each receiver becomes a virtual source, and the response of this virtual source is found at the location of every receiver. In most seismic surveys, the true sources are placed at the surface, so the estimated response retrieved by seismic/electromagnetic interferometry will be dominated by direct waves since these have the highest energy in surface source recordings (Liu, Draganov, & Ghose, 2018). For effective retrieval of a reflector response, the sources should be located in the subsurface (Wapenaar et al., 2010).

Figure 2.2 (a) and (b) illustrate the method of correlation used in this investigation. For a virtual source VS_2 at position R_2, the complex conjugate of the common receiver gather at R_2 (CR_2*) is multiplied element-wise by the common receiver gather at R_1 (CR_1) in the frequency domain. The columns of the resulting matrix (the correlation gather $CG(R_1,R_2)$) are stacked in the time domain to give the response at the receiver R_1 from the virtual source VS_2. This is repeated for every other virtual source and receiver configuration, and the resulting traces are organised in a three-dimensional matrix similar to the one shown in figure 2.2 (a), but with size t x R x R instead of t x R x S due to the R virtual sources.

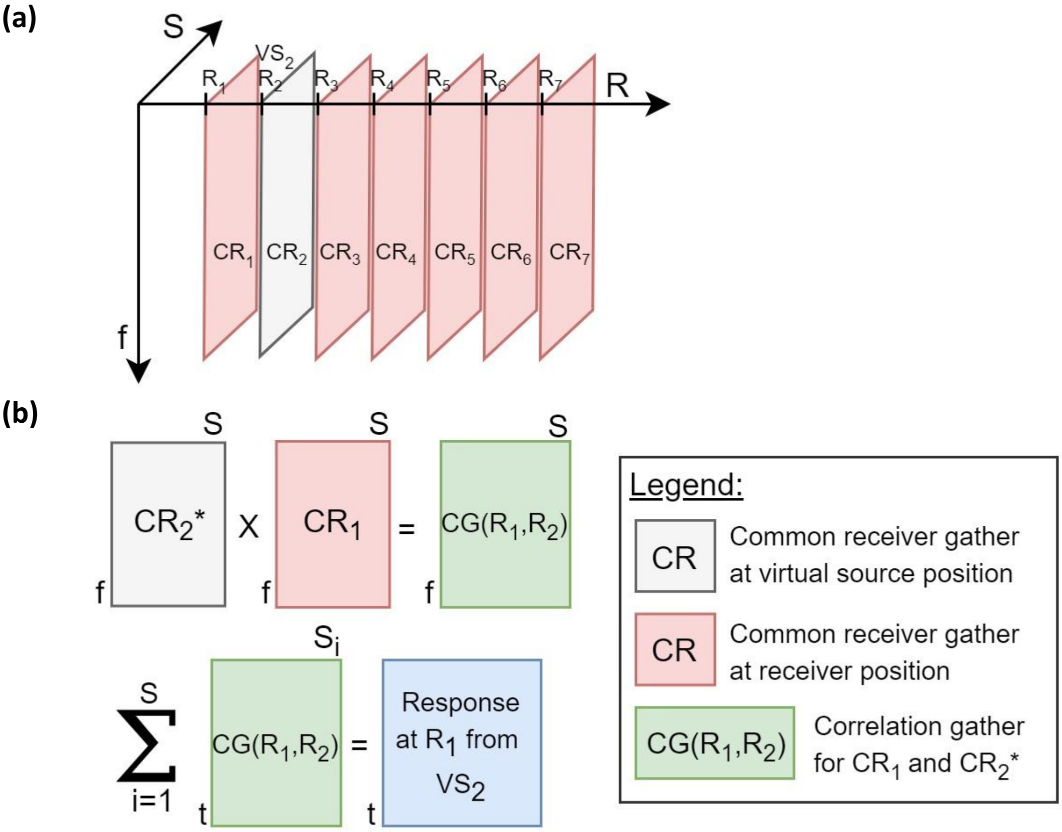

Figure 2.2: (a) Visualisation of common receiver gathers created from a 3D matrix of common source gathers. (b) Visualisation of matrix operations in direct wave EMI.

Seismic/electromagnetic interferometry allows for direct waves to be predicted and subtracted from the original data when used in combination with AS (Dong, He, & Schuster, 2006). In AS, a least-squares fit of the original data is used to approximate the location of the direct wave as retrieved by seismic/electromagnetic interferometry (Konstantaki, Draganov, Ghose, & Heimovaara, 2015; Liu et al., 2018). EMI has previously been applied to GPR data (E. Slob & Wapenaar, 2007; Evert Slob & Wapenaar, 2008), but it has not previously been used in combination with AS for the removal of direct waves in GPR data (D. Draganov, D. Ngan-Tillard, & E. Slob, personal communication, June 2019).

In this investigation, both the common-offset and the multiple-offset setups will be compared, using a PulseEKKO Pro equipped with a 250-MHz antenna. The choice of this frequency was based on the results of the 2018 theses by A. Vroom and K. Harms, and will be further justified in chapter 3 of this thesis. An odometer was used to trigger the measurements.

2.2 Taphonomy

One of the sites investigated as part of this project is the ARISTA facility of the University of Amsterdam Academic Medical Centre (UMC AMC), where human cadavers have been buried for taphonomic research purposes since 2017. For this reason, it is important to consider the state of decomposition of the target, as well as the factors that may influence the decomposition. The study of taphonomy is broad, and attention in this subchapter will mainly be directed toward factors relevant to the situation and period of burial at the ARISTA facility.

Decomposition is influenced by several factors, such as temperature, moisture, soil type, presence of living organisms, and even differences between individual bodies (Schotsmans, Márquez-Grant, & Forbes, 2017). In general, the progression towards complete skeletonization after death is as follows:

Table 2.1: Stages of decomposition (Galloway, Birkby, Jones, Henry, & Parks, 1989; Schotsmans et al., 2017).

Stage	Processes
1	The body reaches ambient temperature (usually cooling) and stiffens in the process. This is called *rigor mortis*, and will pass as the muscle fibres begin to decompose.
2	Breakdown of tissue by microorganisms begins and putrefaction gas generates, manifesting most clearly in the abdomen. Grey, green, and brown discoloration of the flesh occurs.
3	Skin begins to blister and separate from tissue. Fats and soft organs such as the brain begin to liquefy. Skeleton begins to become exposed.
4	Soft tissues (muscles, nerves, etc.) continue to decompose by action of enzymes and microorganisms, as well as insects if these are present.
5	Complete skeletonization, though leathery skin may still be present. Bones continue to become lighter and drier as time passes.

The time taken for each stage varies widely, and the stages are not necessarily distinct from one another, with some studies using pigs finding complete skeletonization of one part of the cadaver and only slight decomposition of the soft tissues elsewhere on the same cadaver (Salsarola et al., 2015). The most important regulators of rate of decomposition are temperature and moisture, with faster decomposition in warmer and wetter regions (Hayman & Oxenham, 2016). As a result of this, clayey soils which retain moisture will promote faster decomposition than sandy soils. However, very wet soils will once again decrease decomposition rate due to lowered gas diffusion and thus aerobic metabolism. In addition, decomposition occurs faster in obese individuals and at slightly alkaline pH.

Most research into taphonomy has been done on pig cadavers, but recent studies reveal differences in the rate of decomposition of human and pig tissues, likely owing to variations in fatty acid composition and nutrient levels (Hayman & Oxenham, 2016). Standardised formulas and scoring systems for estimating the post mortem interval of human remains have been proposed several times, but these prove inaccurate more often than not (Buekenhout, Cravo, Vieira, Cunha, & Ferreira, 2018; Ceciliason, Andersson, Lindström, & Sandler, 2018; Hayman & Oxenham, 2016). Therefore, it is difficult to predict the state of the buried cadavers at the ARISTA facility. Personal communications with C. Nienaber of the Netherlands Forensic Institute suggested the likely state of the body to be around stage 4 to stage 5 as described in table 2.1.

3. Data Collection

This chapter provides a description of the two investigation sites, as well as the set-up used at each site.

3.1 TU Delft Site

The investigation site at the TU Delft was initiated in 2018 with the creation of three test pits. As a continuation of the previous work, 250-MHz common-offset GPR data was collected over a grid, following the recommendations of the authors of the previous theses. In addition to this, the site was used in preparation for the fieldwork to be done at the ARISTA facility, and for the optimisation of the multiple-offset GPR data collection.

3.1.1 Site Description

Figure 3.1 shows the location of the 2018 test area. The three targets comprise one empty, backfilled pit (centred at (4.2,4.2) in figure 3.2), one pit containing an empty plastic barrel (centred at (0.7,0.7)), and one containing a plastic barrel filled with steel rods (centred at (1.7,2.2)), meant to simulate buried weapons. The positions of these are shown in figure 3.2, which also shows the grid surveyed in 2018 (Harms, 2018; Vroom, 2018). The barrels are buried lying down at depths of about 0.35 m, with the top about 5 to 10 cm below the surface. Additional images of and information about the targets may be found in the theses from the 2018 investigation.

Figure 3.1: Location of TU Delft investigation site (Harms, 2018; Vroom, 2018).

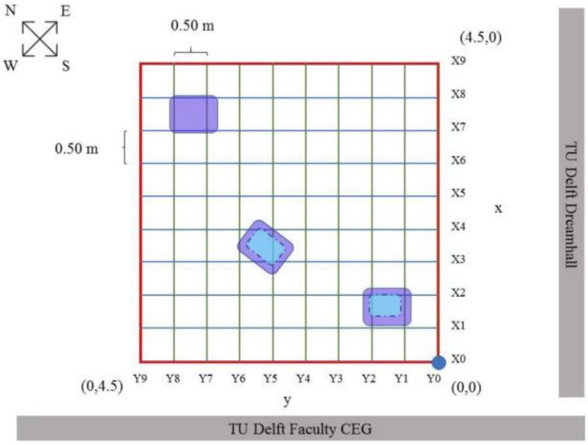

Figure 3.2: Positions of buried targets at TU Delft site (Harms, 2018; Vroom, 2018). Purple rectangles represent trenches, blue rectangles represent barrels. GPR data was acquired along lines X0 to X9 and Y0 to Y9 in 2018.

Unfortunately, the authors of the 2018 theses were unable to locate the exact coordinates of the grid previously created at the site, so a new grid was created for the present investigation. This was done with the help of images taken at the previous investigation, as well as an initial GPR measurement in an attempt to locate the empty barrel. This led to the study area in figure 3.3, which also details measurements from the corners of the grid to nearby pavements and buildings (not to scale). Figure 3.4 shows the coordinates used for this grid, which has a different origin point than that of the 2018 theses. Figure 3.4 also provides the location and coordinates of the electrode grid used for the resistivity survey which was performed during the same data collection, which has the same origin for ease of comparison between the two. The resisitivity data is presented and analysed in the thesis of Claire Mulder. The ERT grid is slightly offset from the GPR grid in an attempt to assure the imaging of the empty barrel target, located at (0.7,0.7) in figure 3.2.

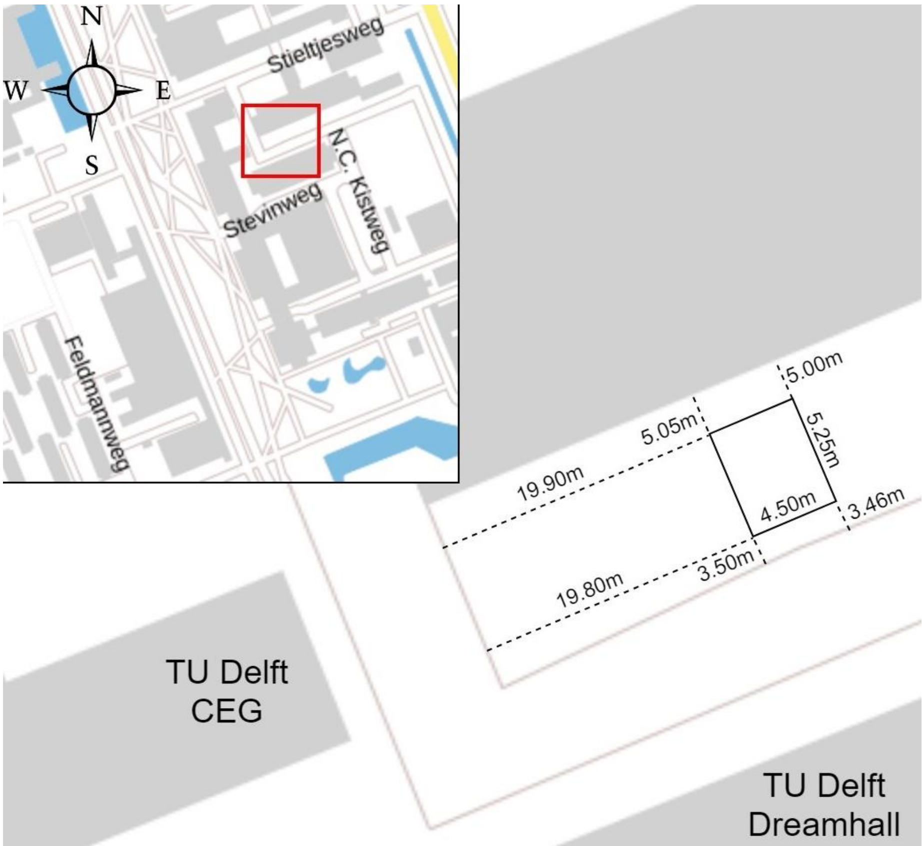

Figure 3.3: Location of the 2019 grid at the TU Delft site, with measurements from adjacent building and roads. Base maps sourced from: (pdok, 2019).

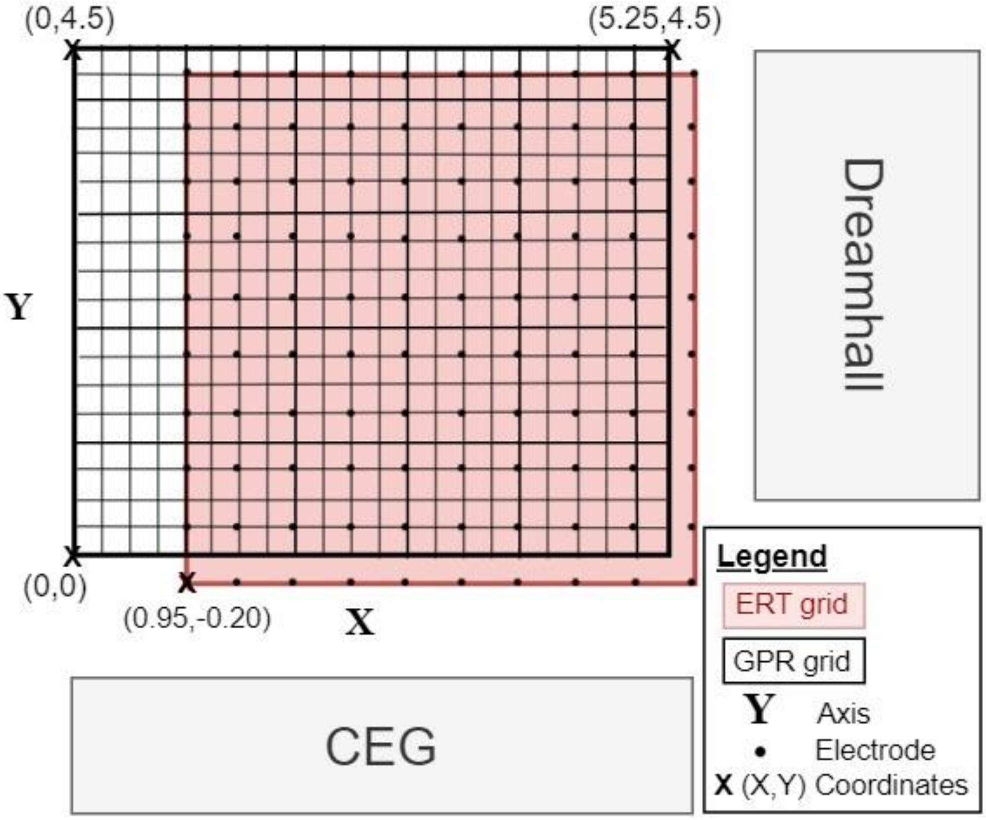

Figure 3.4: Coordinates of the 2019 grid at the TU Delft site. Note the origin point and axes, which are different from the grid used in the 2018 theses (figure 3.2).

According to hand auger analysis from the previous theses, the soil at the site consists primarily of silty sand with increasing peat content from 0% at the surface to about 10% at 1 m depth, as well as a significant amount of pebbles, roots, and remains of bricks, cans, and other rubble. During the investigation, construction was taking place at the CEG faculty, and large metal containers were present on the SE side of the survey grid. These containers could interfere with the readings of the GPR.

3.1.2 Method

The common-offset GPR setup was previously used to collect data at the TU Delft site in 2018. Therefore, the recommendations given in the 2018 work were taken into consideration; lines were collected every 0.25 m instead of every 0.5 m, and only the 250-MHz antenna was used, since it was suggested that the 500-MHz antenna would record too many unwanted signals (e.g. tree roots). Data was collected once along each line shown in figure 3.4, and always in the same direction (not in zigzag mode).

Multiple-offset GPR data was also collected along two lines X=2.75 and X=5.20. These lines were chosen based on estimations of the locations of the barrel containing metal rods and the empty barrel, respectively. The procedure for the multiple-offset GPR data collection is as follows (figure 3.5):

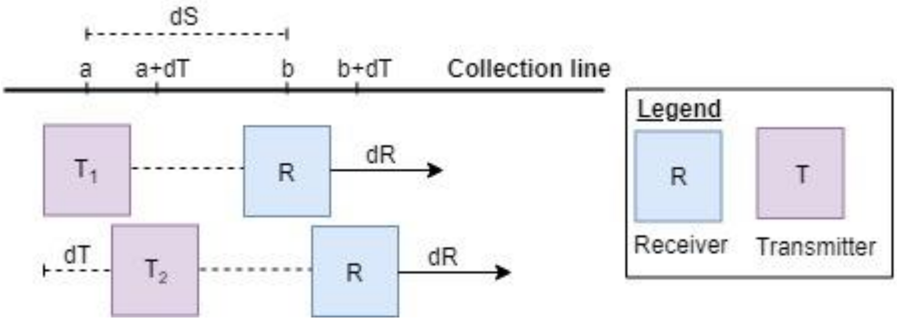

Figure 3.5: Schematic diagram of multiple-offset GPR data collection.

1. The transmitter and receiver are placed at some initial positions *a* and *b*, respectively, along the collection line, with separation *dS*.
2. The receiver is moved away from the transmitter along the collection line, and measurements are triggered by the odometer at each increased step *dR*.
3. The transmitter is shifted to position *a*+*dT* and the receiver to position *b*+*dT* on the collection line, and a new collection is completed. This is repeated a number of times.

Table 3.1 shows the parameters of the data collection for the two lines at the TU Delft site. Figure 3.6 shows the set-up before a measurement. Notice that *dS* is increased by the presence of the odometer, and that the total number of measurements is restricted by the length of the cable connecting the receiver and transmitter.

Table 3.1: Overview of multiple-offset GPR data collected at the TU Delft site.

	X=2.75	**X=5.20**
Initial transmitter position	Y=4.25	Y=3.20
Final transmitter position	Y=1.65	Y=2.00
dT	0.10 m	0.10 m
dS	0.83 m	0.83 m
dR	0.02 m	0.02 m

Figure 3.6: Photograph of multiple-offset GPR set-up before data collection.

Later it was recognised that for EMI and AS to give the best results, at least one receiver position should coincide exactly with the position of each source. Therefore, *dS* was changed to 0.84 cm at the ARISTA facility.

3.2 ARISTA Facility

The ARISTA facility was officially opened in 2017, as Europe's first subsurface human-taphonomy research area. In this investigation, two control graves are studied: one refilled empty pit, and one containing a human cadaver. To simplify this, the former will be referred to as the "pit", and the latter, the "burial". The word "control" signifies that neither grave has been exhumed since initial burial. Both graves were created at the same time.

3.2.1 Site Description

Figure 3.7 shows the location of the ARISTA facility near the UMC AMC, where the burial and pit are indicated by the initials B and P, respectively. The geometry of the graves in relation to the path and fence are shown in figure 3.8. Figure 3.8 also shows the location of a third grave containing a human cadaver (B.2) close to the pit, which may have interfered with the data collection.

The soil at the location is sand, and was very loose over the graves. Both graves were originally dug to a depth of 0.6m, meaning the top of the cadaver in the burial is approximately 0.3 m below the surface, though subsequent compaction of the soil may have decreased this value. Though the height of the surface over the pit was relatively consistent, a noticeable bump could be seen over the location of the burial, raised about 5 cm from the rest of the ground directly over the burial spot. Detailed baseline information on the site, such as soil stratigraphy, groundwater conditions, and elevation information is available, but was not provided during this investigation.

Each grave contains sensors for moisture and temperature, as well as cables connecting these sensors to multiplexers which are visible in the satellite picture in figure 3.7, marked by blue rings. The exact location of these sensors and cables are not known, though the trench for the cables is between each grave and the path. In addition, both graves are within 1 m of the fence, which is supported by metal poles, and a small metal plate is located in close proximity to the burial (visible in figure 3.9). These metal components could have interfered with the GPR data collection.

GPR data was collected over the pit on the first day, and over the burial on the second day of fieldwork. On the second day of fieldwork, it rained, which means that the soil conditions were different over the course of the investigation.

Figure 3.7: Location of investigation site at the ARISTA facility in Amsterdam. Multiplexers marked by blue rings. Base maps sourced from: (Google Maps, 2019; pdok, 2019).

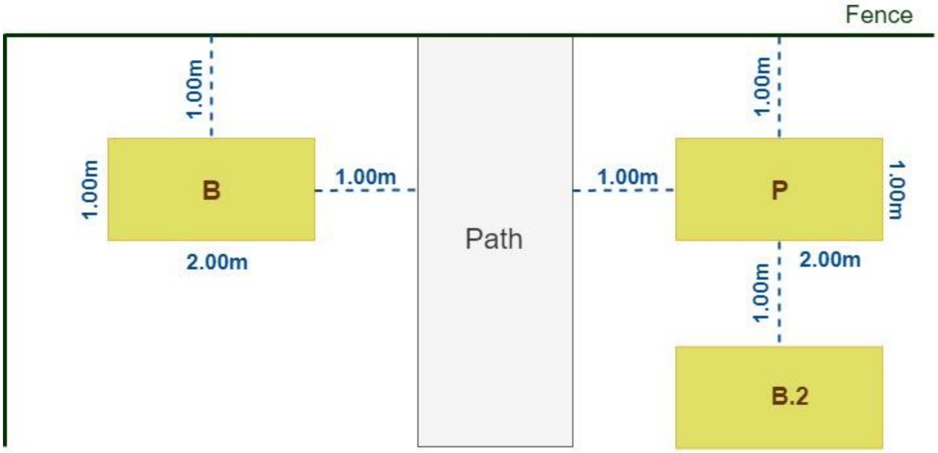

Figure 3.8: Locations of the two studied graves and one nearby grave at the ARISTA facility. B and B.2 signify burials, P signifies a refilled empty pit.

Figure 3.9: Photograph of resistivity survey setup at the ARISTA facility, with possible interferences marked by blue arrows and rings.

3.2.2 Method

The 250-MHz frequency was chosen for the ARISTA facility investigation based on the recommendations from the previous theses that this frequency would be better than the 500-MHz frequency for larger and deeper targets (Harms, 2018; Vroom, 2018). Common-offset lines were collected according the grids shown in figure 3.10, which also shows the main sources of interference. Since the path acts as an axis of symmetry between the burial and the pit, the X-coordinates of the grids over the graves do not correspond directly. The line X=0.00 over the pit corresponds to the line X=3.00 over the burial. A reference table of corresponding lines is presented in Appendix A. Once again, all lines were collected in the same walking direction, and not in zigzag mode.

Some lines over the burial in the X direction (Y=0.00 to Y=3.00), were shorter due to the presence of several plants near the fence (visible in figure 3.9). The same lines sometimes had a few skips near the very end of the line due to these plants, meaning the receiver was moved too quickly to gather sufficient data for a trace.

Multiple-offset lines were collected along one line in the Y direction and one line in the X direction over each grave according to the same procedure outlined for the TU Delft site, and these lines are summarised in table 3.2. At this site, the length of the cable connecting the receiver and transmitter was not the only factor limiting the number of receiver positions for each gather – the presence of the fence was also a hinderance. Figure 3.11 is a photograph taken during the collection of a multiple-offset line.

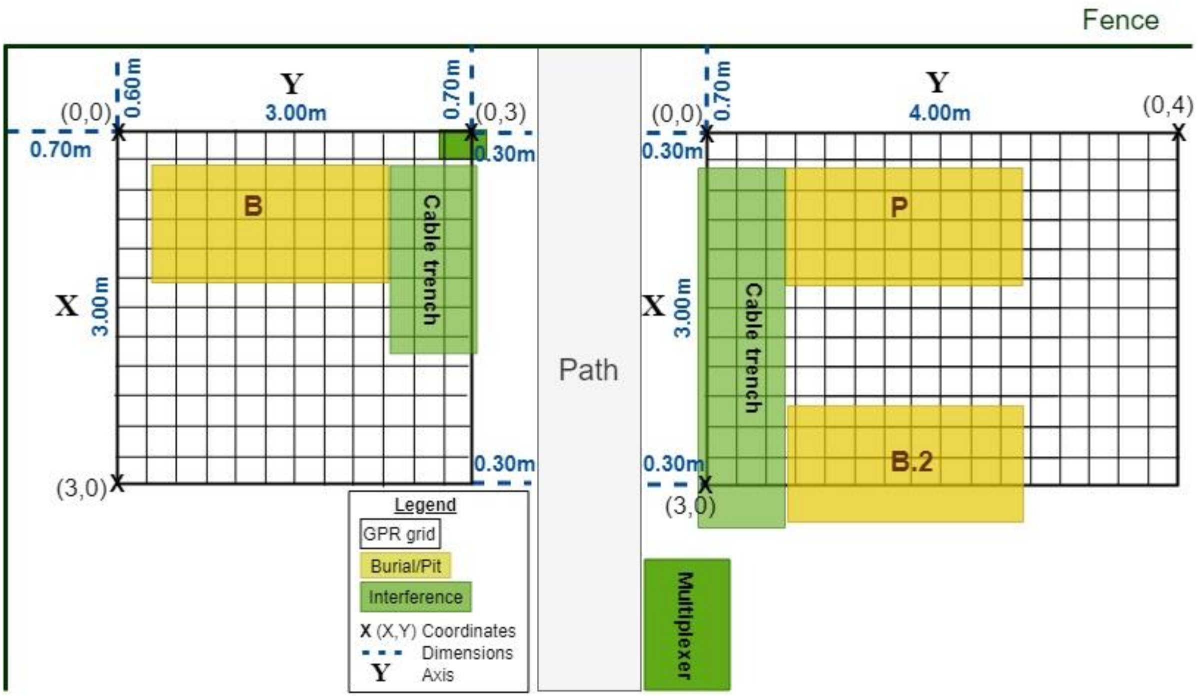

Figure 3.10: GPR data collection grid at the ARISTA site.

Table 3.2: Overview of multiple-offset GPR data collection at the ARISTA facility.

	X=1.00	**Y=1.50**	**X=1.15**	**X=1.15**	**Y=3.00**
Grave	Burial	Burial	Pit	Pit	Pit
Initial transmitter position	Y=5.30	X=5.95	Y=-0.30	Y=2.80	X=-0.40
Final transmitter position	Y=3.40	X=4.05	Y=1.10	Y=4.20	X=2.30
dT	0.10 m	0.10 m	0.10 m	0.10 m	0.10 m
dS	0.84 m	0.84 m	0.84 m	0.84 m	0.84 m
dR	0.02 m	0.02 m	0.02 m	0.02 m	0.02 m

Figure 3.11: Photograph taken during the collection of a line of multiple-offset GPR data.

4. Data Processing and Results

This chapter presents the data processing that was done for each of the methods used in the investigation of the two sites: the common-offset GPR and the multiple-offset GPR. The results are also presented here.

4.1 Common-Offset GPR

This subchapter provides the processing steps and the most important results for the common-offset setup. Images of all results will be provided in Appendix A. Consistent axes are used for all images of results, with the right Y-axis showing time in nanoseconds, the left Y-axis showing depth in meters using the velocities defined in section 4.1.1, and the X-axis always being consistent with the coordinates of the grids defined for each site.

4.1.1 Processing

The data processing performed for the common-offset data collection was similar to the processing performed in the theses of 2018, with the goal of limiting noise and enhancing reflections. The data was processed using EKKO View Deluxe and visualised as radargrams in EKKO View 2. Timeslices were created in EKKO Mapper. These programs are the default for processing data from the pulseEKKO pro and are created by the manufacturer of the equipment. The steps performed were as follows:

1. Reverse and reposition data lines to correspond to the coordinates of the grids shown in figures 3.4 and 3.10
2. Dewow
3. Repick timezero to 1% of largest amplitude
4. Background subtraction of average of all traces
5. Bandpass filter using 0, 50, 500, 600 MHz to eliminate very high and very low frequencies
6. AGC with 50 maximum gain and a window width of 1.5

The effects of each of these processing steps are shown in Appendix B, where the amplitude spectra of some of the raw data are also provided. For the radargrams at the ARISTA facility, the groundwave velocity was calculated using the multiple-offset data, and was found to have an average value of 0.112 m/ns, which is within the range of values for sandy soils (Goodman & Piro, 2013). The groundwave was less clearly visible in the multiple-offset data collected at the TU Delft site, due to stronger attenuation, so a velocity of 0.075 m/ns was used, which is the same as for the 2018 theses.

These velocities in combination with a frequency of 250 MHz suggest a resolution of 0.112 m for the ARISTA site, and 0.075 m for the TU Delft site, assuming the resolution to be ¼ of a wavelength. The use of 250 MHz to calculate the resolution is justified for both sites, since although the peak frequency of the received amplitude spectra (shown in Appendix B) have shifted slightly from the theoretical transmitted signal, the central frequency and, more importantly, the bandwidth have remained at about 250 MHz (E. Slob, personal communication, June 2019; Jol, 2009).

4.1.2 TU Delft Results

The common-offset data collected at the TU Delft site is especially important, as it provides a way to redefine the locations of the buried targets, such that the resistivity data analysed in the thesis by Claire Mulder can be appropriately interpreted, and such that future investigations can use these new coordinates for reference.

The clearest target in the radargrams is the barrel containing metal rods, which is visible along lines Y=1.50, and Y=1.75, centred at about X=3.00, as seen in figures 4.1 and 4.2. The same signal is visible in lines X=3.00 and X=3.25 (most clearly in the latter), centred at about Y=1.50 (figures 4.3 and 4.4), which supports the attribution of this signal to the barrel with metal rods, as a tree root can usually be followed in several adjacent radargrams. In addition, this reflection looks very similar to the reflection defined in the 2018 theses as the barrel containing steel rods, both in patterning and depth interval. Along X=3.00 and X=3.25, the barrel is close to a strong adjacent signal. This signal is very consistently seen in lines parallel to the X-axis, and seems too straight to be a tree root, which one would assume to be more winding, so perhaps this could be a pipe or buried cable.

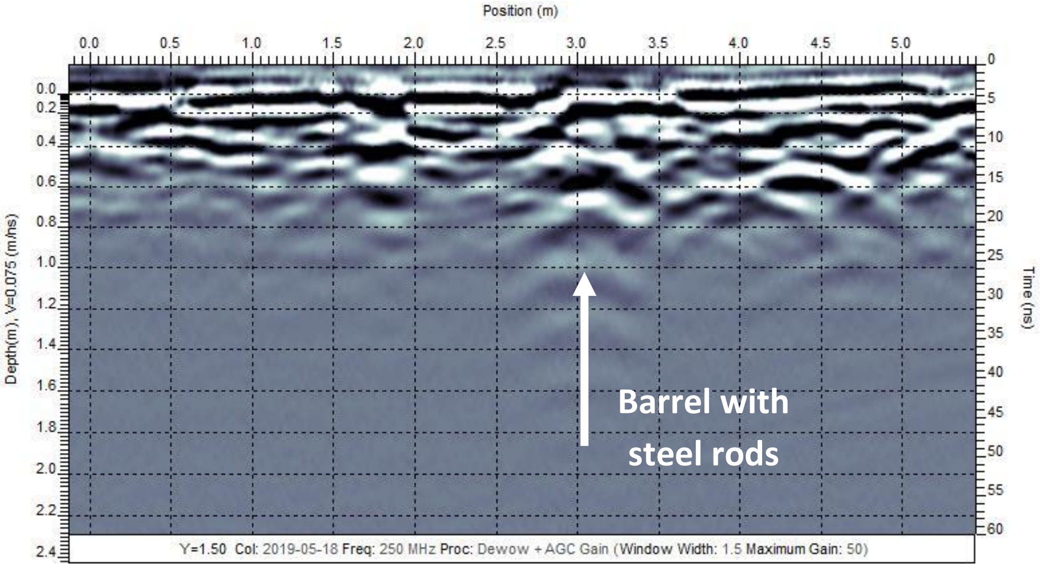

Figure 4.1: TU Delft site line Y=1.50, 2019.

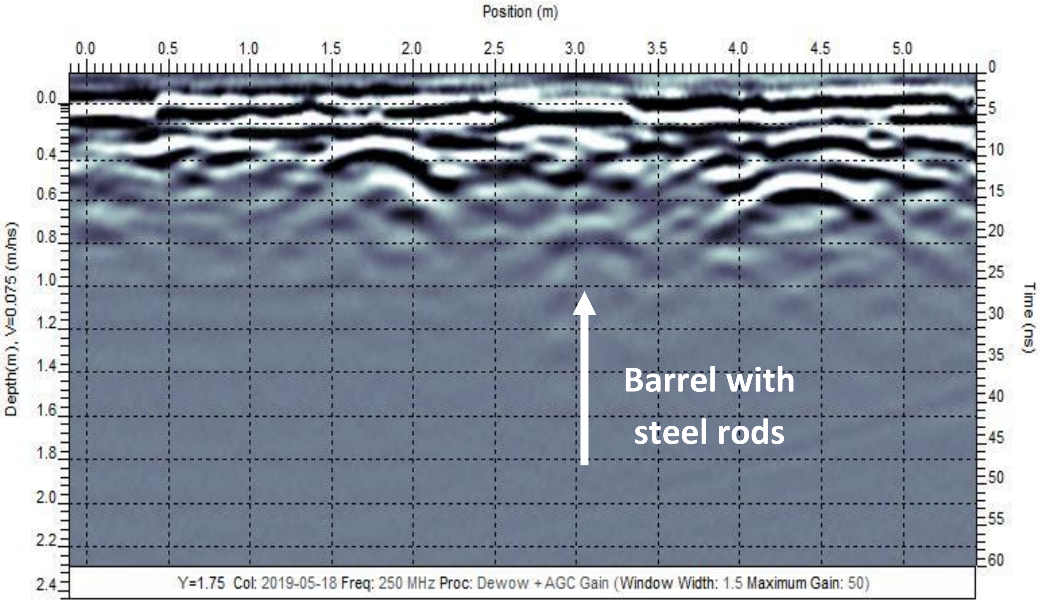

Figure 4.2: TU Delft site line Y=1.75, 2019.

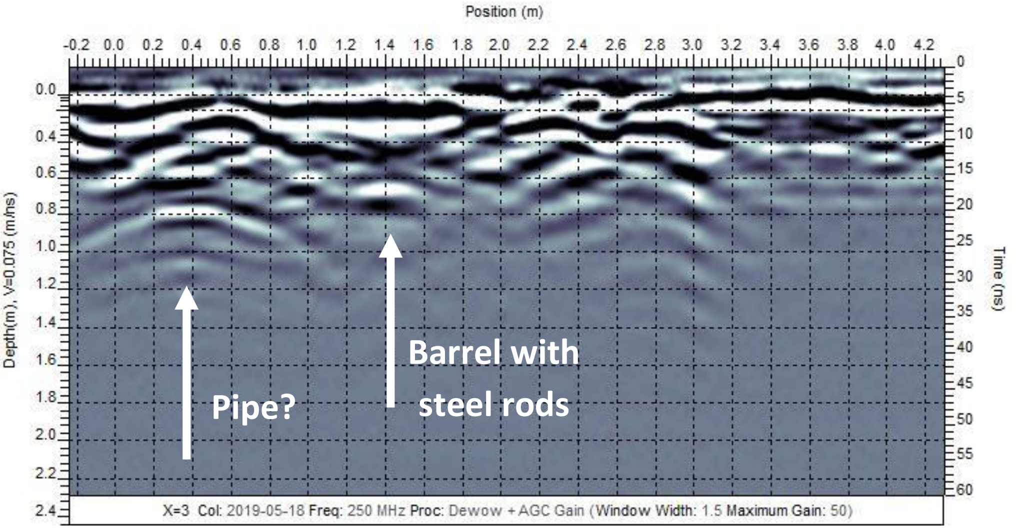

Figure 4.3: TU Delft site line X=3.00, 2019.

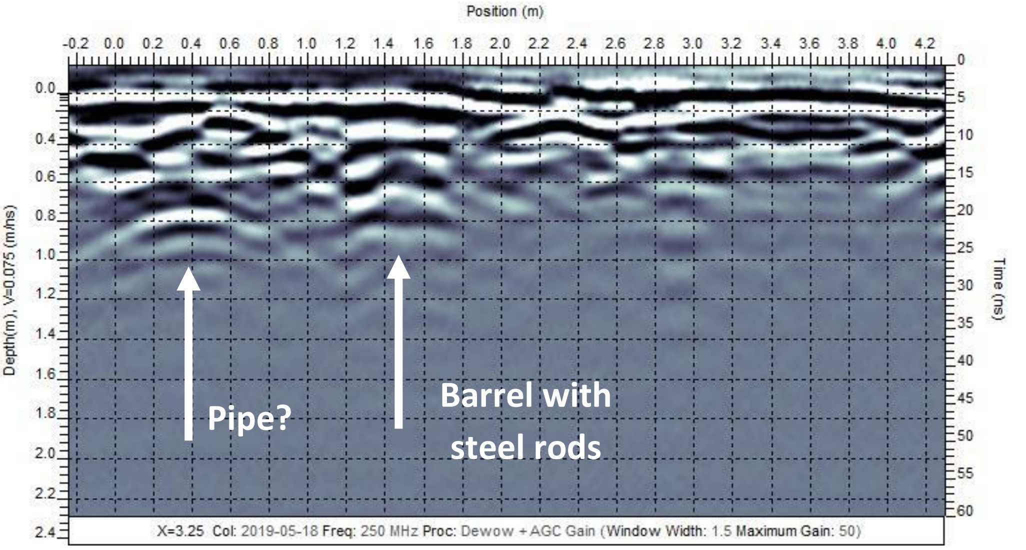

Figure 4.4: TU Delft site line X=3.25, 2019.

The other targets are not clearly visible without knowing their locations, since the site is filled with large tree roots, despite the results of the 2018 theses suggesting that the 250-MHz antenna might show less unwanted reflections.

Using the position of the barrel with steel rods and the grid from the 2018 theses, and assuming the new grid is not rotated with regards to the old grid, the positions of the targets may be redefined. This is summarised in table 4.1.

Table 4.1: Redefined coordinates.

	Coordinates in grid of 2018 theses (figure 3.2)	Redefined coordinates in new grid (figure 3.4)
Barrel with steel rods	(1.7, 2.2)	(3.25, 1.50)
Empty barrel	(0.7, 0.7)	(4.75, 0.50)
Refilled pit	(4.2, 4.2)	(1.25, 4.00)

These new positions allow us to compare the results from this year to those of last year. The empty barrel should be visible in line X=4.25 (figure 4.5), centred at Y=0.50, but in this line and the adjacent lines there is only the possible pipe previously identified. In the other direction, on line Y=0.50 (figure 4.6), the region around X=4.50 does show a very weak hyperbola, but it is difficult to tell whether this is due to the empty barrel or tree roots.

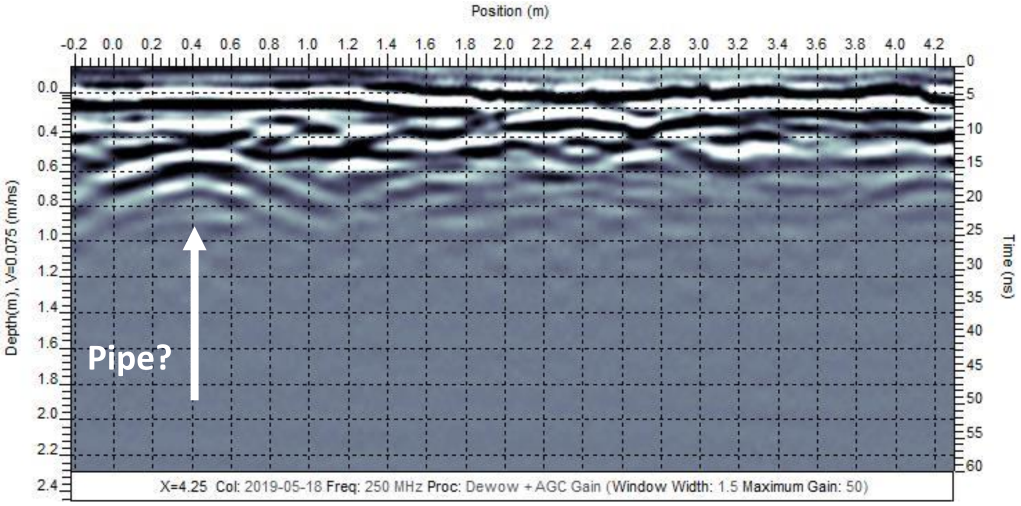

Figure 4.5: TU Delft site line X=4.25, 2019.

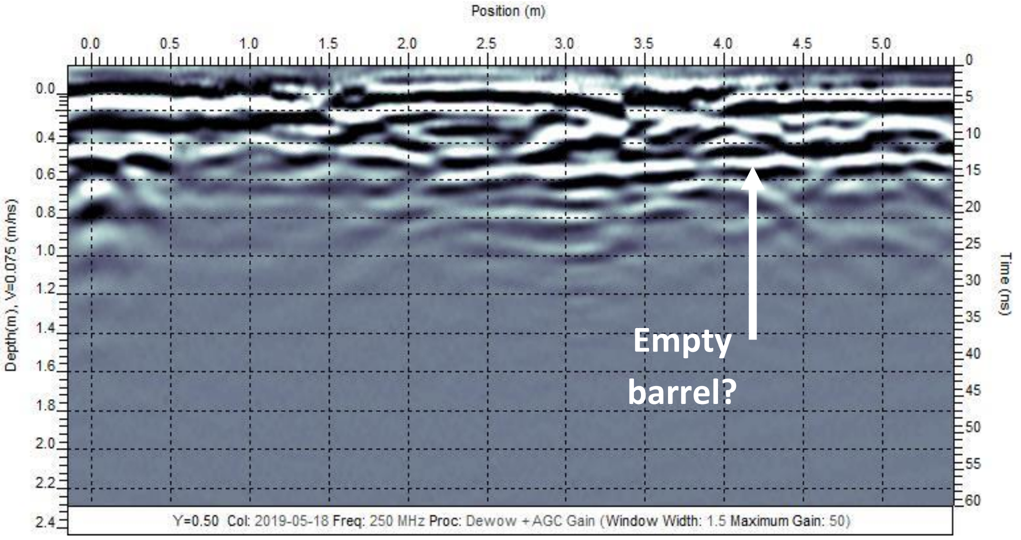

Figure 4.6: TU Delft site line Y=0.50, 2019.

In the case of the refilled pit, line X=1.25 (figure 4.7) does show the beginning of a hyperbola near Y=4.20, but due to the strength of the signal, this is more likely a tree root, as even in the 2018 theses, the refilled pit was nearly unidentifiable in the results. The corresponding radargram for Y=4.00 (figure 4.8) supports this, as the hyperbola seen at X=1.25 in this line can be followed in adjacent lines, moving toward X=1.50.

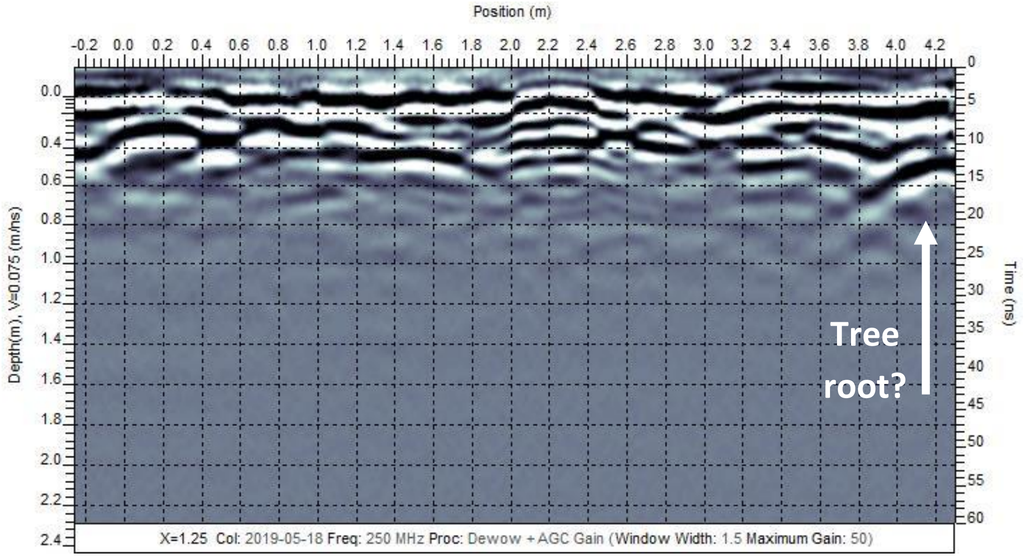

Figure 4.7: TU Delft site line X=1.25, 2019.

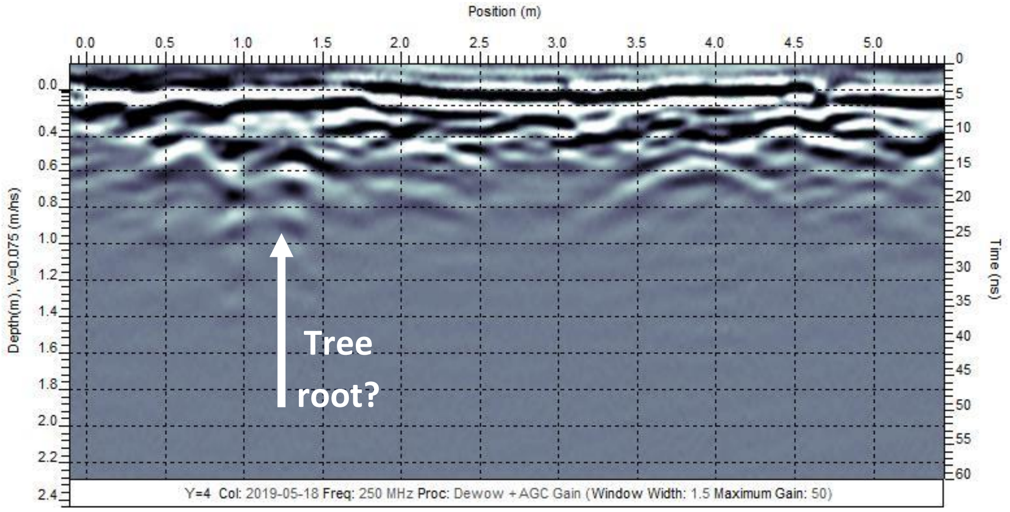

Figure 4.8: TU Delft site line Y=4.00, 2019.

4.1.3 ARISTA Facility Results

For the results of the common-offset GPR data collection at the ARISTA facility, lines which are comparable between the burial and the pit were grouped together in images with markings showing the expected location of each grave. Where the grave B.2 was covered in a line, this is also marked. Figure 4.9 provides a common legend for these images. Note that a lighter green colour indicating the trenches for the cables is chosen since it is not known exactly where these trenches are located.

Since the targets are buried shallowly, direct waves cover most of the useful signals in the raw data. These direct waves have been somewhat removed through the background subtraction applied in the processing, the effects of which may be seen in figures B.3 and B.4 in Appendix B.

The higher velocity at the ARISTA site meant a lower resolution. In addition, there was less attenuation of the waves, and the signal penetrated much deeper than the estimated depth of the graves. In general, the common-offset data from the ARISTA facility was characterised by strong interference from the nearby fence, metal plate, and other factors as described in section 3.2.1. The effect of especially the metal plate can be seen clearly in line X=0.25 over the burial (figure 4.10), where it creates a strong, echoing signal which affects the whole line of data.

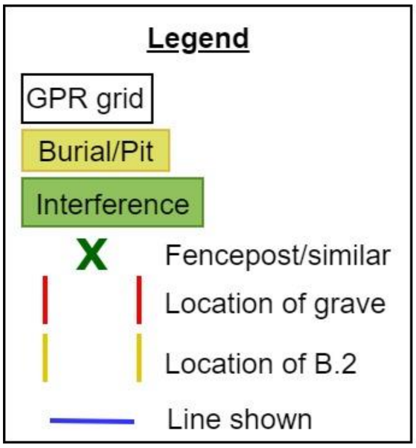

Figure 4.9: Legend for figures 4.10 to 4.14.

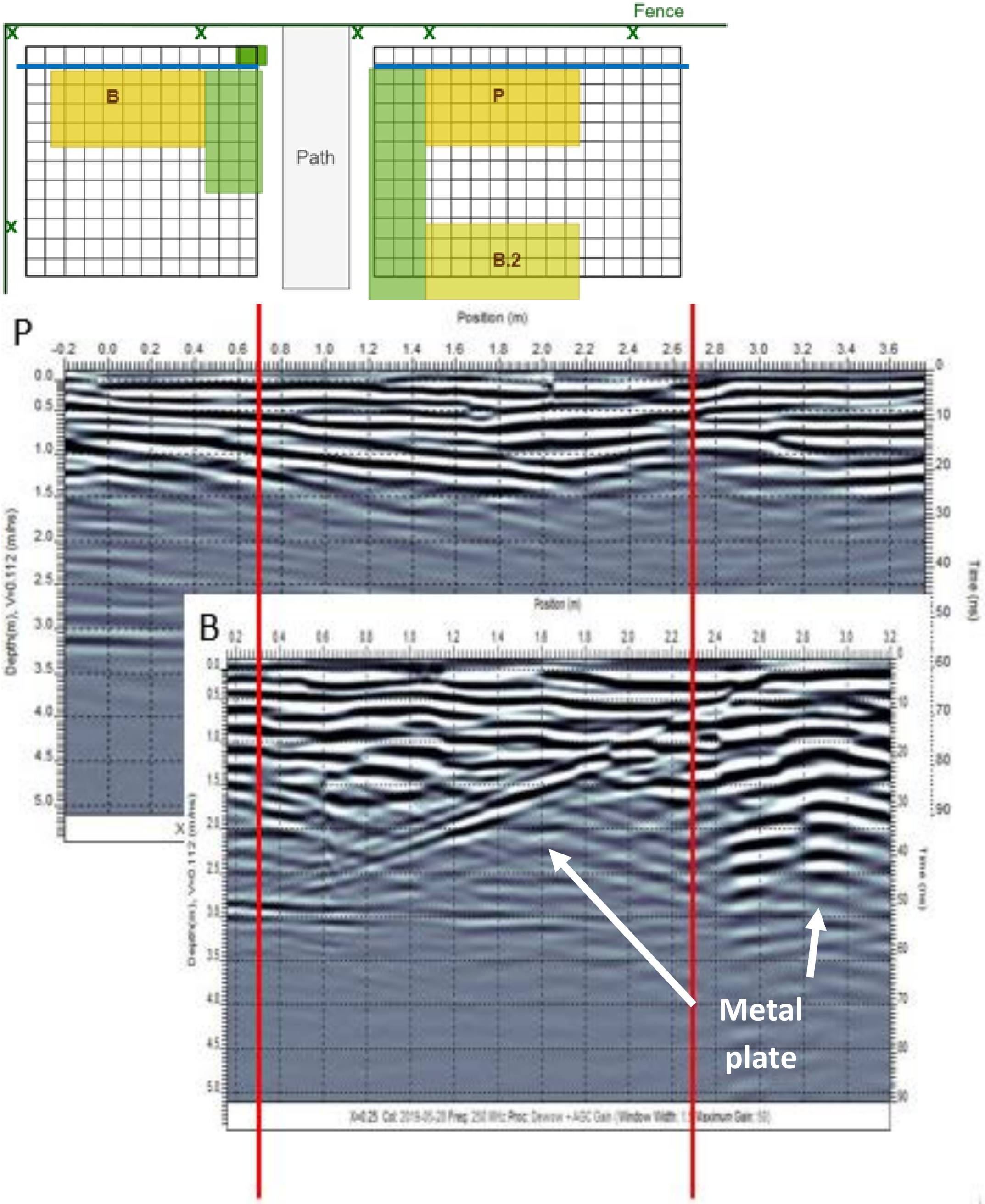

Figure 4.10: Line X=0.25 for both graves, 2019.

Lines over the pit are not exempt from this kind of interference, however. Figure 4.11 shows a signal in both the burial and the pit, which is likely due to the trench for the cables, since it shows up similarly in both lines, and begins outside the area occupied by the graves. The same figure, does suggest some small differences between the pit and the burial, as the pit seems to have slightly more homogeneous layers at the very top. A similar pattern may be observed in adjacent lines.

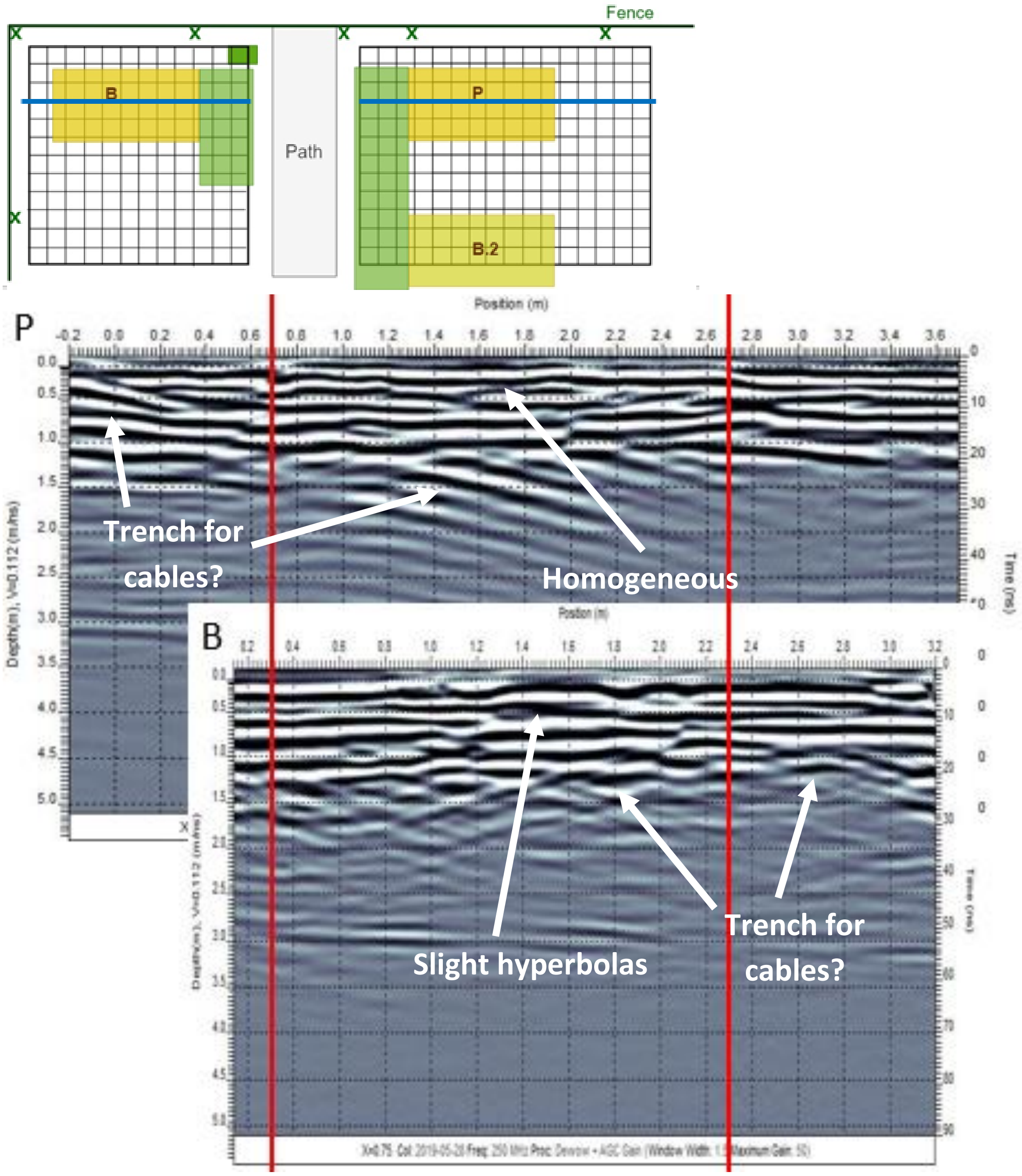

Figure 4.11: Line X=0.75 for both graves, 2019.

In the other direction, the effects of the nearby metal objects are again clear. Figure 4.12 shows the metal plate once again visible in the line over the burial, and another signal visible over the pit, which is likely due to the multiplexer, as well as a weak signal on the other side of the pit, likely due to the metal fence post. These interferences continue in several adjacent lines. Looking past this interference, however, it does seem that the response in the region of both graves is more homogeneous here, outside the location of the actual trenches.

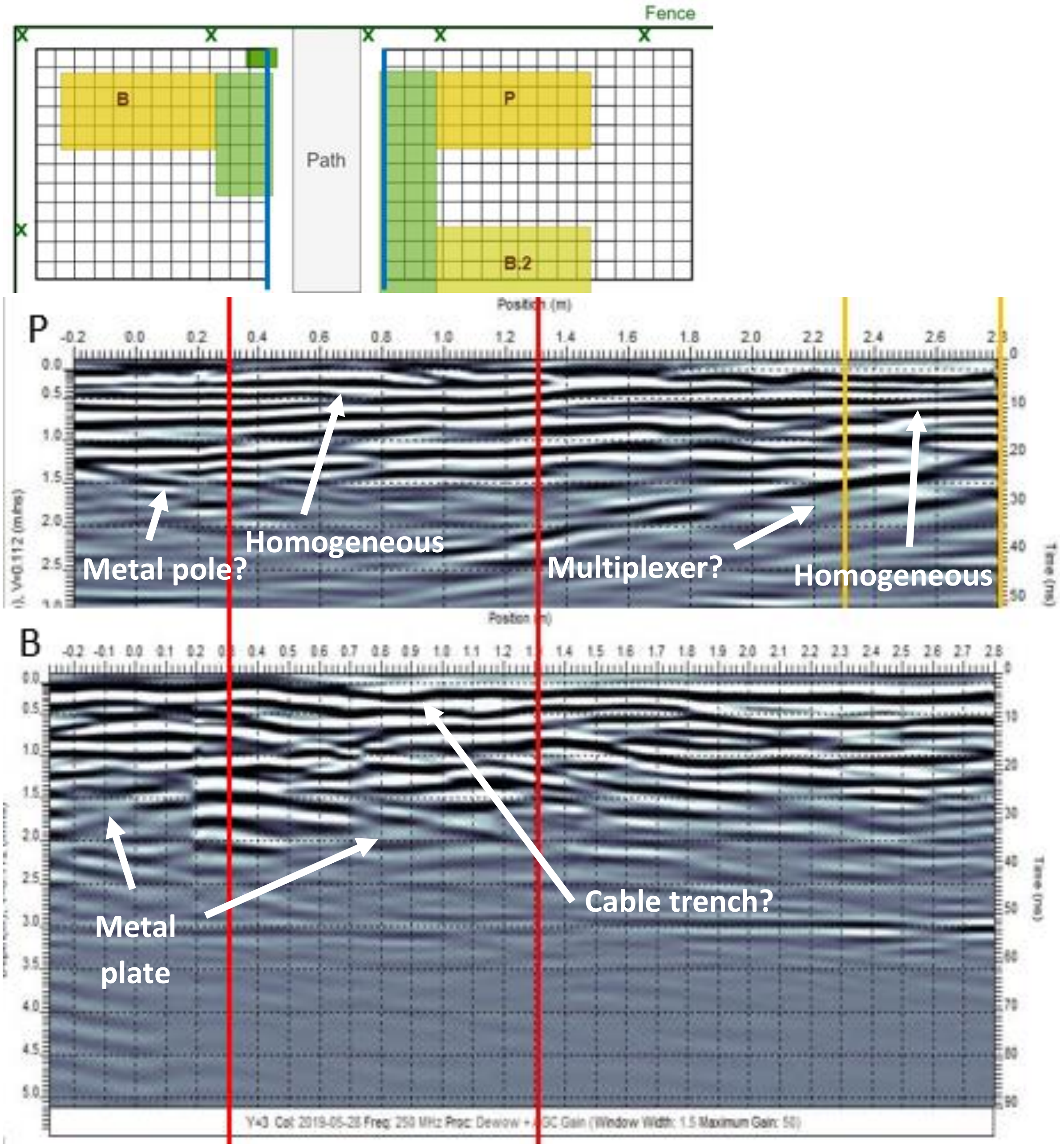

Figure 4.12: Line Y=3.00 (B) and Y=0.00 (P) , 2019.

The fence itself also seems to create some interference, even when no fence posts are near. This is seen in figure 4.13, where a signal is seen near the fence over the burial, far from the metal plate or any fence posts. However, the same signal is not visible over the pit, despite similar distances to the fence, suggesting that interference from the fence itself is not consistent, or that the aforementioned signal is not due to the fence, but to some unseen object under the surface. It is possible that the plastic sheet which covers the fence is buried in some areas. It is unlikely that this is a difference between the burial and the pit, since the signal begins outside the grave. In the same figure, slight hyperbolas are visible over the burial, whereas the pit shows more homogeneous signals. Part of a hyperbola may also be seen over grave B.2 in the line over the pit.

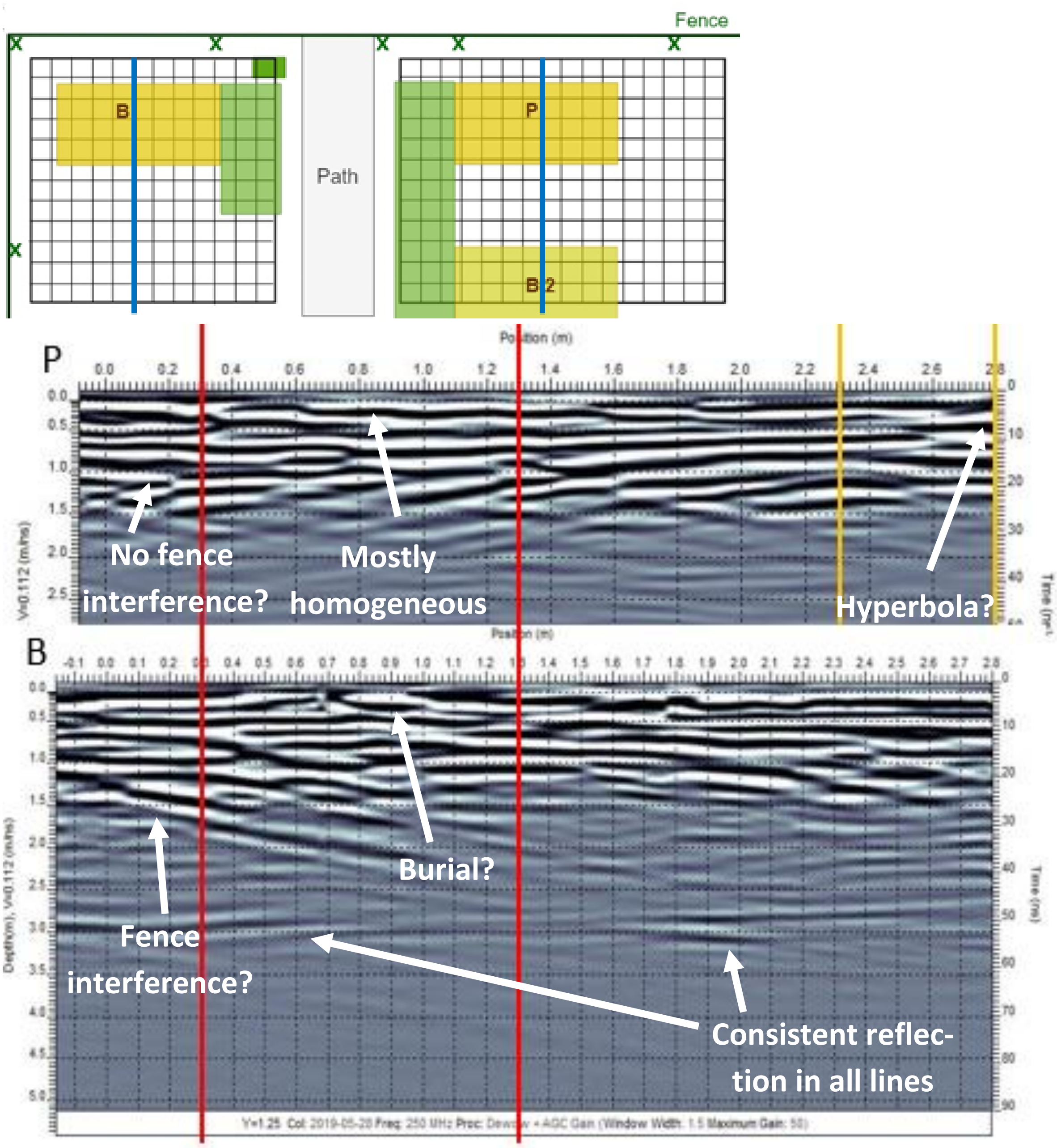

Figure 4.13: Line Y=1.25 (B) and Y=1.75 (P) , 2019.

One interesting note to make is that there is a visible hyperbola in the pit grid compared to the burial grid in line X=2.75, where the situation is reversed. Here, the line traverses grave B.2 (figure 4.14). The clarity of the hyperbola over B.2 may be attributed to the fact that this grave has been exhumed for research after burial, and is therefore a “fresher” trench. Interference is still seen in both graves for this line. In the pit (now grave B.2), this may once again be due to the cable trench in the pit grid, while in the burial grid (now empty, i.e., no grave nor pit), this is most likely due to the nearby fence post.

Another observation is that a homogeneous reflection is consistently seen in all the collected lines at a depth of approximately 3 m (pointed out in figures 4.13 and 4.14). This could be due to a change in soil type at that depth, which can be confirmed if given access to geological data from the ARISTA facility.

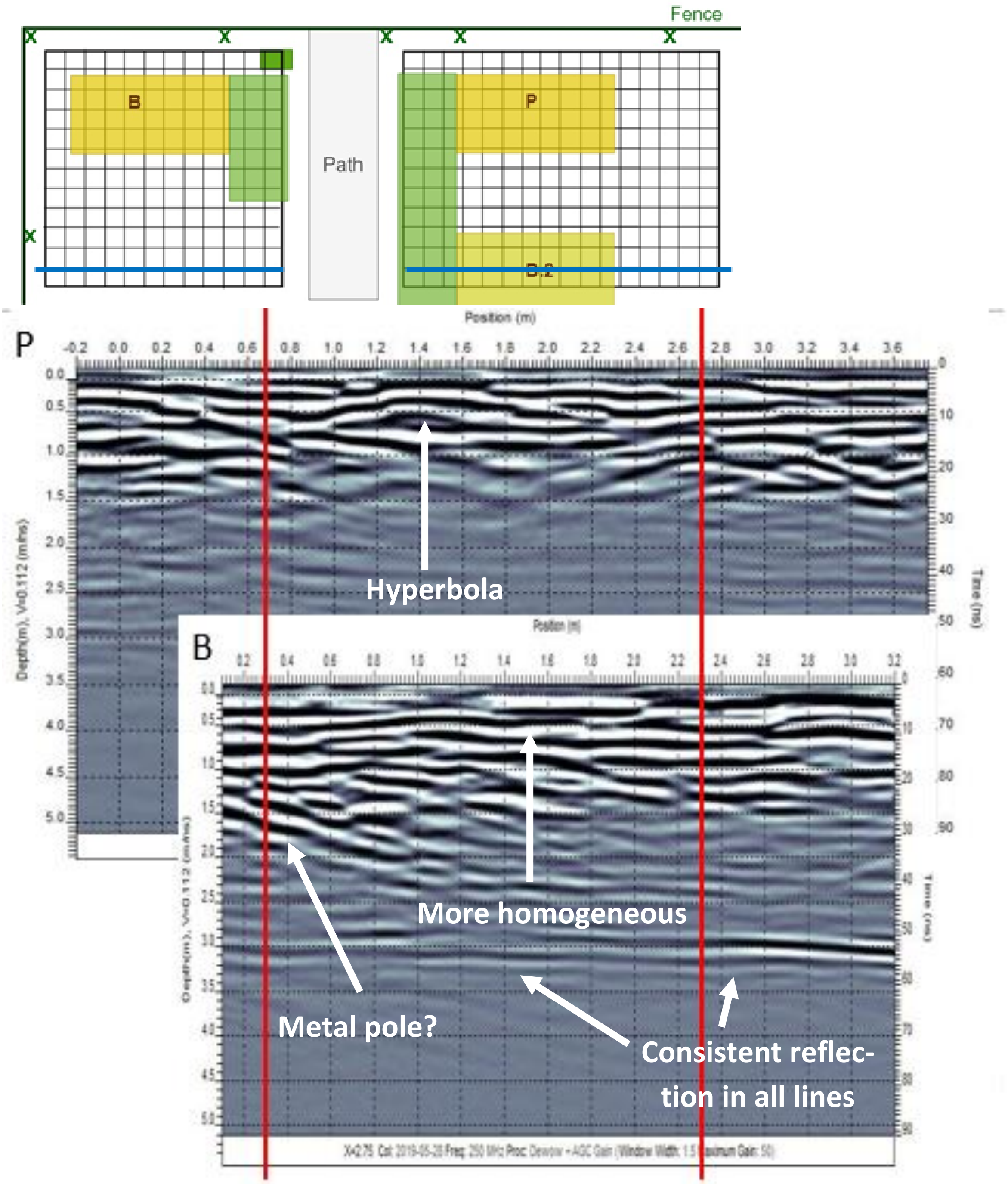

Figure 4.14: Line X=2.75 for both graves, 2019.

4.2 Multiple-Offset GPR

This subchapter presents the processing steps for the multiple-offset GPR data gathered. The principles of EMI and AS have already been discussed in chapter two, and will not be recounted here. The multiple-offset GPR data required considerably more data processing than the common-offset data. A main goal of this thesis is the investigation of the best method for supressing the direct waves in the original data. Therefore, only one collection line will be discussed due to time restrictions, though the other lines will be available on the TU Delft data repository for anyone interested in continuing the project.

The line chosen for this analysis is line Y=1.50 over the burial at the ARISTA facility, as this line has the highest chance of capturing some reflection in the subsurface. The pit at the ARISTA facility would hypothetically have a weaker response than the burial. The lines at the TU Delft site were based on guesses of the locations of the buried targets, and have the additional problem that no receiver position coincides with any source position due to the 0.83 m offset. Though part of the processing is performed in MATLAB, all the images are visualised in Seismic Unix for easy comparison. Full-size versions of the images are given in Appendix C.

4.2.1 Process Optimisation

Each step in the processing of the multiple-offset data requires optimisation for the best method to be determined. The initial step was always to dewow the raw data. Figure 4.15 shows a data line after dewowing.

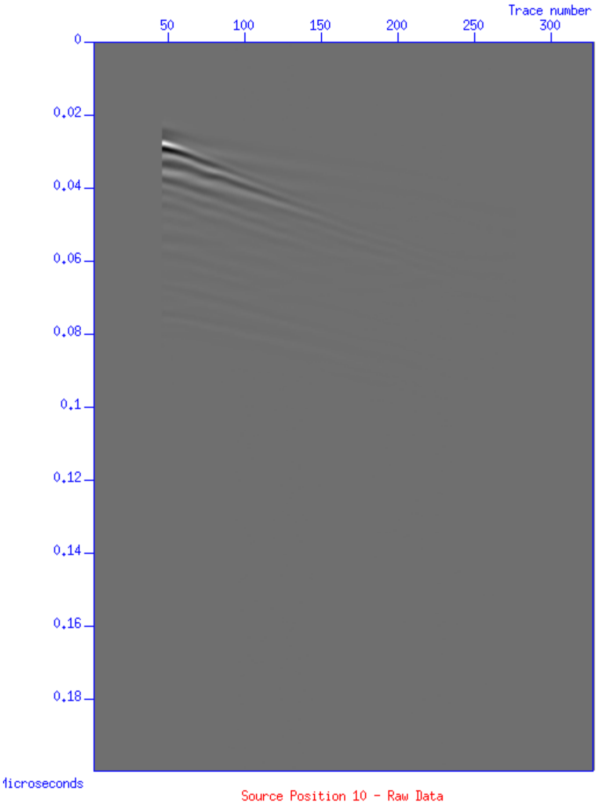

Figure 4.15: Dewowed MO data at source position 10.

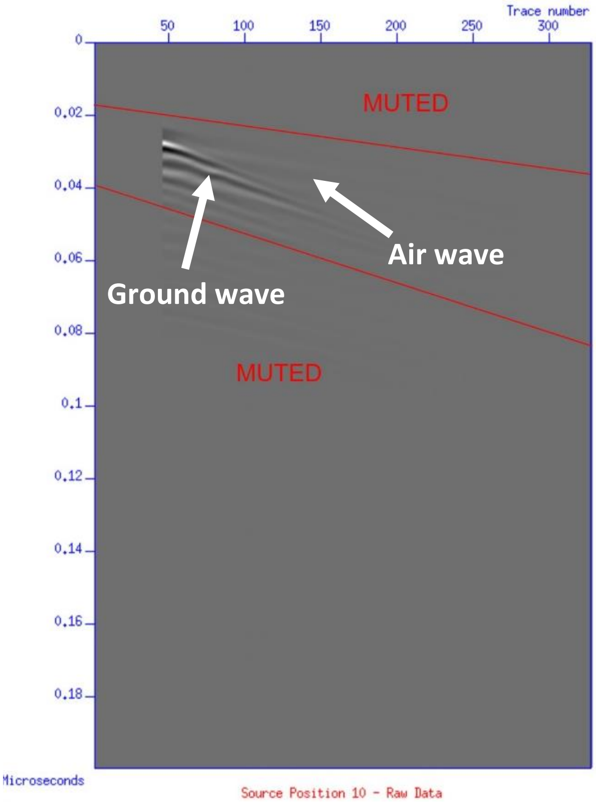

Figure 4.16: Illustration of muting method.

Before cross-correlating the traces, several steps may be taken to “clean” the data in order to better retrieve the direct waves. In this investigation, the following methods were compared:

1. Muting the area containing reflections
2. Applying a bandpass filter to remove very high and very low frequencies
3. Performing both the aforementioned steps
4. No isolation of the direct waves prior to EMI

The bandpass filter applied in methods two and three had a lowcut frequency of 130 MHz and a highcut frequency of 500 MHz, with a sin-shaped taper of length 100 MHz on either side. The mute was applied by estimating the slope of the air wave and ground wave, and muting data on either side of these lines (illustrated in figure 4.16). The direct-wave estimations by EMI of each of these methods are shown in figures 4.17 to 4.20. During the EMI, a time shift has occurred, seen when comparing any of figures 4.17 through 4.20 to the initial data in figure 4.15. This time shift is corrected before AS is performed, such that the direct waves are in the same location in the retrieved direct wave matrix as in the raw data.

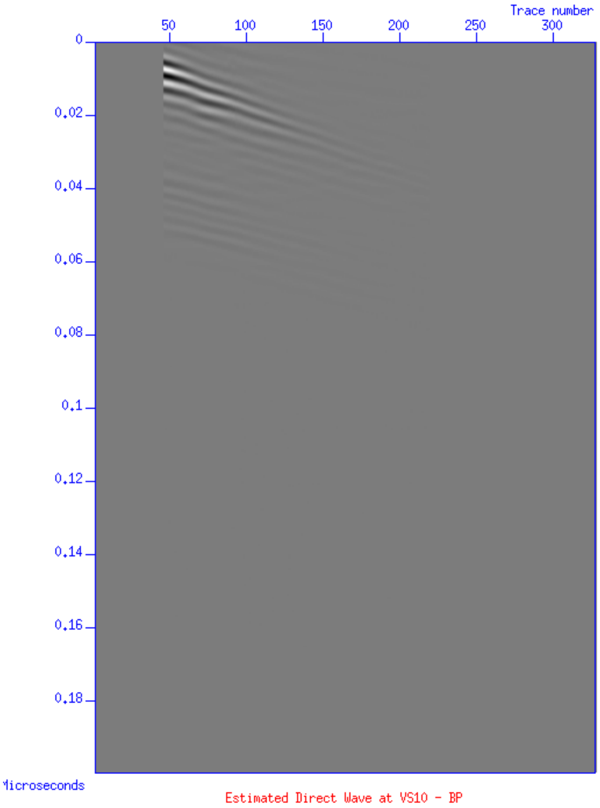

Figure 4.17: Estimated direct wave at virtual source 10 using bandpass filter isolation.

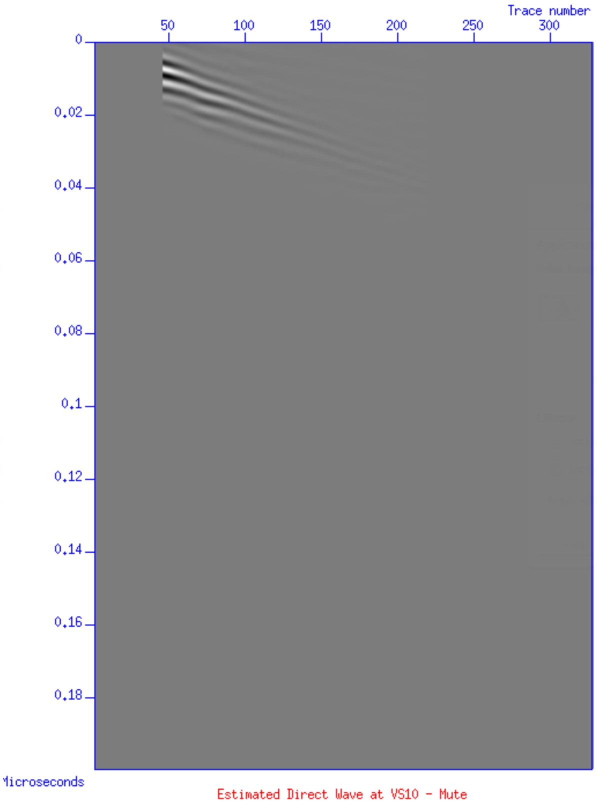

Figure 4.18: Estimated direct wave at virtual source 10 using mute isolation.

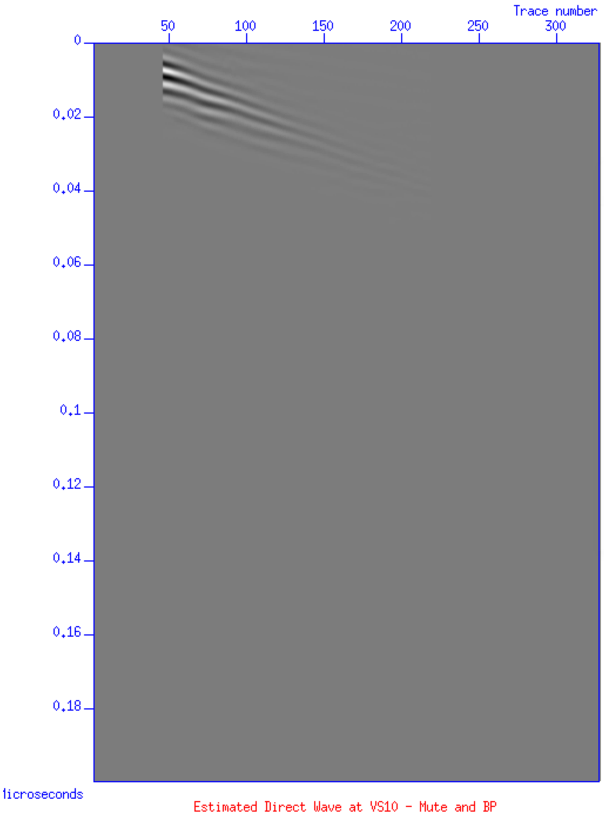

Figure 4.19: Estimated direct wave at virtual source 10 using bandpass filter and mute isolation.

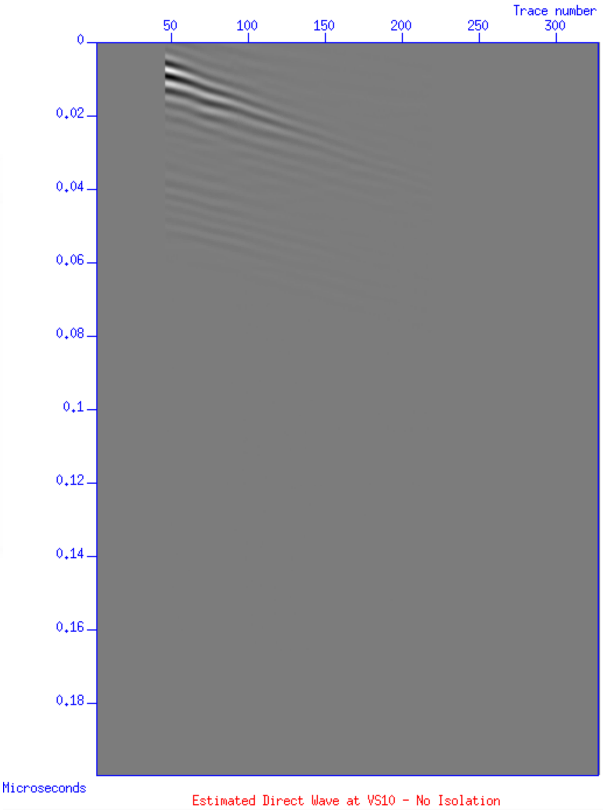

Figure 4.20: Estimated direct wave at virtual source 10 using no isolation.

The function leastsub2 was used in Seismic Unix to subtract the retrieved direct waves from the initial data. This function has its own set of parameters which can be changed, the most important of which are the length of the filter, lfilt, the taper on either side of said filter, ltap, and the size of the window in which the data is fitted, ntwnd x nxwnd (number of time samples by number of traces). The filter length was initially estimated to have an ideal value of 60 time samples using the method described in Dong et al. (2006). Based on this, the filter taper was given a value of 15 time samples, and the window was given a size of 120x7. This initial subtraction is shown for the unisolated direct wave in figure 4.21. The parameters were thereafter shifted slightly, one at a time, and a subjective judgement was made on which set of parameters was better. All the parameters tested are shown in images in Appendix C, and the final set of parameters was chosen to be: lfilt=100, ltap=20, ntwnd=200, nxwnd=10 (figure 4.22). Both figures 4.21 and 4.22 are marked with a blue circle highlighting one difference between them, where the reflections are clearer in the latter. These reflections seem to be nearly horizontal in nature, suggesting they may originate from a far-away object in the cross-line direction, though this would require additional investigation in order to confirm. Figure 4.22 also points out the region of subtracted direct ground wave, as well as one clear reflection, which here has a higher amplitude relative to the ground wave than in the original raw data (figure 4.15).

One aspect of EMI is that the direct wave will only be retrieved if the common source gathers at the virtual source position and the receiver position have at least one source in common. This is not true for the very end of each line, mainly due to the large 0.84 m initial offset. Because of this, the retrieved direct wave is shorter than in the initial data, causing the “clearer” region after trace number 220 in figures 4.21 and 4.22. In fact, this area is not clearer – the direct waves simply have not been subtracted.

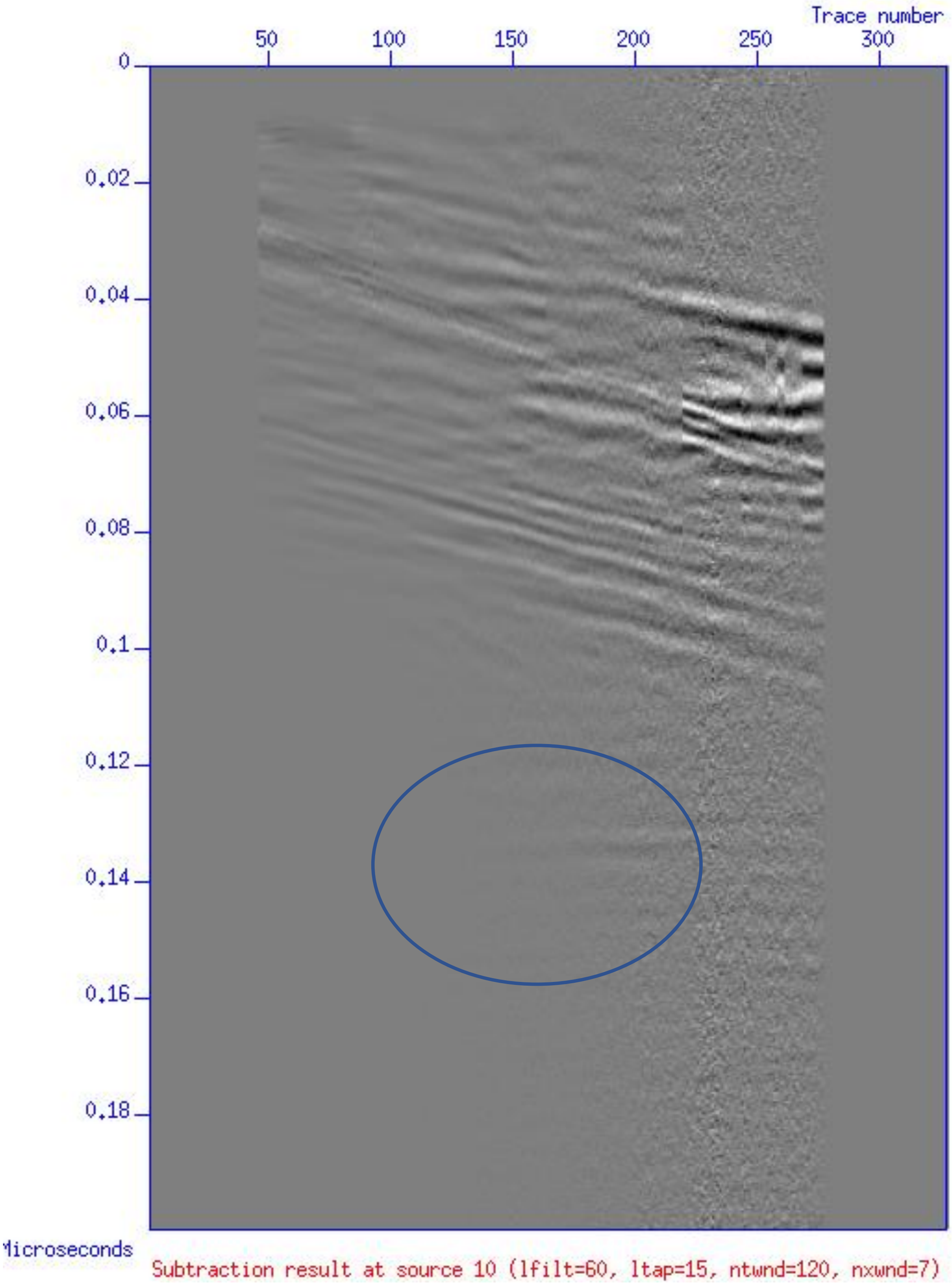

Figure 4.21: Subtracted unisolated direct wave at source 10 using parameters lfilt=60, ltap=15, ntwnd=120, nxwnd=7. Blue ring highlights dim reflections.

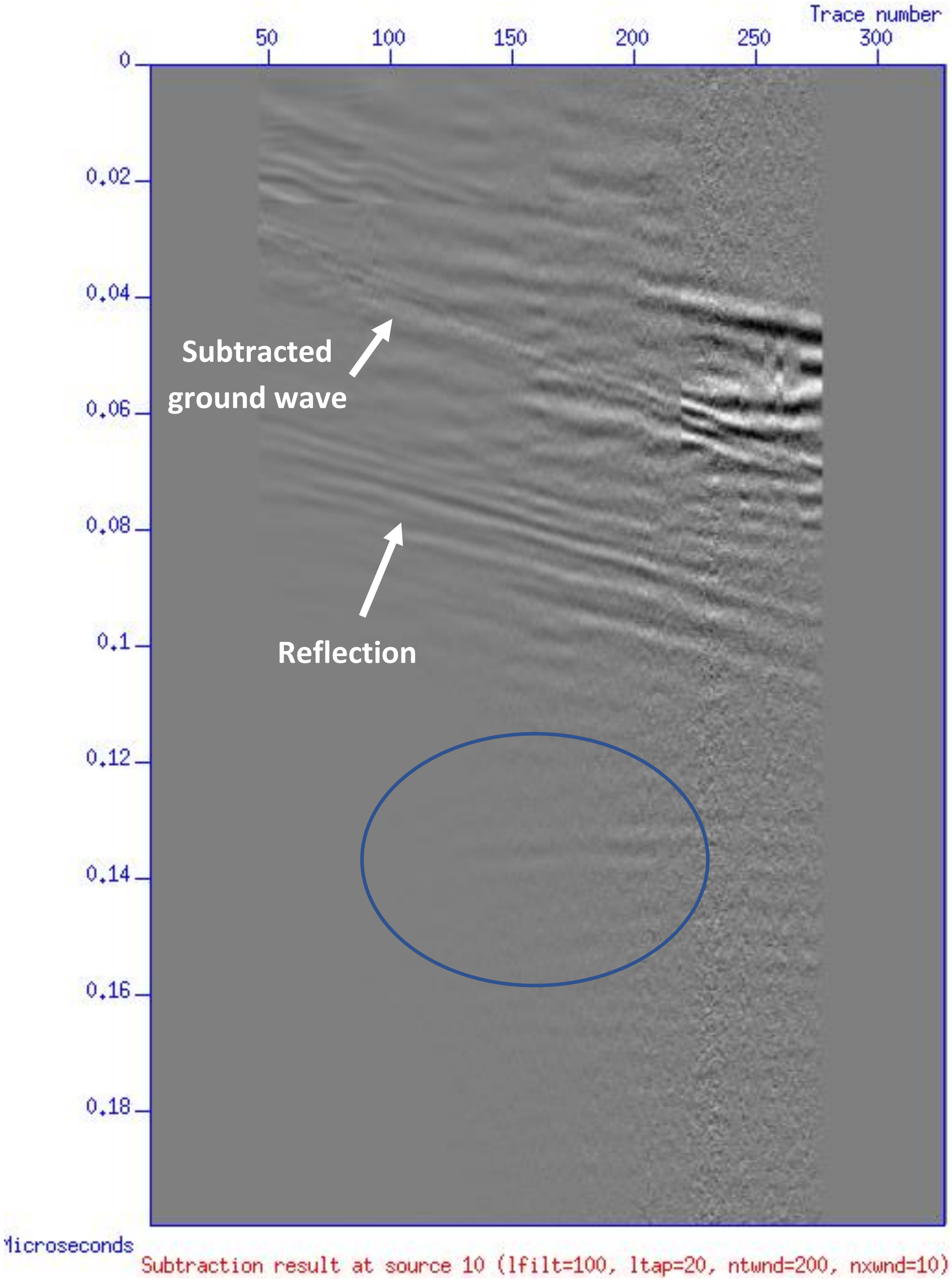

Figure 4.22: Subtracted unisolated direct wave at source 10 using parameters lfilt=100, ltap=20, ntwnd=200, nxwnd=10. Blue ring highlights reflections.

Using the final parameters from figure 4.22, it is now possible to compare each of the isolation methods previously described. The results are shown in figures 4.23 through 4.26 for source 10. From these images, it seems that the unisolated wave leaves the clearest remaining direct wave, as marked by the blue rings in figure 4.25 and 4.26. The unisolated direct wave also seems to remove some weak reflections, marked by red rings in figures 4.23 and 4.26, which are most clearly visible when only bandpass filtering is applied. The subtraction using the mute-isolated direct wave supresses the direct wave efficiently, but also leaves weaker reflections than bandpass filtering alone (green rings in figures 4.23 and 4.24). Thus, it seems that bandpass filtering alone gives the best subtracted result.

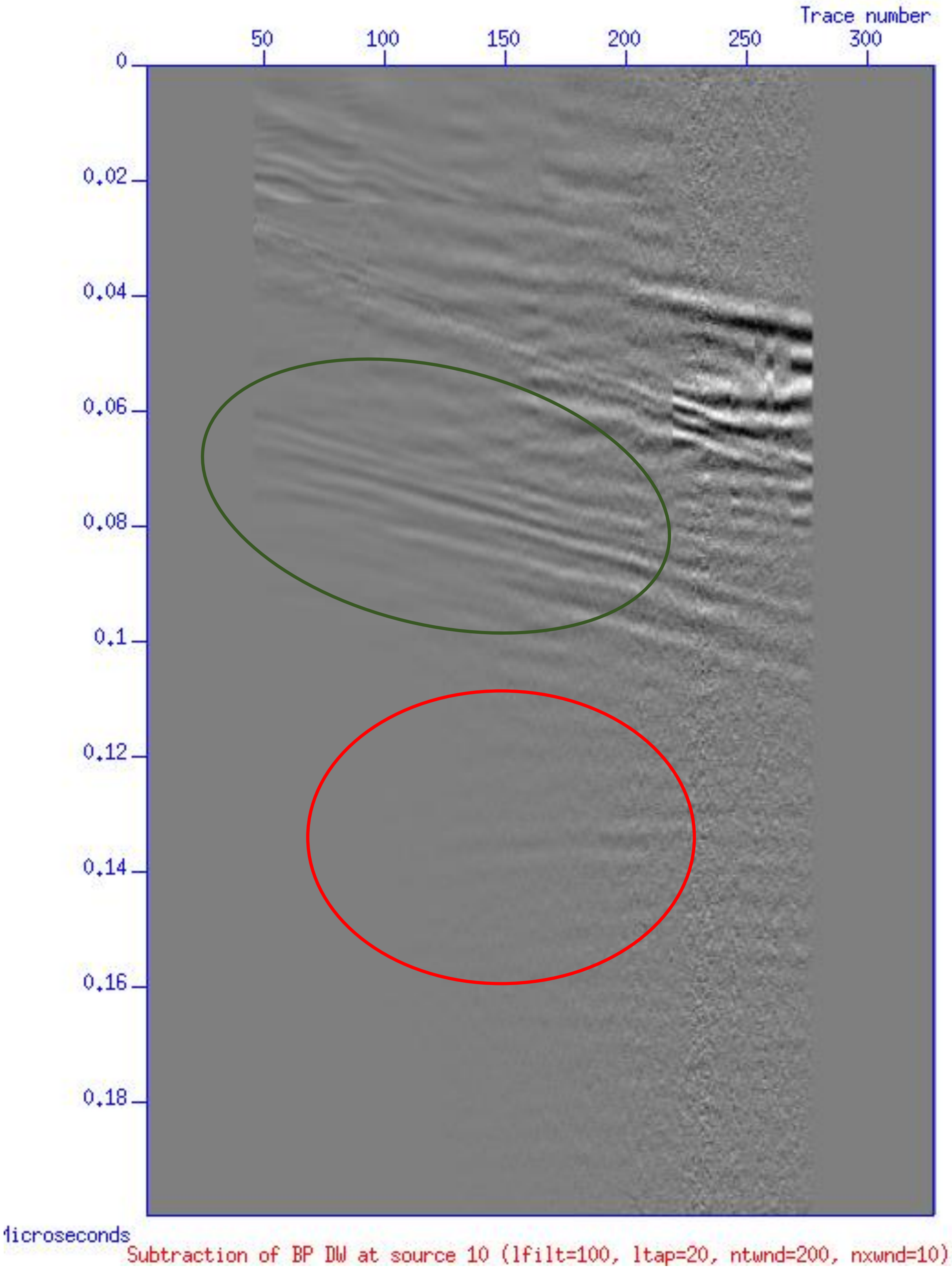

Figure 4.23: Subtracted bandpass filtered direct wave at source 10. Red ring highlights clear reflections. Green ring highlights clear reflection.

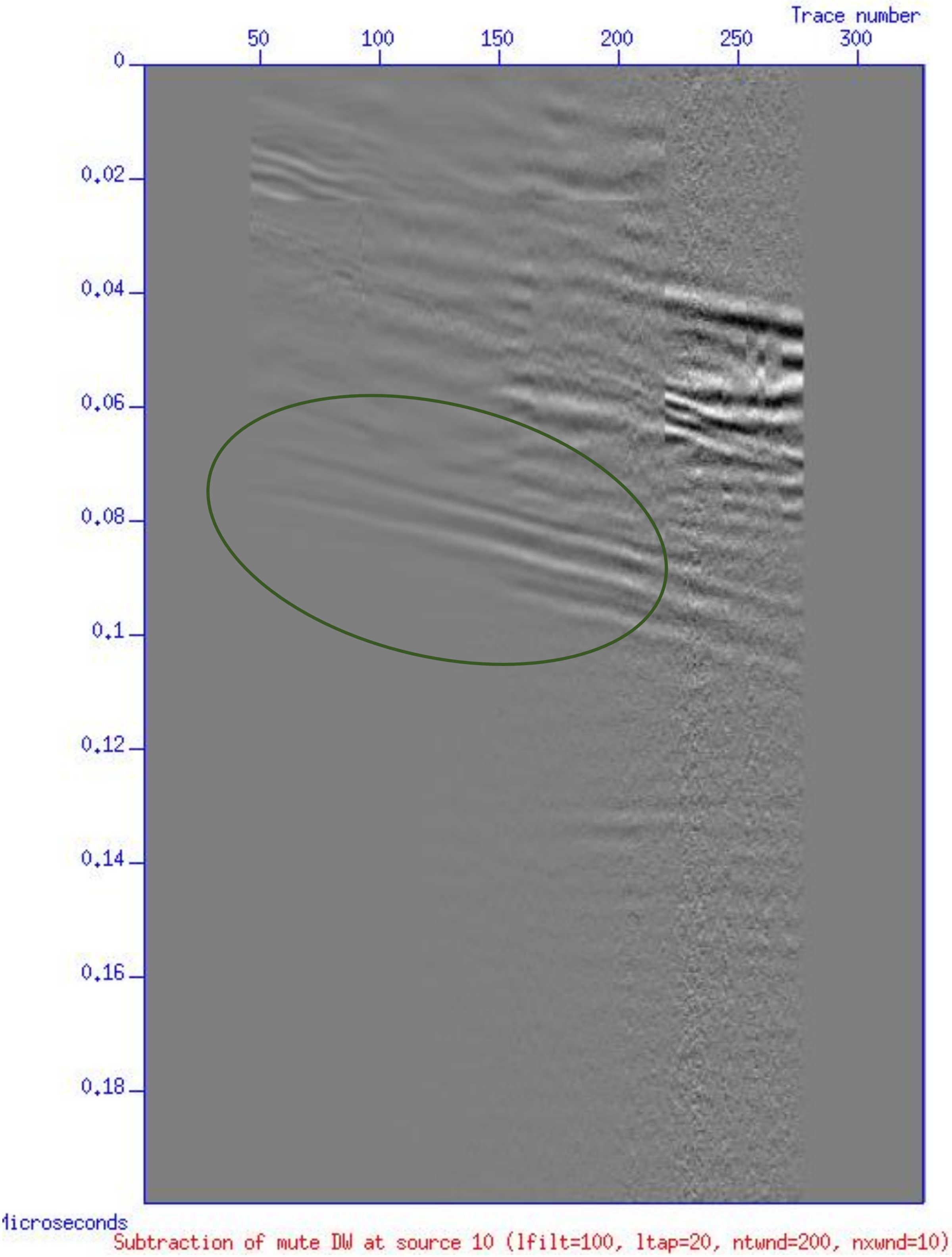

Figure 4.24: Subtracted mute-filtered direct wave at source 10. Green ring highlights reflection.

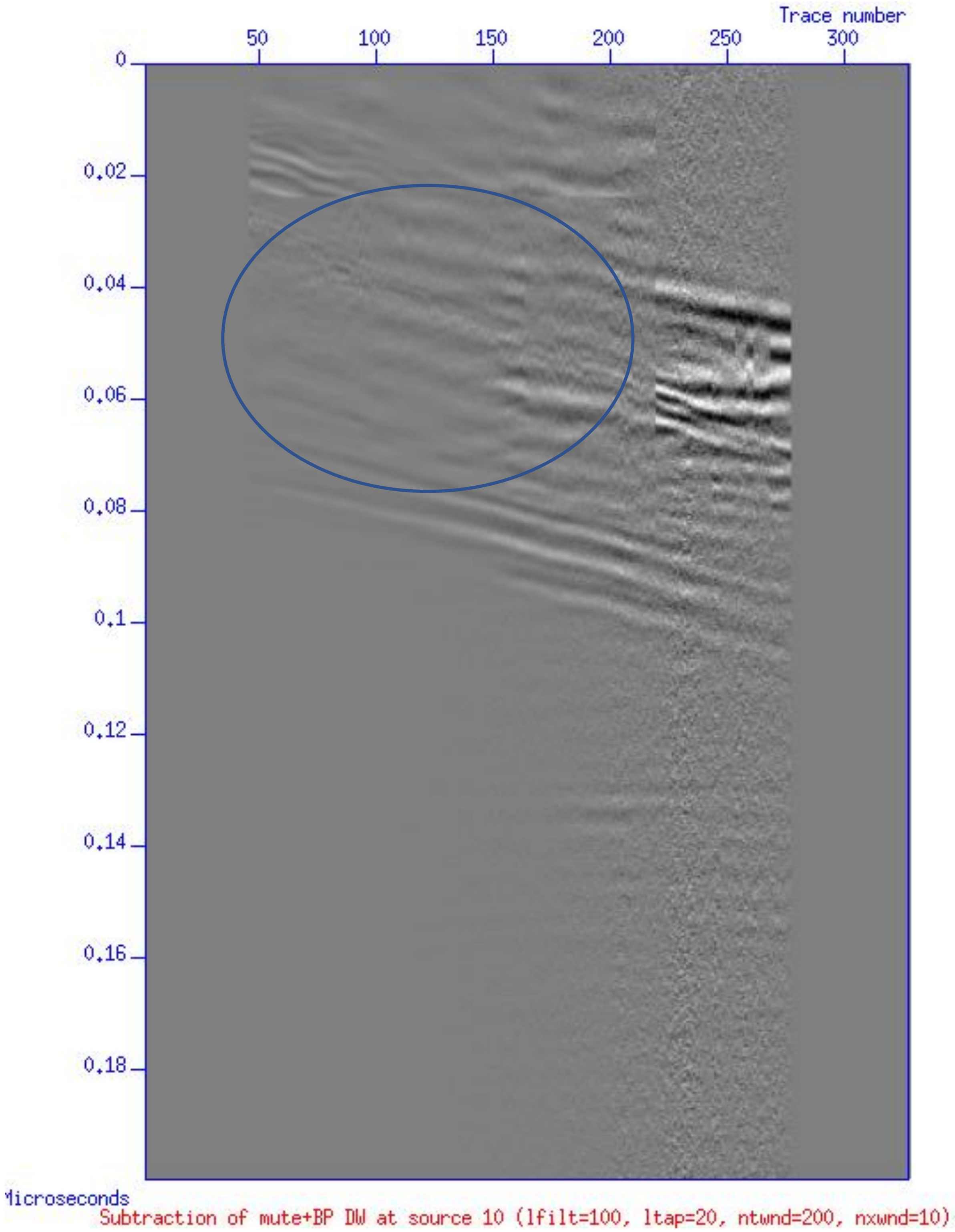

Figure 4.25: Subtracted muted and bandpass-filtered direct wave at source 10. Blue ring highlights effective suppression of the direct ground wave.

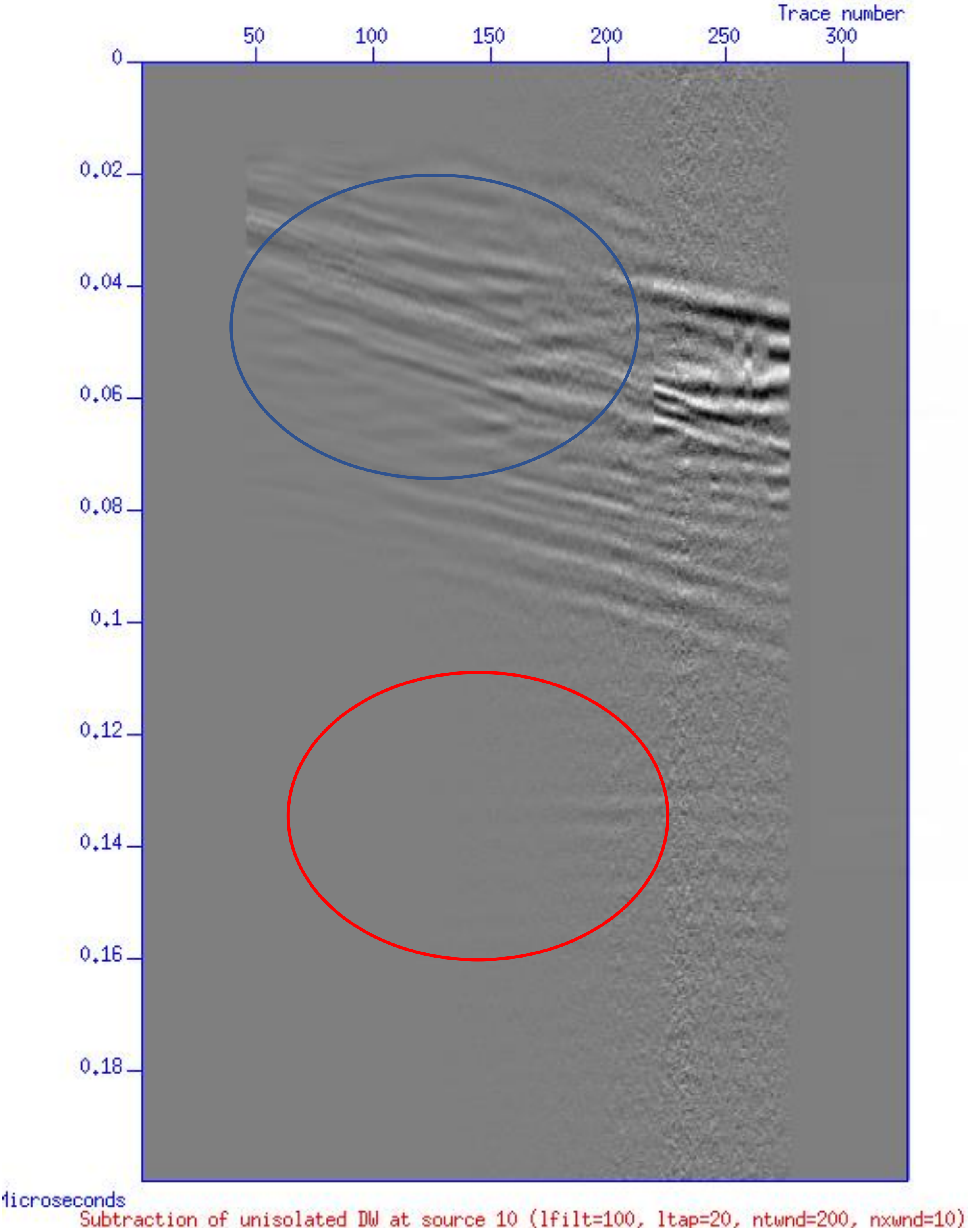

Figure 4.26: Subtracted unisolated direct wave at source 10. Red ring highlights dim reflections. Blue ring highlights region of suppressed direct ground waves.

We may also compare the results from EMI and AS to results of simple topmuting of the direct waves. Figure 4.27 shows the dewowed data from source 10 after a topmute has been applied below the ground wave. Here, the reflections visible at around 0.14 micorseconds in the subtraction results are nearly invisible, and they can only be clearly seen when the image is clipped to 99% of the maximum amplitude (figure 4.28). In addition, the topmute simply hides reflections that may be present behind the direct waves.

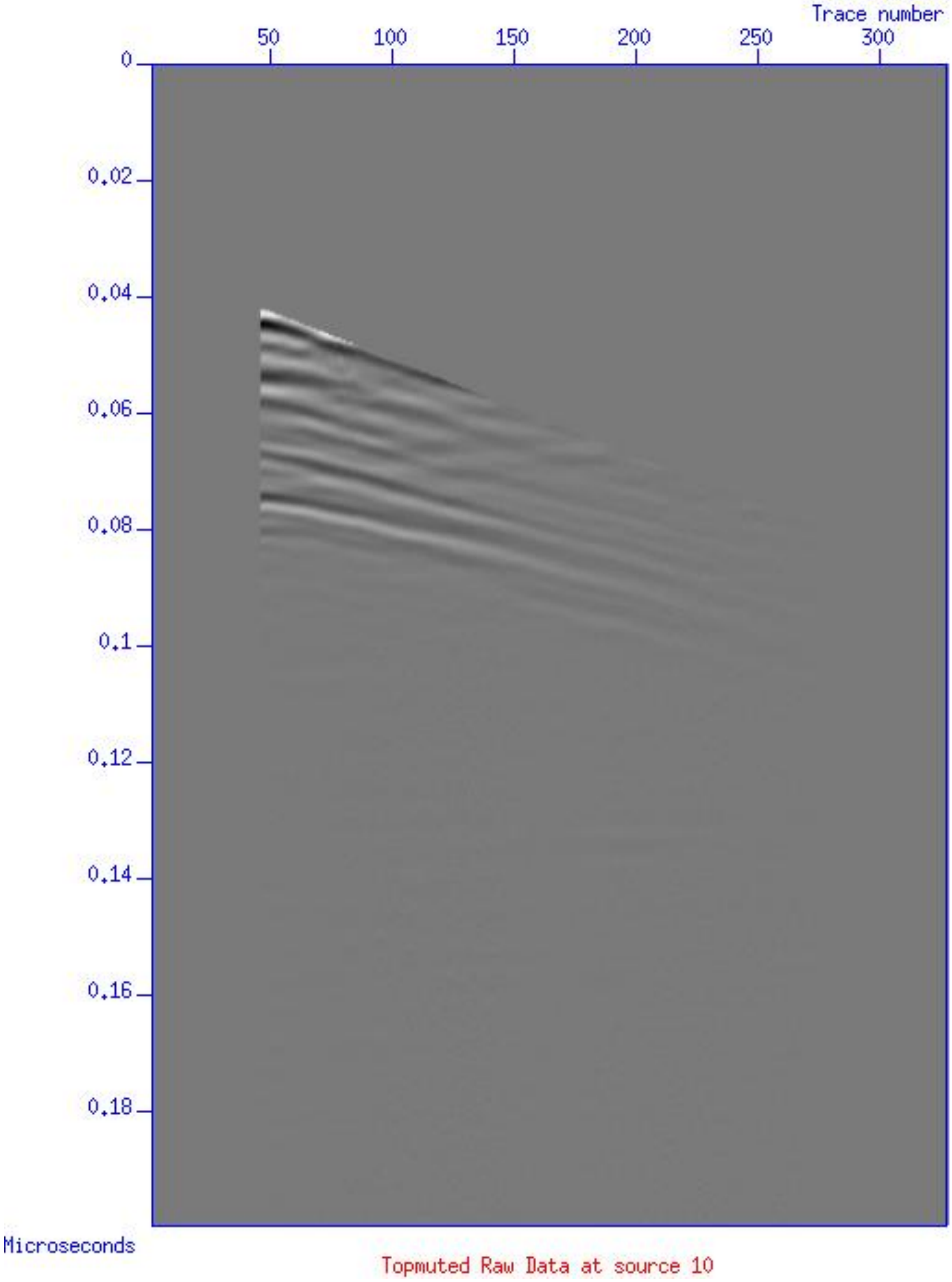

Figure 4.27: Raw data at source 10 with a topmute applied below the ground wave.

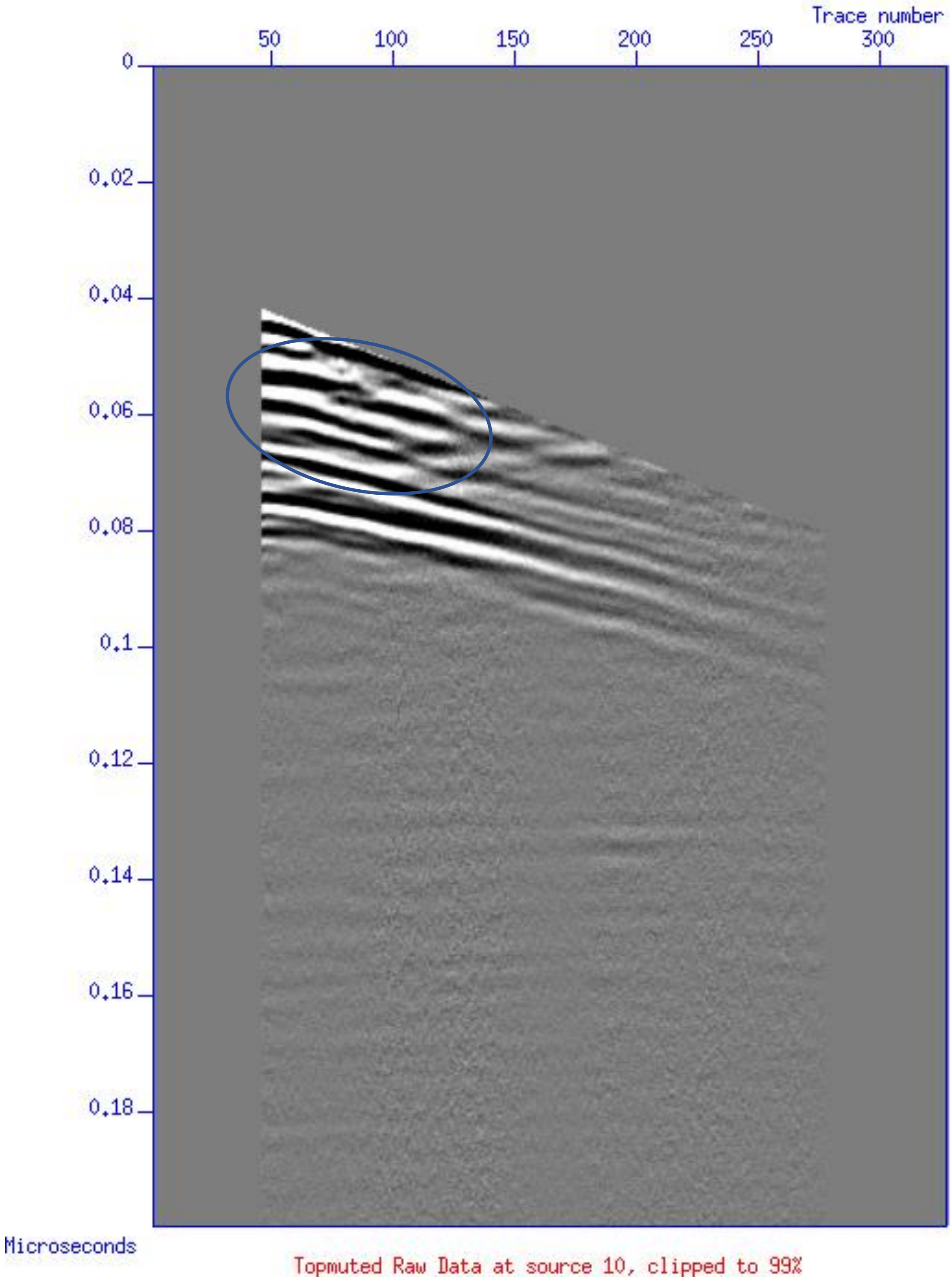

Figure 4.28: Topmuted raw data at source 10, clipped to 99%. Blue ring marks reflections.

Figure 4.29 shows the final subtraction result clipped to 90% of the maximum amplitude. Here, noticable blurring is observed between trace numbers 45 and 125, below an arrival time of 0.09 microseconds (indicated in figure 4.29 with an arrow). The cause of this blurring is difficult to tell, though if the nearly horizontal reflections in this region are indeed due to a fencepost, this area is of little interest. However, comparing figure 4.29 to figure 4.28, there seems to be some reflections which have been suppressed during the subtraction, marked by the blue ring in both images. Since these reflections cannot be retrieved by EMI, and indeed do not appear in the retrieved direct wave seen in figure 4.17, this may be attributed to AS, suggesting more work should be carried out in order to determine the optimal AS parameters.

The final process is summarised in figure 4.30.

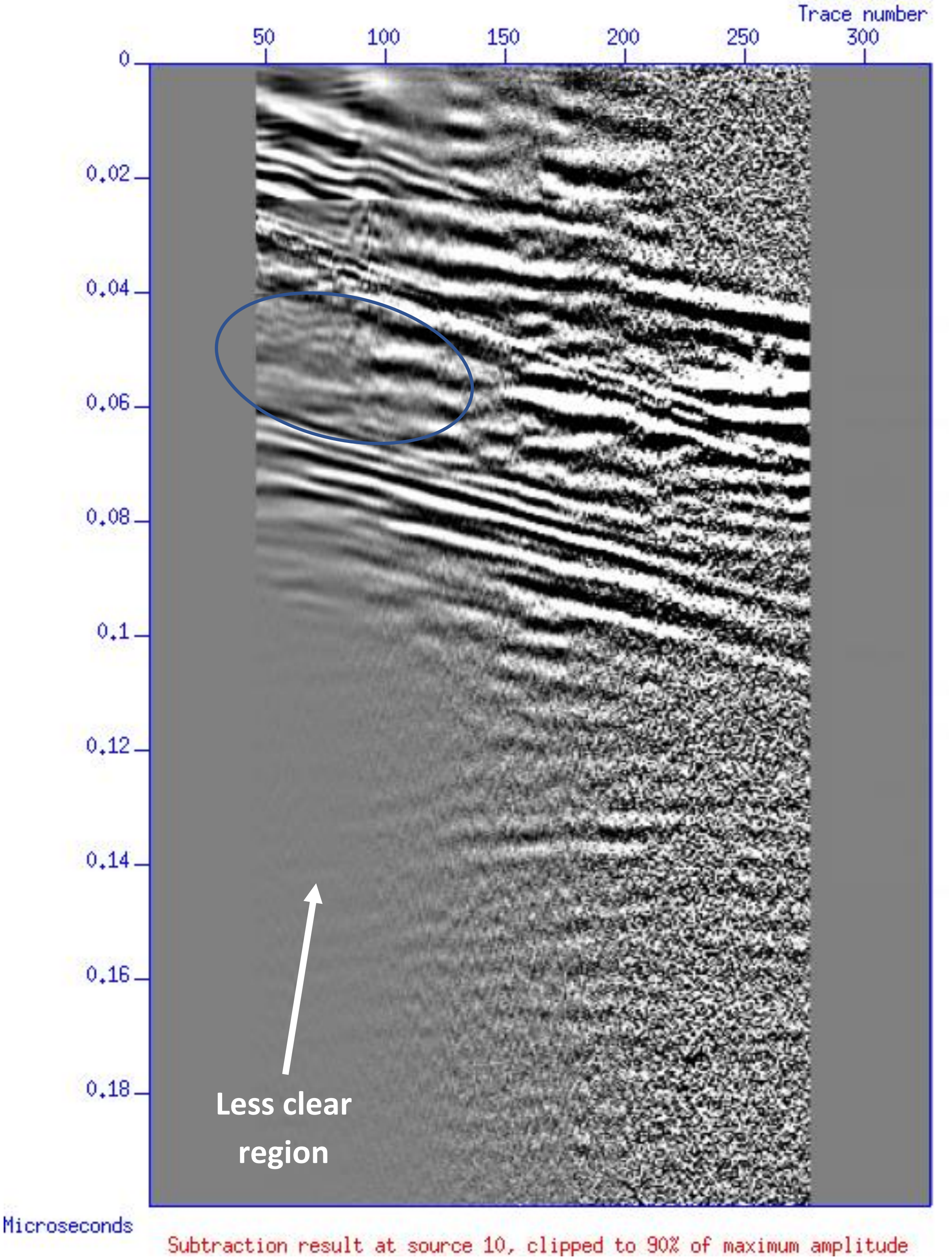

Figure 4.29: Subtracted data at source 10, clipped to 90%. Blue ring marks lack of reflections present in figure 4.28.

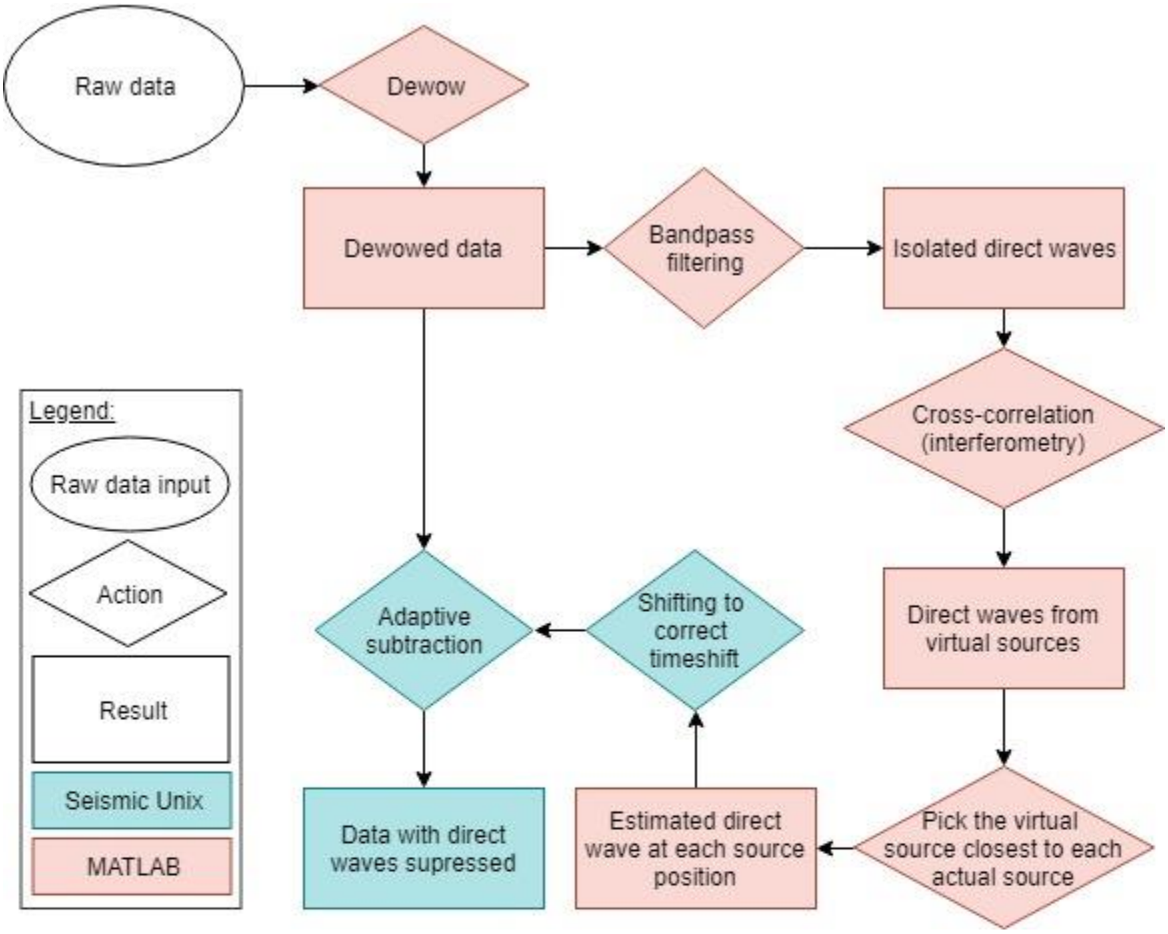

Figure 4.30: Summary of multiple-offset GPR data processing to supress direct waves using EMI and AS.

4.2.2 Stacking

Following the EMI+AS procedure described in the previous section, both the dewowed data and the subtraction results were sorted into common midpoint (CMP) gathers and normal moveout (NMO) correction was applied. Each set of data was then stacked: the stacked raw data is seen in figure 4.31, and the stacked subtraction result in seen in figure 4.32, each clipped to 99% of the maximum amplitude. Both images are less reliable from CMP 200 to 422, due to a low fold. This is noticable as figure 4.31 barely has any visible reflections in this region, while figure 4.32 shows a high degree of aliasing in the same region. As a consequence, it is difficult to indentify the presence of the trench or the cadaver in either section. However, the images show that the direct waves have been suppressed very effectively (red ring) by EMI+AS, while the signature of the main reflection seen between 0.06 and 0.08 microseconds (blue ring) has been maintained.

It is important to note that as a result of picking the closest virtual source to each actual source for the AS step, the first eight source positions all have the same retrieved direct wave (from the virtual source at the very first receiver position). Though this means the subtraction result for these eight sources is not ideal, they are still used in the stacking. It could be interesting to investigate whether using the raw data for these sources would give a better stacked section. Similarly, the stacked section for the subtraction results would be different if the unsubtracted region at large offsets was muted for each source position, though it would be at the cost of fold, and this would also be interesting to investigate.

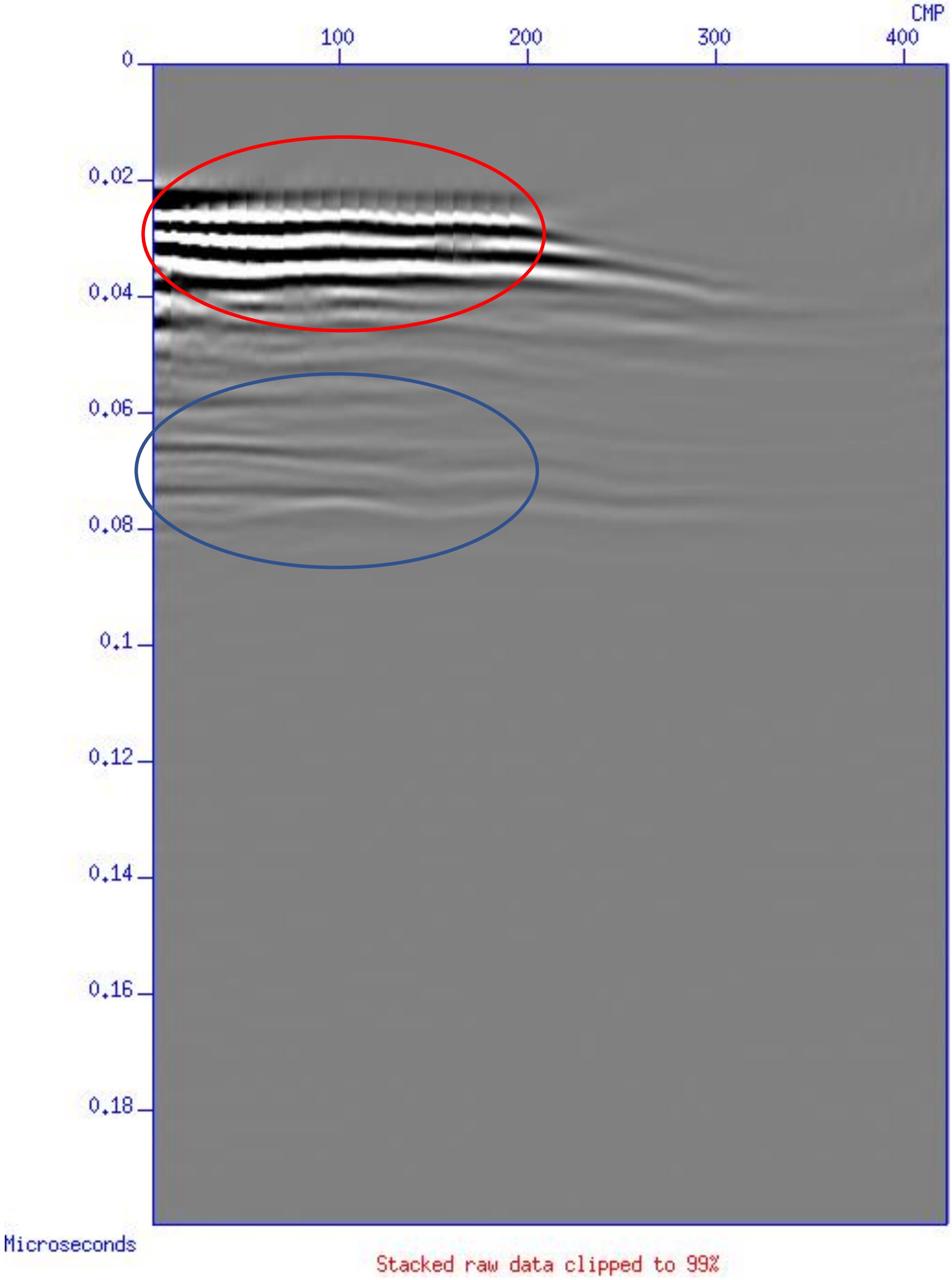

Figure 4.31: Stacked raw data, clipped to 99%. Red ring highlights direct wave. Blue ring highlights main reflection.

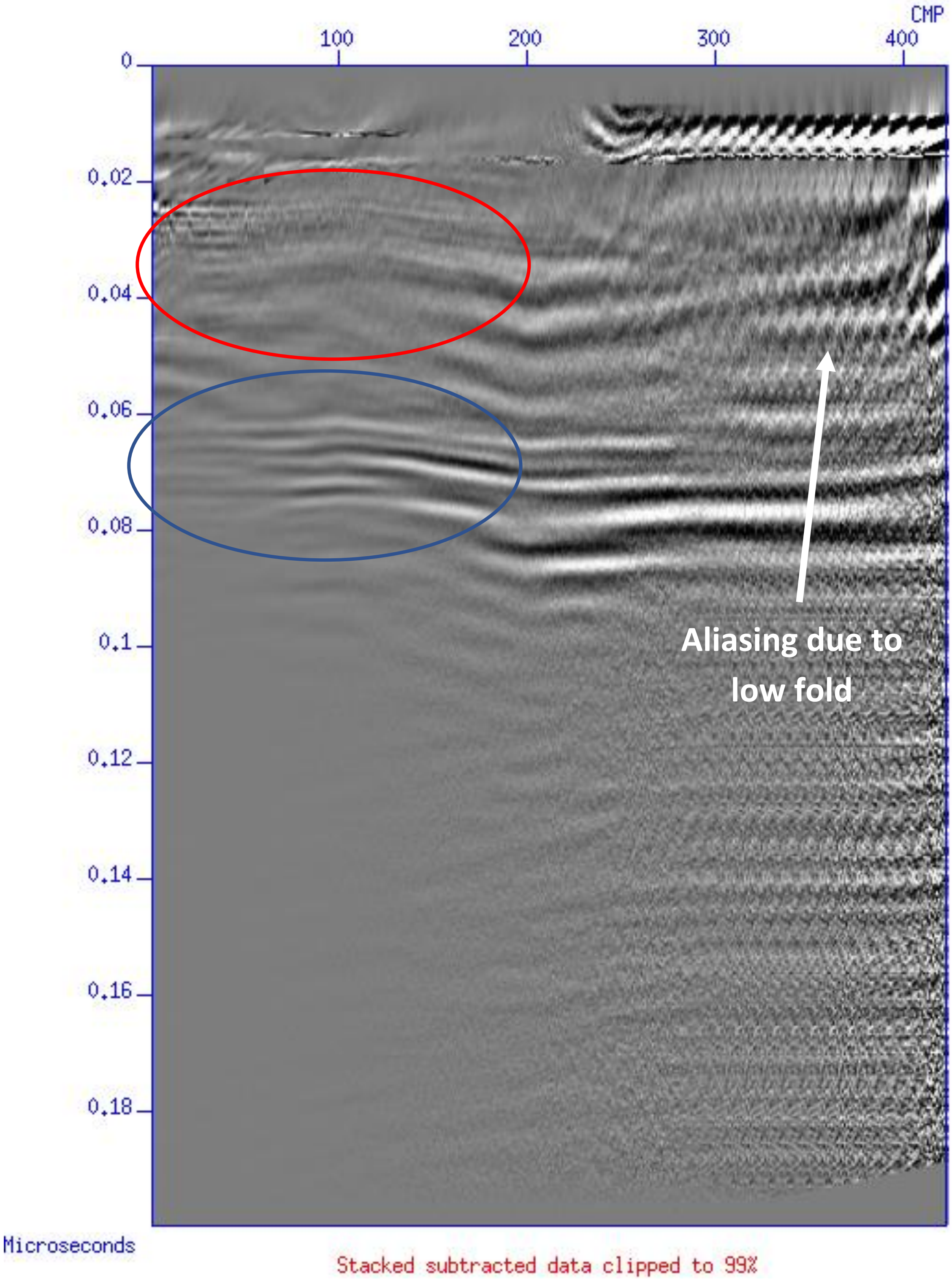

Figure 4.32: Stacked subtraction results, clipped to 99%. Red ring highlights direct wave. Blue ring highlights main reflection.

5. Discussion

In this chapter the results presented in the previous chapter will be discussed with reference to the sub-questions presented in the introduction. First, the sub-questions of the “side investigation” at the TU Delft site will be evaluated, after which the main questions will be discussed. The recommendations for future research will be discussed separately in chapter 7.

5.1 Redefinition of TU Delft Investigation Site Target Locations

In redefining the positions of the buried targets placed during the investigation of 2018, several features of the 250-MHz common-offset data collected at the site were noticed. The 250-MHz antenna was chosen based on the recommendations of the previous theses, stating that the 250-MHz antenna would be less noisy at the site, and that it would act as a “filter” for most smaller objects (roots) due to the lower resolution. This was ideal for the purpose this year, as it would encourage the identification of the barrel locations. However, it seemed that several new signals were present this year, which were not present previously. One such artefact was a long, straight, and strong signal, which resembles a pipe more than any kind of root.

Using the same processing steps and velocity estimate, it was possible to identify a reflection resembling the barrel containing steel rods from the previous thesis, both in signature and depth profile. Following this, the locations of the other two targets were back-calculated in order to redefine their positions. However, even having identified this object, it was difficult to identify the presence of the empty barrel and refilled pit in the 2019 dataset. The continued difficulty in locating targets despite knowing the redefined coordinates suggests the new grid may indeed have been rotated slightly with regards to the past grid, or perhaps that the empty barrel was removed without the knowledge of the authors in order to place the possible pipe. The latter is supported by the fact that this supposed pipe is not clearly visible in any of the data provided in the 2018 theses, despite being positioned within the studied grid.

5.2 Comparison of 250-MHz Antenna in Sandy vs. Silty/Clayey Soils

The use of the 250-MHz antenna at both sites investigated during this project allows for some conclusions to be drawn about the appropriateness of this choice in different settings. At the ARISTA facility, the soil was very sandy and loose, and was later found to have a relatively high velocity compared to the estimated velocity at the TU Delft site. The wave attenuation was much lower at the ARISTA facility, and the wave penetrated deeper. The resolution of the image was also lower at the ARISTA facility due to the increased velocity. All of this meant the data from the ARISTA facility was difficult to interpret at the depth of the burial.

The choice to continue using the 250-MHz antenna at the ARISTA facility was mainly based on the recommendation of the 2018 theses that this antenna would be more suited to larger and more deeply buried targets than the 500-MHz antenna. However, the difference in soil type seems to negate this conclusion, and this is supported by the theory presented in chapter two of this thesis. In addition, the soil at the ARISTA facility is much more homogeneous than at the TU Delft site, with no network of tree roots in the subsurface, meaning the 500-MHz antenna would have produced cleaner results than those seen at the TU Delft site in 2018. It seems that the 500-MHz antenna might have been a more appropriate choice of frequency for the investigation at the ARISTA facility.

5.3 Differences in 250-MHz Common-Offset GPR Data between a Clandestine Burial and a Refilled Pit

The circumstances at the ARISTA facility make it difficult to objectively compare the two graves. In the data collected over both graves, a lot of interference was seen from metal and plastic objects close by, and since the interference is not the same for both graves, it is hard to say which differences can be attributed to the grave contents, and which to the interferences.

In general, it seems that a pit will show more homogeneously layered responses, while the burial of a body may show a series of smaller hyperbolas. The clearest difference between a burial and a pit, is seen not from the targeted graves, but from burial B.2, which is located close enough to the investigated pit that it was covered during the data acquisition. Here, there is a large and clear hyperbola in B.2 where no similar signal is seen in the pit in any line. It is not certain that this constitutes a true difference, however, due to the aforementioned interference over the pit, which may have masked a similar hyperbola. The theoretical signature of a trench or grave as described in subchapter 2.1 was not observed in any grave.

In order to objectively investigate this, it would be good to place targets of investigation far from any metal fenceposts, cables, and multiplexers, as well as the plastic sheet covering the fence, which may be buried as well.

5.4 Optimal Procedure for EMI and AS of Multiple-Offset 250-MHz GPR Data

Firstly, it is important to consider the method on-site when planning to use EMI and AS to remove direct waves from data. It is important to have at least one receiver position at the same location as each true source. If this is not done, no virtual sources will be generated at the exact location of each source, and the subtraction step will have to proceed with the closest virtual source instead. This is avoided by simply choosing an initial source/receiver offset which is a multiple of the receiver separation (e.g. 0.84 m initial offset, which is a multiple of the 0.02 m receiver separation). This will not be perfect, since position and signal wavelength uncertainties, as well as topography will affect the accuracy of the source and receiver placements, but it can somewhat limit the error.

Once the data has been collected, the best method for supressing direct waves in multiple-offset GPR data is suggested to be the use of a bandpass filter to eliminate very high and very low frequencies from the data before cross-correlating and summing the traces to retrieve the direct waves. Using a hard mute around the direct waves before cross-correlating seems to be less effective at bringing out the reflections in the subsurface than simply leaving the input unmuted. In addition, it may be argued that applying a top- and bottom-mute using estimated velocities for the direct waves means the method is no longer completely data-driven. However, leaving the input direct waves completely unisolated appears the least effective at suppressing the direct waves in the final result, all other variables kept equal.

The optimum parameters for AS may vary between datasets, as it depends on the number and size of time samples, number of traces, and signature of the wave to be removed. The AS parameters reached in this thesis could be further optimised, since it seems some reflections were suppressed during this step. Further investigation is required in order to confirm this.

5.5 Effectiveness of using EMI and AS to Remove Direct Waves from Multiple-Offset GPR Data

The method of using EMI to retrieve direct waves at each source location and using AS to remove these from the initial data has some merits. It may be seen in all variants of the subtracted results (using mute-isolated direct waves, bandpass-isolated direct waves, both, or neither) that the direct waves are suppressed in the final result, and reflections are visible underneath their original positions. In addition, EMI and AS are shown to be useful for highlighting weak reflections in comparison to simply topmuting the direct waves.

The large initial offset of at least 0.83 m makes it difficult to apply this method to GPR data, since the first eight source positions will have no corresponding virtual source because no receivers are present in this interval. The closest virtual source to all these first eight sources is the virtual source created at the first receiver position. This means that when it comes to stacking, although 20 source positions were used for the line investigated in this project, only 12 have had the direct waves suppressed in the ideal manner. In addition to this, the limitation of receiver positions per line gathered due to the length of the cable sets a restriction on the number of common midpoints in the data, another disadvantage when it comes to stacking the data. It must also be considered that with the high degree of interference from metal objects in the common-offset data, it is assumed that this interference will be present in the multiple-offset data as well.

Due to these factors, many further investigations are required in order to determine the most appropriate procedure for stacking, such as whether it is better to use raw data in place of the first eight source positions, and whether muting the region of unsuppressed direct waves at large offsets in each source position has a positive effect on the stacked result.

6. Conclusion

This thesis serves as a continuation of a collaboration between Delft University of Technology and the Netherlands Forensic Institute which is still in very early stages. As such, the scope of the thesis is broad, and many questions are raised during this investigation. It is the hope of the author that the questions answered as well as the ones raised during this report will help bring some additional focus to future work in this line of research.

Common-offset GPR data was collected at the TU Delft site with the goal of encouraging long-term research of stashes buried under criminal intent and the location of these using geophysical methods. Common-offset GPR data was collected at the ARISTA facility in order to investigate the differences between a clandestinely buried human corpse and a refilled empty pit. In addition, multiple-offset GPR data was collected along several lines at both investigation sites, and one of these was processed using electromagnetic interferometry and adaptive subtraction in order to explore the possibilities of this method for GPR data.

The positions of the targets buried in during the theses written in 2018 were redefined in a new grid. This was done by comparing the common-offset 250-MHz GPR results from the previous year to new results which were processed using the same processing steps. A reflection which seems very similar in signature and depth profile to the barrel containing steel rods in the 2018 theses was identified, and based on this, new coordinates were defined for the target locations. However, despite knowing the redefined locations of the targets, they were difficult to identify in the data, in particular due to an apparently new reflection close to the supposed position of the empty barrel. It may be possible that some construction work has been done near the area in the past year, or that the new grid is rotated from that of the previous year.

The choice of using the 250-MHz antenna at the ARISTA facility was taken for granted, and it appears that the 500-MHz antenna may have been more appropriate for the site, due to a higher velocity in cleaner and drier sand, which led to an estimated penetration three times greater than the maximum grave depths. In addition, the resolution was decreased, and it was difficult to compare the reflections of the burial and the pit due to this. However, the choice of frequency was not the only limiting factor at the ARISTA facility. Several metal objects and distinct trenches were present in close proximity to the two target graves, and a high degree of interference was seen in almost all lines of common-offset data collected. The clearest evidence of a difference in GPR response between a clandestine burial and a refilled pit came from a nearby burial which was included in the data by proximity alone. Even for this nearby burial, no pit clear of interference was available to compare with.

An optimal procedure for using EMI and AS to remove direct waves from multiple-offset GPR data was suggested using bandpass filtering of the data to remove very high and very low frequencies before cross-correlating the traces to retrieve the direct wave. This method appears better than performing no isolation of the direct waves before EMI, and also better than applying a hard mute around the direct wave region. It is shown that EMI and AS are effective at supressing the direct waves in a stacked multiple-offset GPR section, and effectively enhance the reflections present in the subsurface. However, more analysis should be completed in order to determine the best parameters for the AS, as well as the optimal procedure for stacking the subtraction results.

7. Recommendations for Further Work

Several recommendations can be made for anyone wishing to continue this line of research. At the TU Delft site, it may be worth digging a small hole at the location of the seemingly new reflection in order to see whether a pipe has indeed been placed there. It is highly recommended to initiate a more formal investigation area, with more varying targets and soil conditions and consistent logging of coordinates.

At the ARISTA facility, it will be difficult to justify a continuation of GPR investigations as long as the graves are so close to so many sources of interference. We advise returning with the 500-MHz GPR and repeating the investigation, in order to see whether a higher resolution might encourage the distinction between interference and actual differences between a pit and a grave. If additional graves will be created, we advise that they be placed as far from the fences as possible, and with as few sensors and cables as possible, especially if electromagnetic methods are to be evaluated in greater detail.

One issue encountered often during the analysis of the collected data, was the need for more information about the graves at the ARISTA facility. Moisture content and temperature in the grave could have helped shed additional light on the decomposition state of the body, the size of the body could have given a better estimate of the causes of each reflection (since the human body is not a 1 m x 2 m x 0.3 m block), and the exact placement of sensors and cables could have been helpful when determining specific sources of interference. Site geology, and sand thickness, placement, and method of compaction would all be interesting to consider. Even specific elevation data of the graves could have been useful. All this data is available, and we hope the next group working on this will have greater access to the baseline data than we had. Transparent data archiving and sharing is necessary for this kind of interdisciplinary project.

Finally, a few notes about the multiple-offset GPR set-up. As mentioned in this thesis, limitations in possible equipment configurations could cause issues during the data processing, both during the adaptive subtraction and stacking of the data. Using the 500-MHz antenna would already reduce the initial offset between the source and receiver, but having a longer cable connecting the receiver to the odometer would allow a further reduction of this distance as well. Then the receiver could be placed on the opposite side of the frame from the odometer, and could be placed with no additional separation from the transmitter other than the fixed separation already present in the common-offset set-up. In addition to this, a longer cable between the transmitter and receiver would allow more receiver positions and increase the fold during stacking. More source positions are also recommended in order to extend the section.

References

Berard, B. A., & Maillol, J. M. (2007). Multi-offset ground penetrating radar data for improved imaging in areas of lateral complexity - Application at a Native American site. *Journal of Applied Geophysics*, *62*(2), 167–177. https://doi.org/10.1016/j.jappgeo.2006.10.002

Bradford, J. H. (2007). Frequency-dependent attenuation analysis of ground-penetrating radar data. *Geophysics*, *72*(4), J7–J16. https://doi.org/10.1190/gpysa7.72.y3_1

Buekenhout, I., Cravo, L., Vieira, D. N., Cunha, E., & Ferreira, M. T. (2018). Applying standardized decomposition stages when estimating the PMI of buried remains: reality or fiction? *Australian Journal of Forensic Sciences*, *50*(1), 68–81. https://doi.org/10.1080/00450618.2016.1212268

Ceciliason, A. S., Andersson, M. G., Lindström, A., & Sandler, H. (2018). Quantifying human decomposition in an indoor setting and implications for postmortem interval estimation. *Forensic Science International*, *283*, 180–189. https://doi.org/10.1016/j.forsciint.2017.12.026

Daniels, D. J. (David J. . (2004). *Ground penetrating radar*. London : Institution of Electrical Engineers.

Dong, S., He, R., & Schuster, G. T. (2006). Interferometric predcition and least squares subtraction of surface waves, 2783–2786. https://doi.org/10.1190/1.2370102

Forte, E., & Pipan, M. (2017). Review of multi-offset GPR applications: Data acquisition, processing and analysis. *Signal Processing*, *132*, 210–220. https://doi.org/10.1016/j.sigpro.2016.04.011

Galloway, A., Birkby, W. H., Jones, A. M., Henry, T. E., & Parks, B. O. (1989). Decay Rates of Human Remains in an Arid Environment. *Journal of Forensic Sciences*, *34*(3), 12680J. https://doi.org/10.1520/jfs12680j

Goodman, D., & Piro, S. (Salvatore). (2013). *GPR remote sensing in archaeology*. Springer.

Google Maps. (2019). Google Maps. Retrieved from https://www.google.com/maps/@52.292784,4.9498591,638m/data=!3m1!1e3

Hansen, J. D., Pringle, J. K., & Goodwin, J. (2014). GPR and bulk ground resistivity surveys in graveyards: Locating unmarked burials in contrasting soil types. *Forensic Science International*, *237*, e14–e29. https://doi.org/10.1016/J.FORSCIINT.2014.01.009

Harms, K. (2018). GPR and EM Responses to Buried Clandestine Forensic Objects in Wet and Dry Soil Conditions, (July).

Hayman, J., & Oxenham, M. (2016). *Human Body Decomposition*. *Human Body Decomposition*. https://doi.org/10.1016/C2015-0-00038-7

Jol, H. M. (Harry M. . (2009). *Ground Penetrating Radar Theory and Applications.* Amsterdam, Netherlands ; Elsevier.

Killam, E. W. (2004). *The Detection of Human Remains.* Charles C Thomas Publisher, LTD. Retrieved from https://books.google.nl/books/about/The_Detection_of_Human_Remains.html?id=Fixwh4j8b6kC&redir_esc=y

Konstantaki, L. A., Draganov, D., Ghose, R., & Heimovaara, T. (2015). Seismic interferometry as a tool for improved imaging of the heterogeneities in the body of a landfill. *Journal of Applied Geophysics*, *122*, 28–39. https://doi.org/10.1016/j.jappgeo.2015.08.008

Liu, J., Draganov, D., & Ghose, R. (2018). Seismic interferometry facilitating the imaging of shallow shear-wave reflections hidden beneath surface waves. *Near Surface Geophysics*, *16*(3), 372–

382. https://doi.org/10.3997/1873-0604.2018013

Møller, I. (2006). Ground Penetrating Radar. In *Groundwater Resources in Buried Valleys: A Challenge for Geosciences* (pp. 99–105). Hannover: BurVal Working Group. https://doi.org/10.1016/B978-0-12-394807-6.00179-9

pdok. (2019). Dataset: Basic registration Topography (BRT) TOPNL. Retrieved from https://www.pdok.nl/introductie/-/article/basisregistratie-topografie-brt-topnl

Pringle, J. K., Jervis, J., Cassella, J. P., & Cassidy, N. J. (2008). Time-Lapse Geophysical Investigations over a Simulated Urban Clandestine Grave*. *Journal of Forensic Sciences*, *53*(6), 1405–1416. https://doi.org/10.1111/j.1556-4029.2008.00884.x

Salsarola, D., Poppa, P., Amadasi, A., Mazzarelli, D., Gibelli, D., Zanotti, E., … Cattaneo, C. (2015). The utility of ground-penetrating radar and its time-dependence in the discovery of clandestine burials. *Forensic Science International*, *253*, 119–124. https://doi.org/10.1016/j.forsciint.2015.06.006

Schotsmans, E. M. J., Márquez-Grant, N., & Forbes, S. L. (Eds.). (2017). *Taphonomy of Human Remains: Forensic Analysis of the Dead and the Depositional Environment*. Chichester, UK: John Wiley & Sons, Ltd. https://doi.org/10.1002/9781118953358

Slob, E., & Wapenaar, K. (2007). General representations of electromagnetic interferometry. In *2007 4th International Workshop on, Advanced Ground Penetrating Radar* (pp. 8–11). IEEE. https://doi.org/10.1109/AGPR.2007.386515

Slob, Evert, & Wapenaar, K. (2008). *Practical representations of electromagnetic interferometry for GPR applications: a tutorial*. *Near Surface Geophysics*. Retrieved from http://homepage.tudelft.nl/t4n4v/Daylight2/NSG_08.pdf

Vroom, A. (2018). The Potential of Geophysical Instruments as Tools for Forensic Searches.

Wapenaar, K., Draganov, D., Snieder, R., Campman, X., & Verdel, A. (2010). Tutorial on seismic interferometry: Part 1 — Basic principles and applications. *Geophysics*, *75*(5), 75A195-75A209. https://doi.org/10.1190/1.3457445

Appendix A

This appendix presents the complete results of the common-offset GPR data collection at both investigation sites, as well as a table of corresponding grid lines between the pit and burial grids at the ARISTA facility. The legend shown in figure 4.9 applies to figures A.1 through A.27.

Table A.1: Corresponding grid lines at the ARISTA facility in the X-direction.

Pit	Burial
Y=3.00	Y=0.00
Y=2.75	Y=0.25
Y=2.50	Y=0.50
Y=2.25	Y=0.75
Y=2.00	Y=1.00
Y=1.75	Y=1.25
Y=1.50	Y=1.50
Y=1.25	Y=1.75
Y=1.00	Y=2.00
Y=0.75	Y=2.25
Y=0.50	Y=2.50
Y=0.25	Y=2.75
Y=0.00	Y=3.00

Table A.2: Corresponding grid lines at the ARISTA facility in the Y-direction.

Pit	Burial
X=3.00	X=3.00
X=2.75	X=2.75
X=2.50	X=2.50
X=2.25	X=2.25
X=2.00	X=2.00
X=1.75	X=1.75
X=1.50	X=1.50
X=1.25	X=1.25
X=1.00	X=1.00
X=0.75	X=0.75
X=0.50	X=0.50
X=0.25	X=0.25
X=0.00	X=0.00

Figure A.1: Line X=0.00 for both graves, 2019.

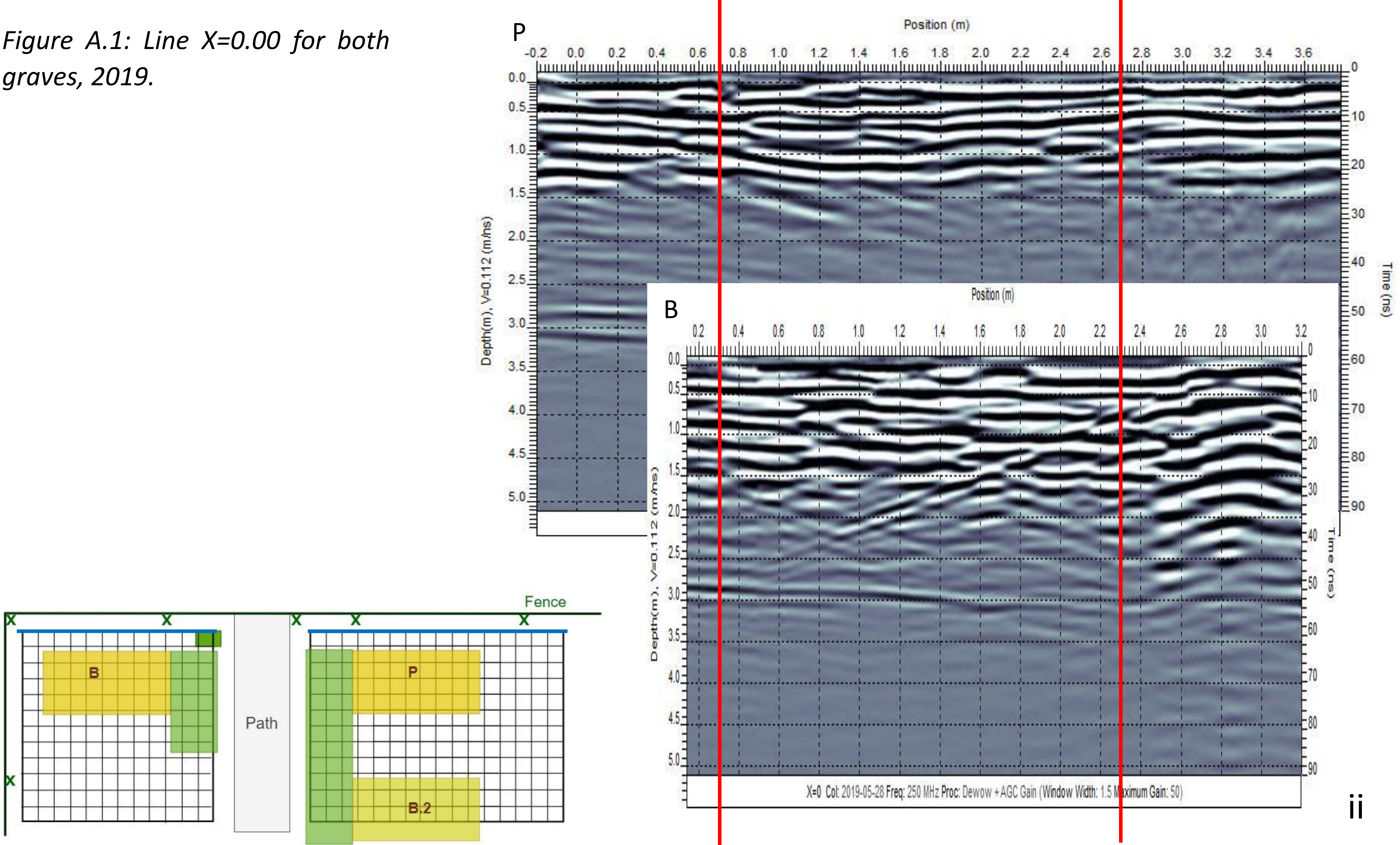

Figure A.2: Line X=0.25 for both graves, 2019.

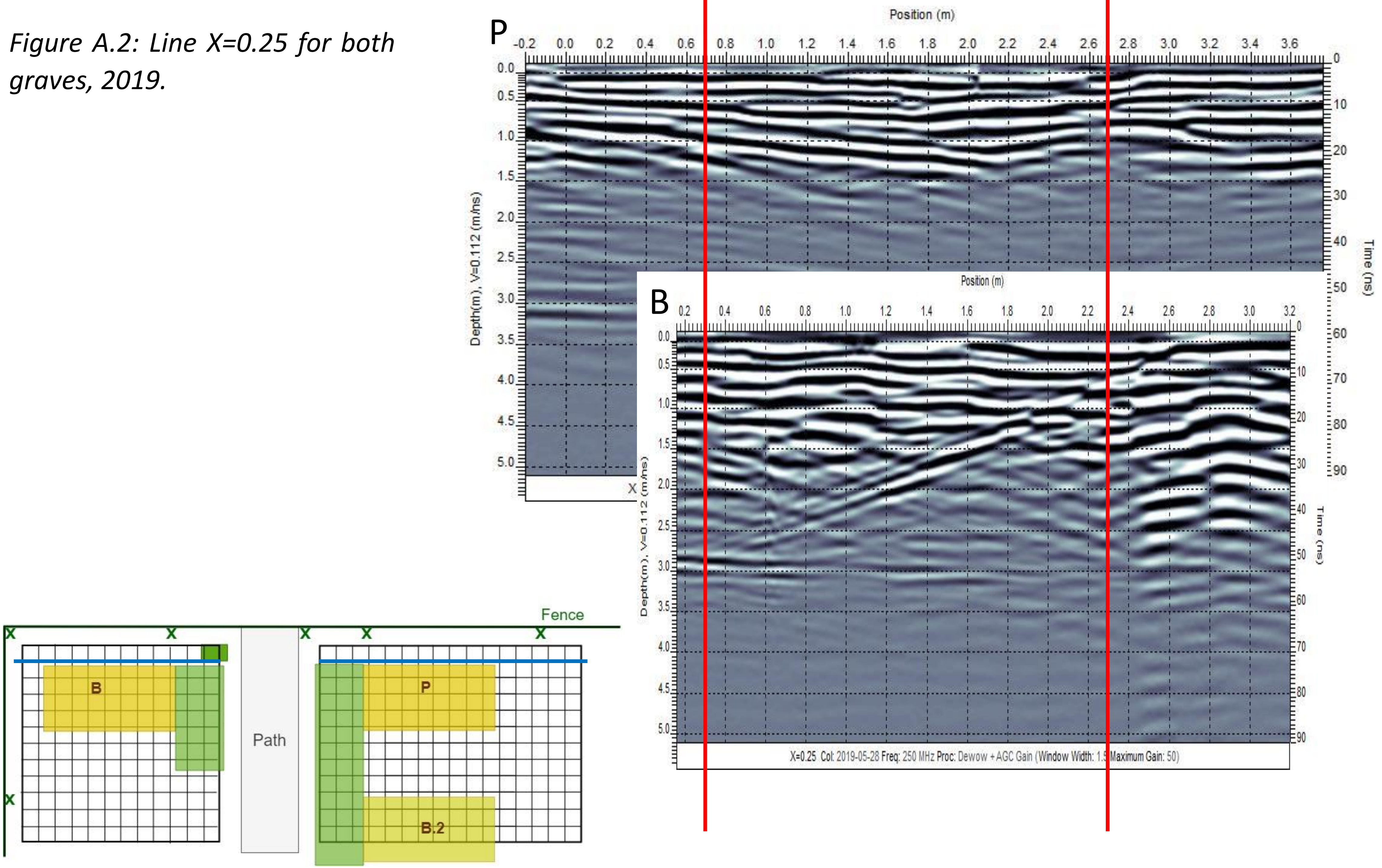

Figure A.3: Line X=0.50 for both graves, 2019.

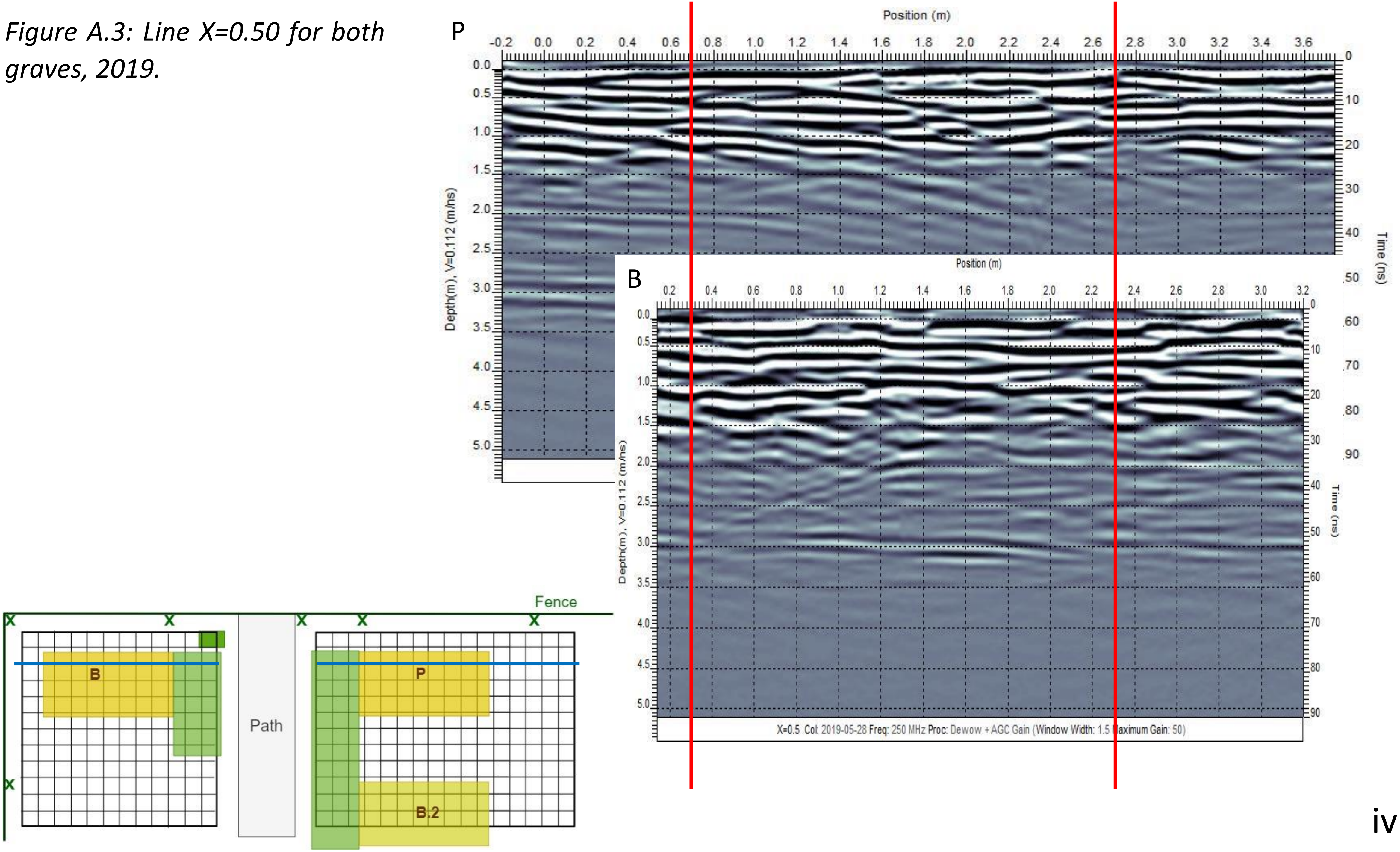

Figure A.4: Line X=0.75 for both graves, 2019.

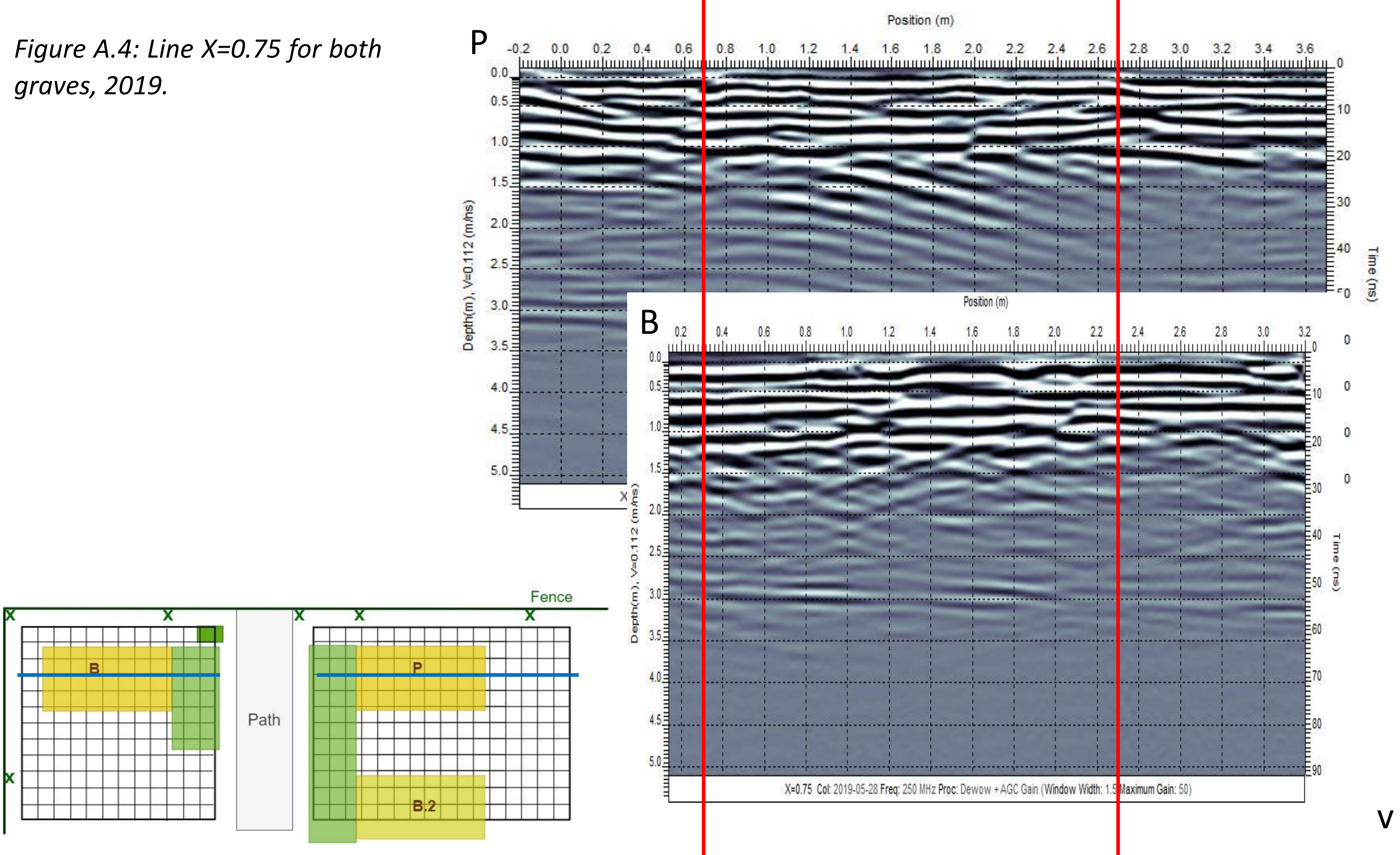

Figure A.1: Line X=1.00 for both graves, 2019.

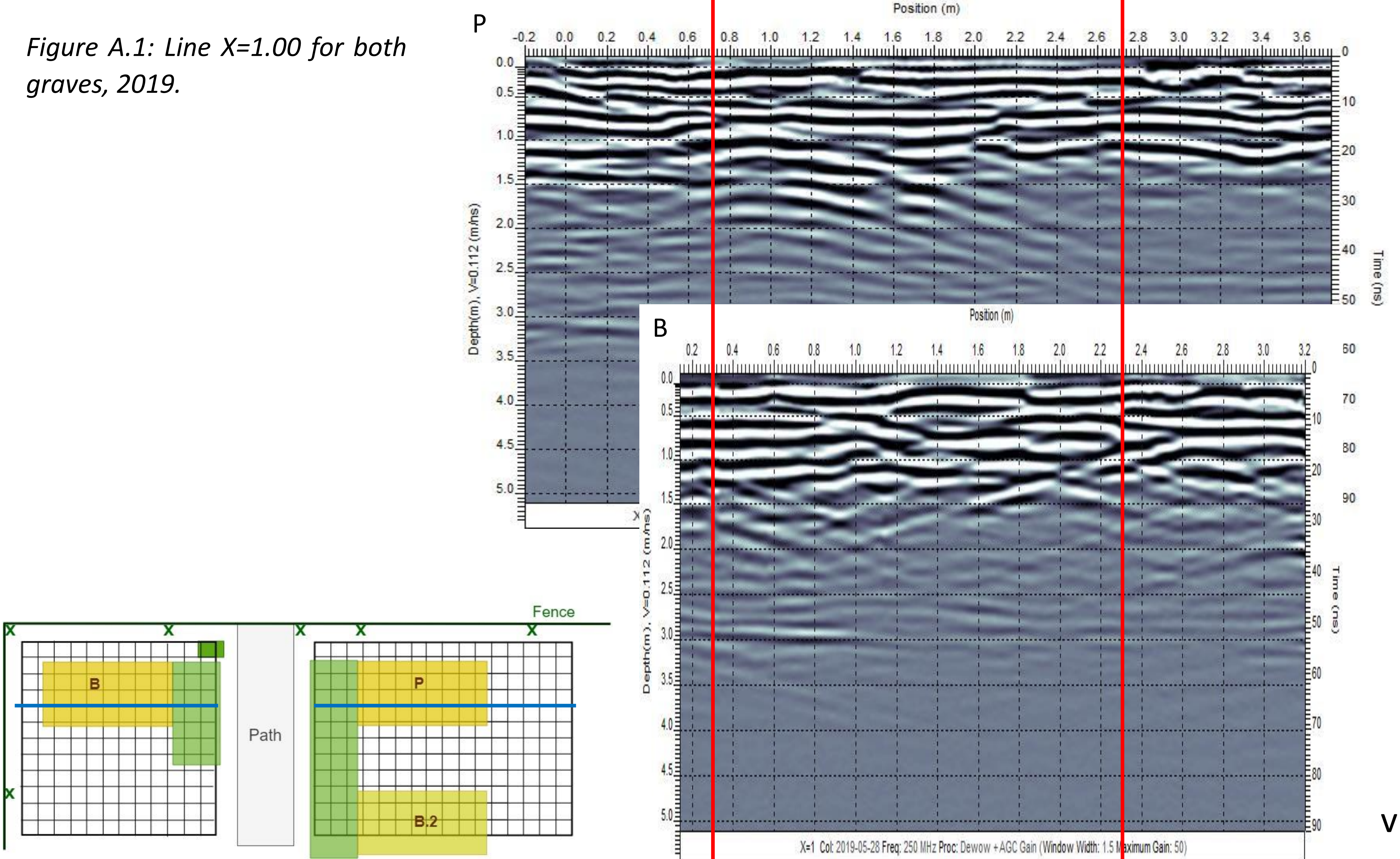

Figure A.6: Line X=1.25 for both graves, 2019.

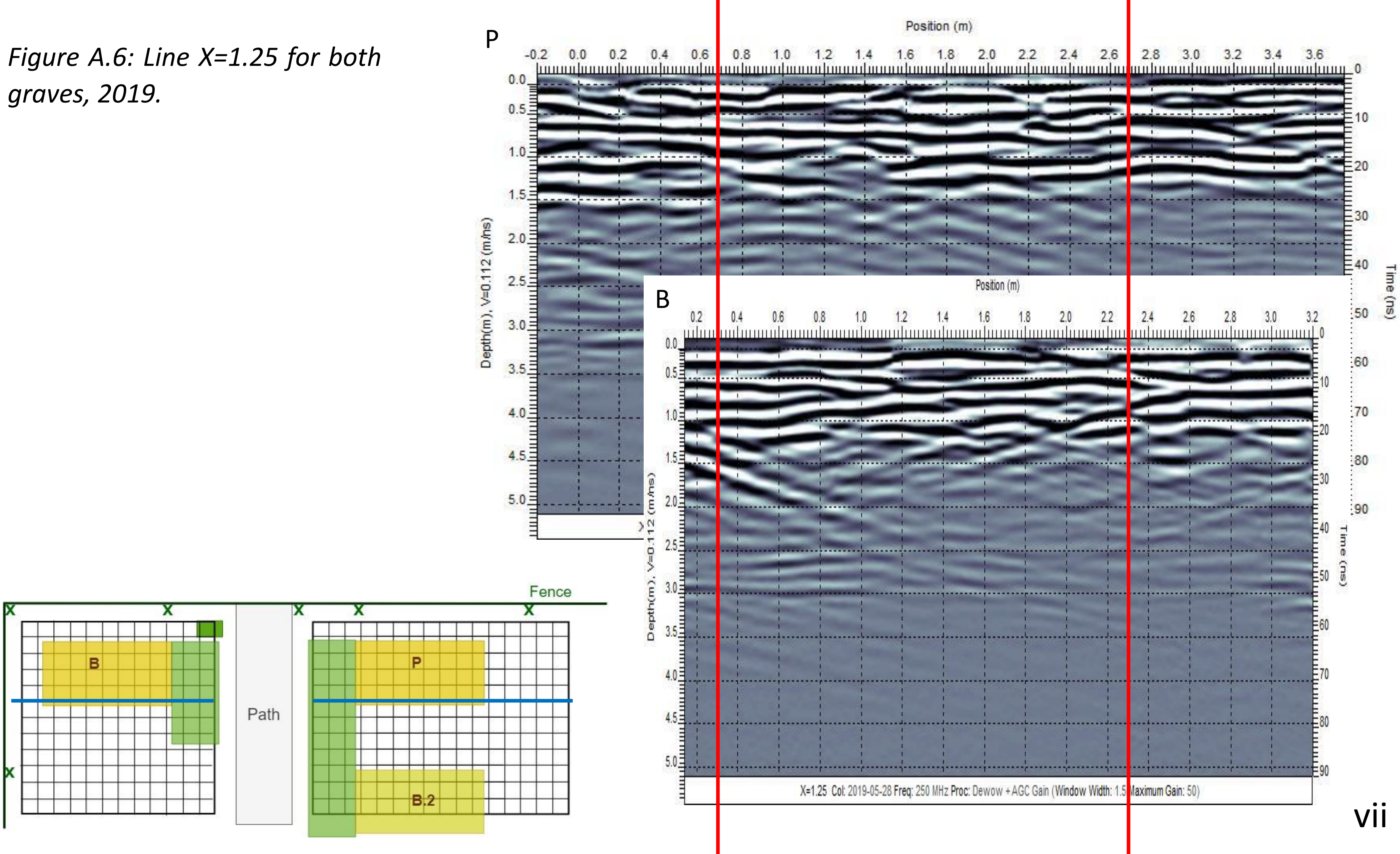

X=1.25 Col: 2019-05-28 Freq: 250 MHz Proc: Dewow + AGC Gain (Window Width: 1.5 Maximum Gain: 50)

Figure A.7: Line X=1.50 for both graves, 2019.

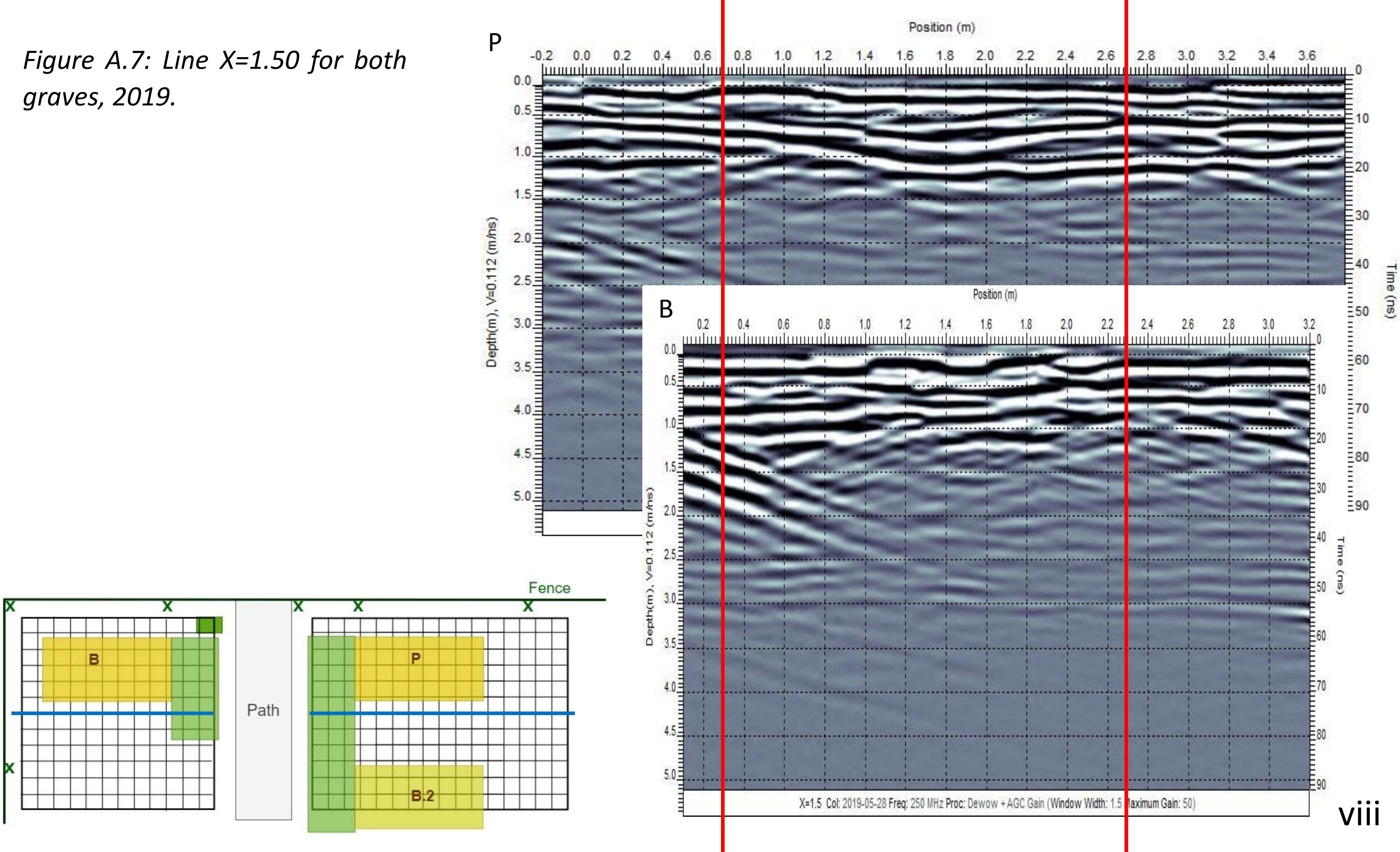

Figure A.8: Line X=1.75 for both graves, 2019.

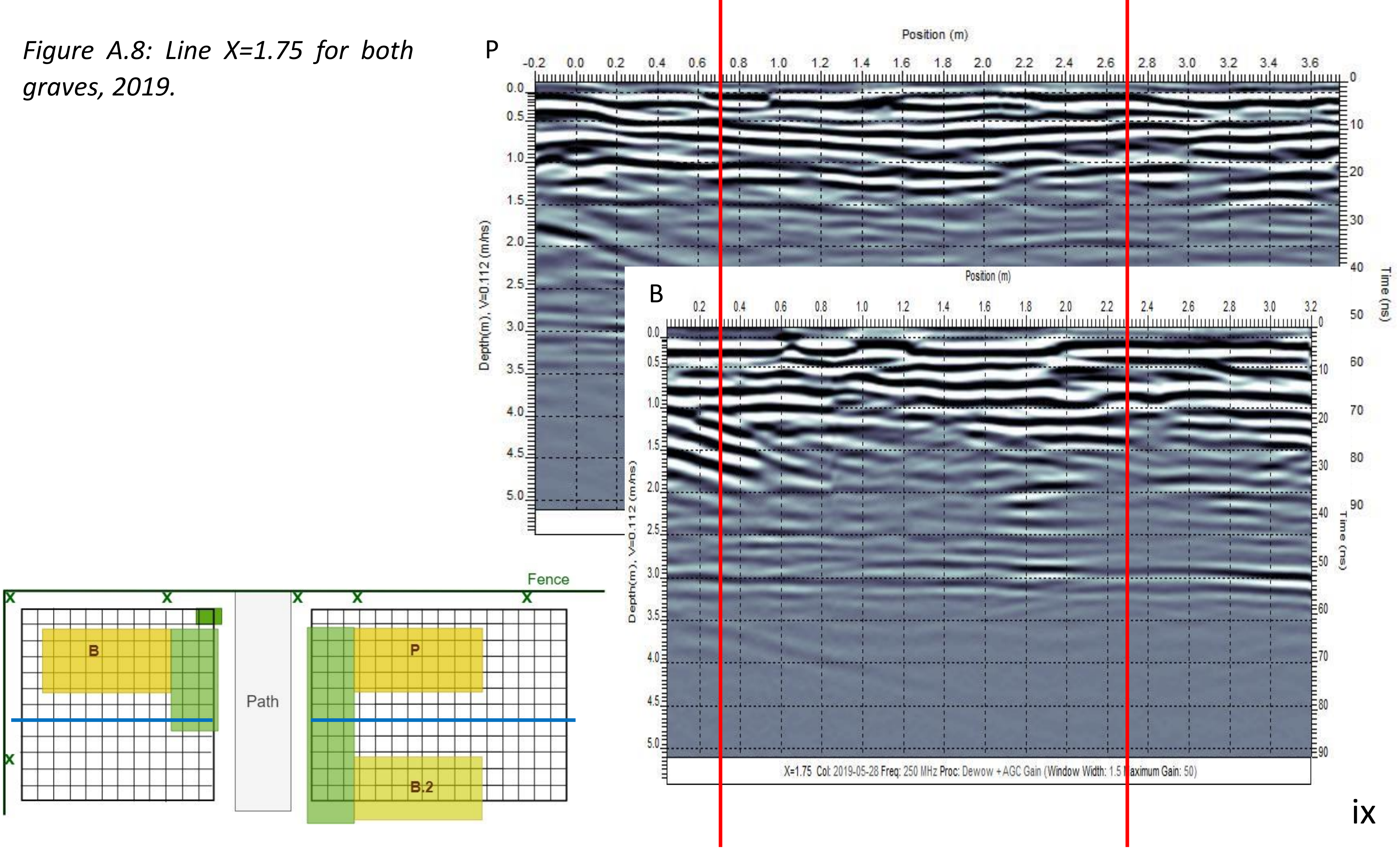

Figure A.9: Line X=2.00 for both graves, 2019.

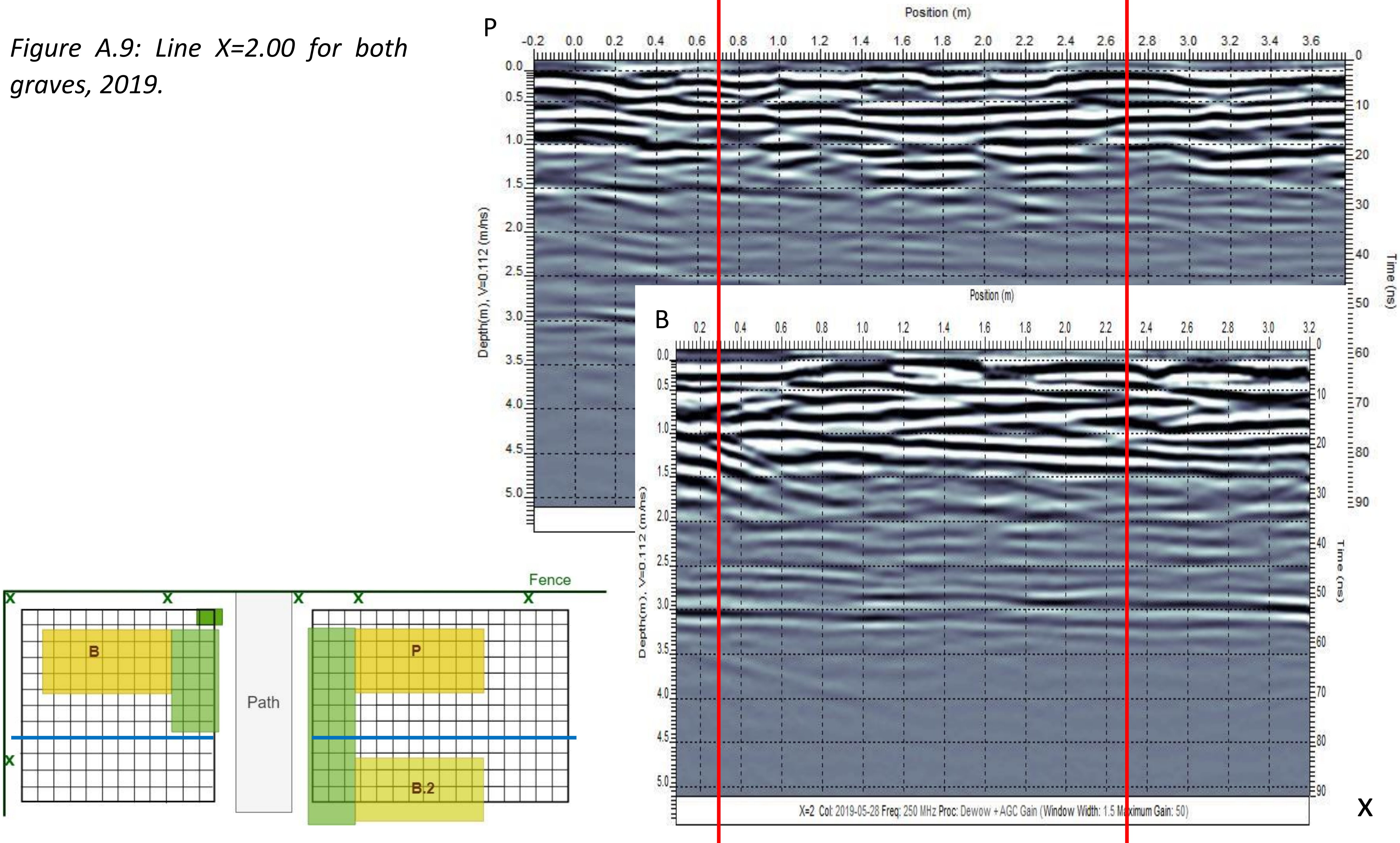

Figure A.10: Line X=2.25 for both graves, 2019.

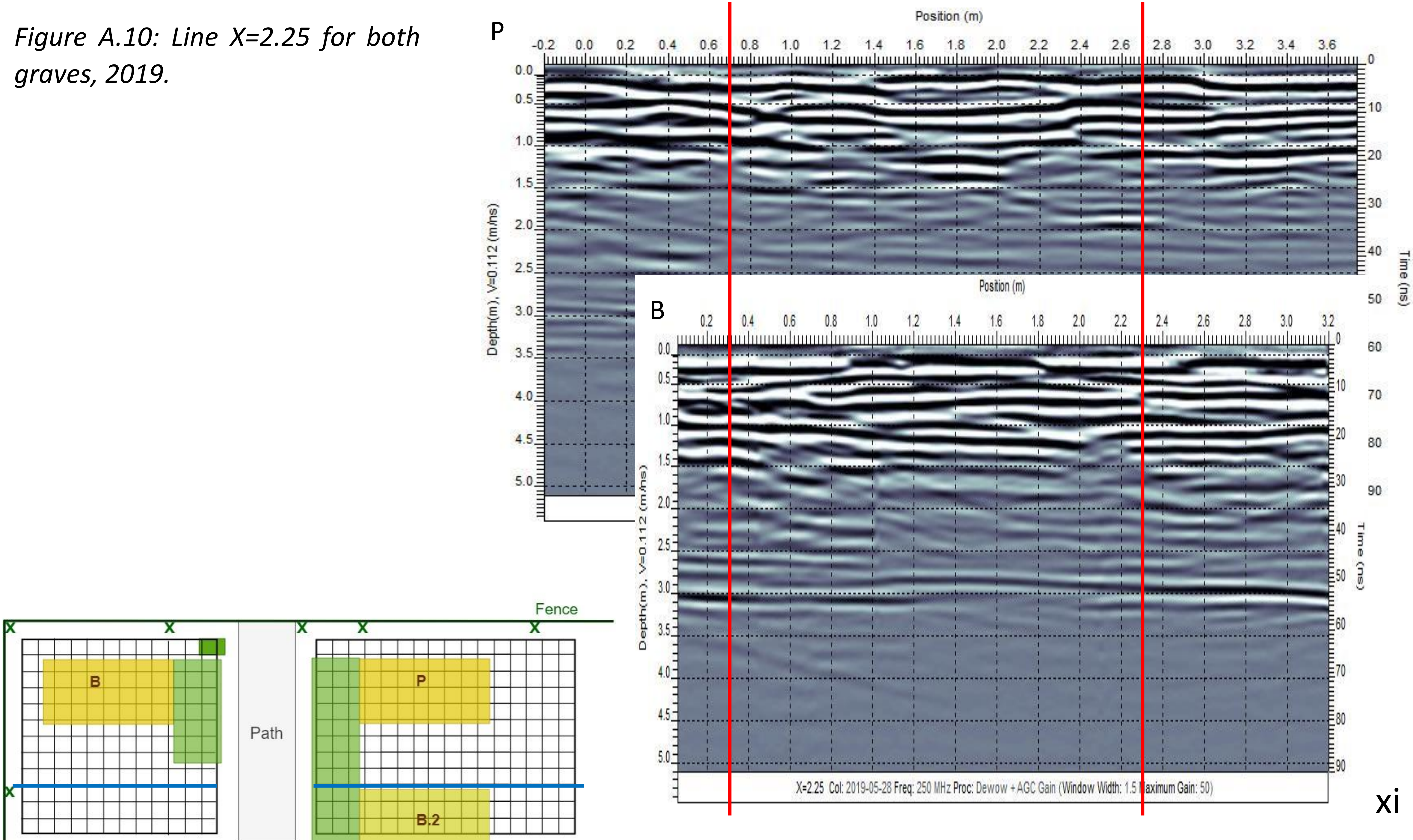

Figure A.11: Line X=2.50 for both graves, 2019.

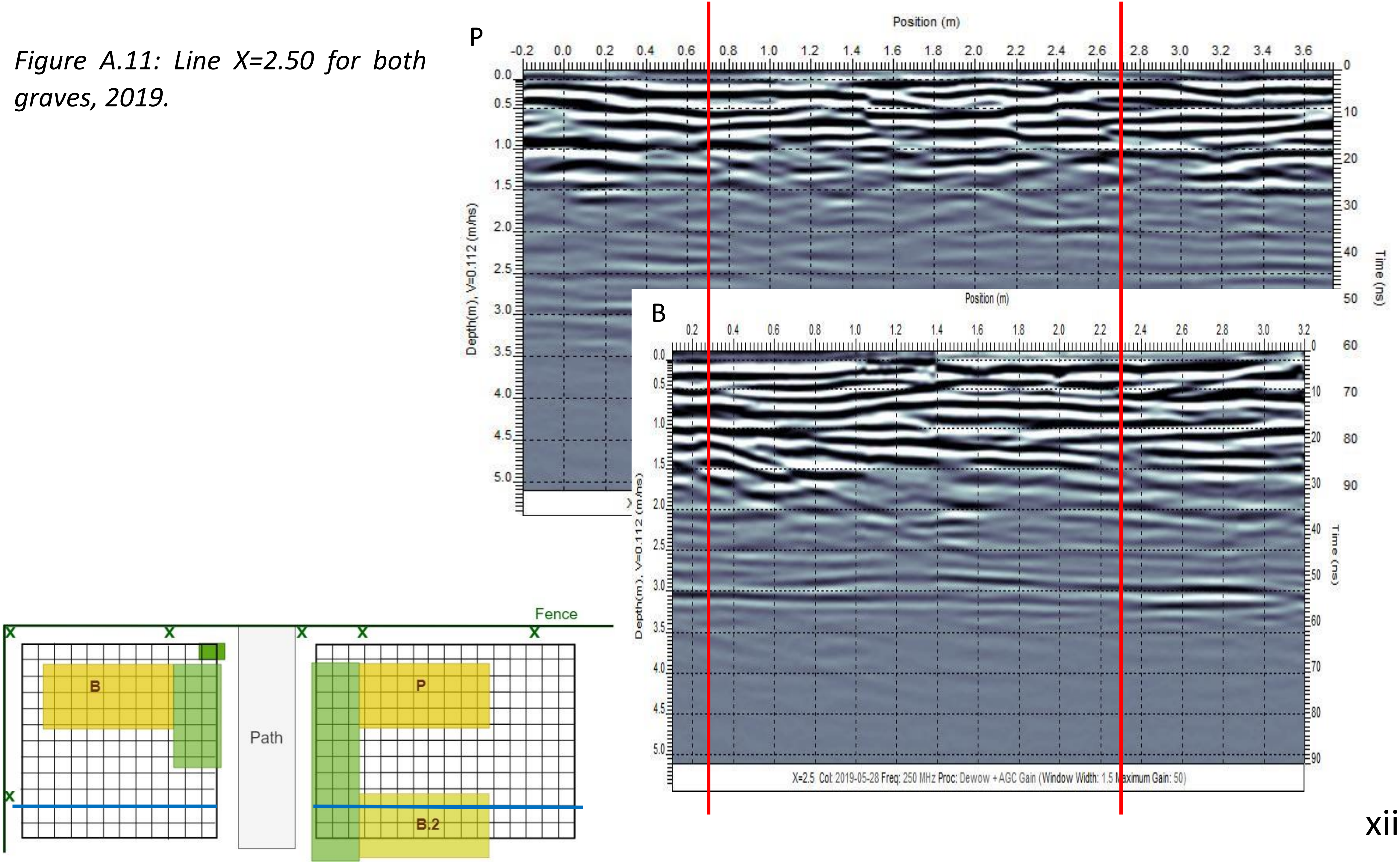

Figure A.12: Line X=2.75 for both graves, 2019.

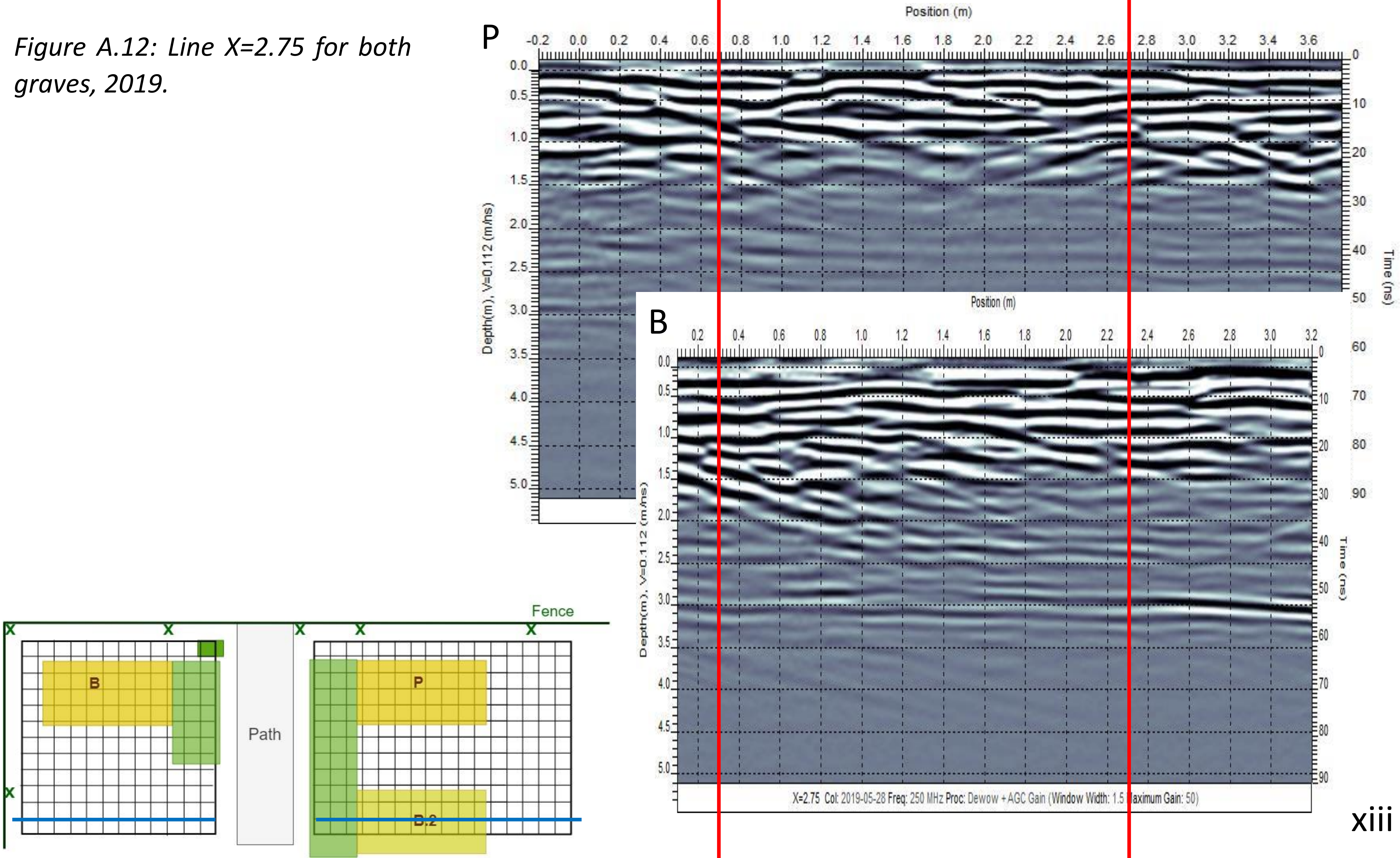

Figure A.13: Line X=3.00 for both graves, 2019.

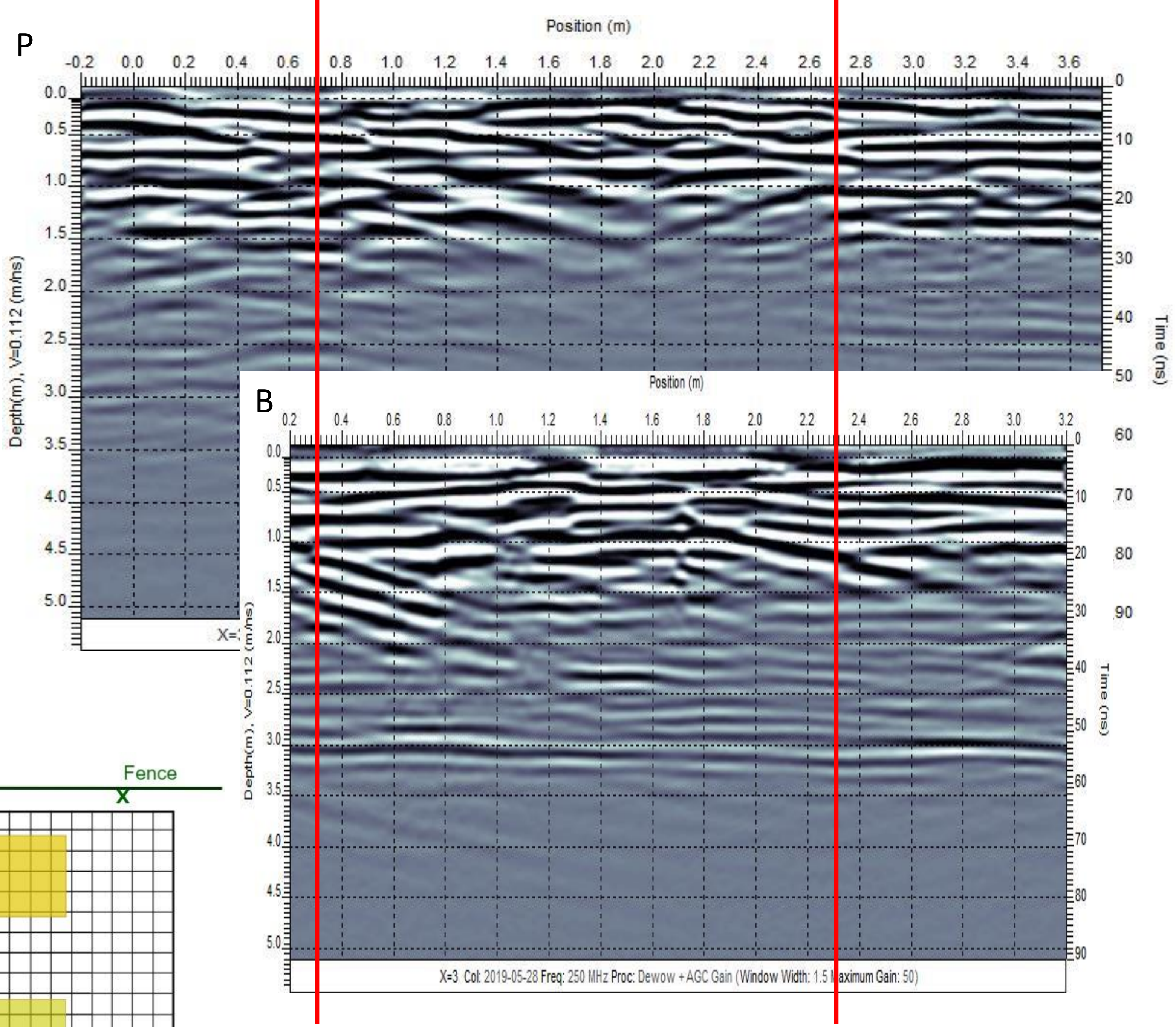

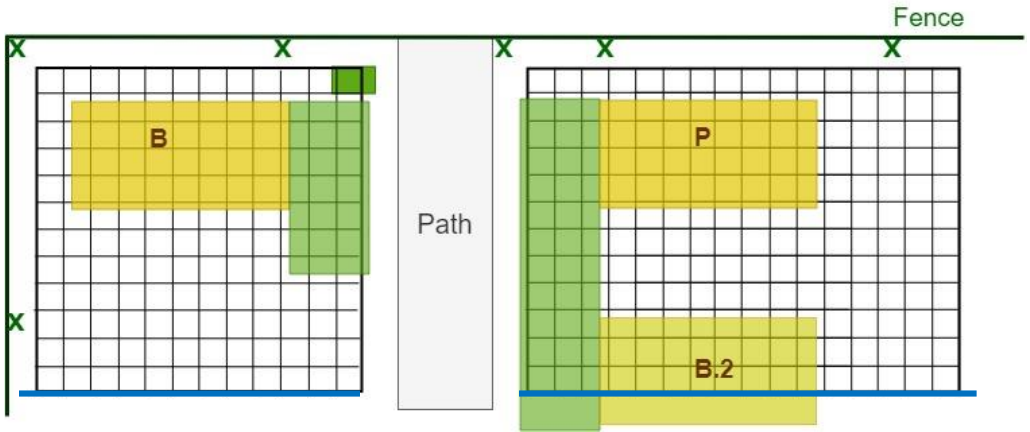

Figure A.14: Line Y=0.00 (B) and Y=3.00 (P) , 2019.

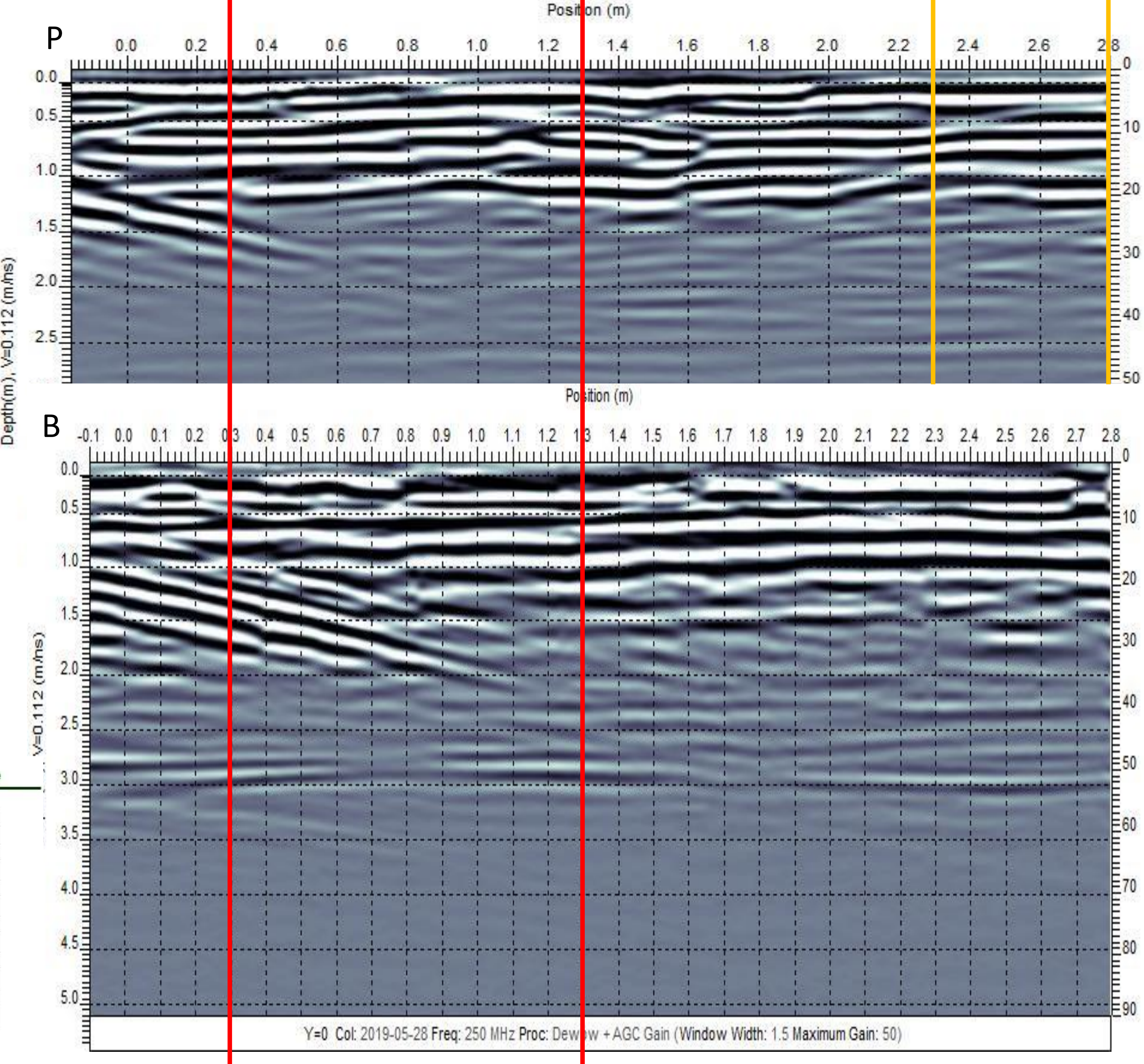

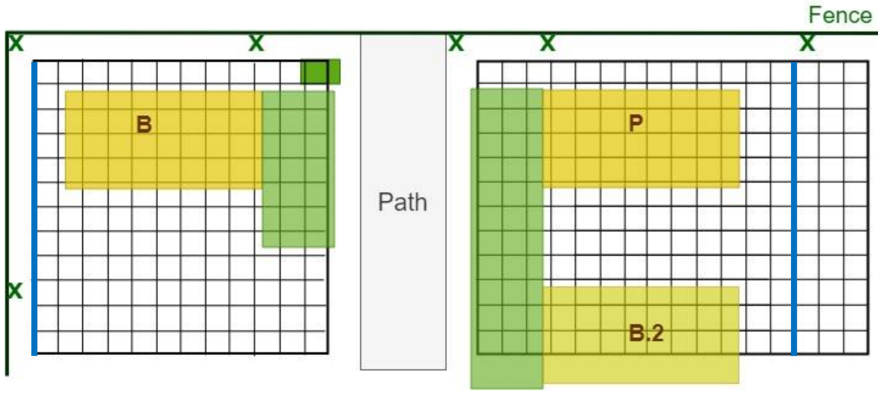

XV

Figure A.15: Line Y=0.25 (B) and Y=2.75 (P) , 2019.

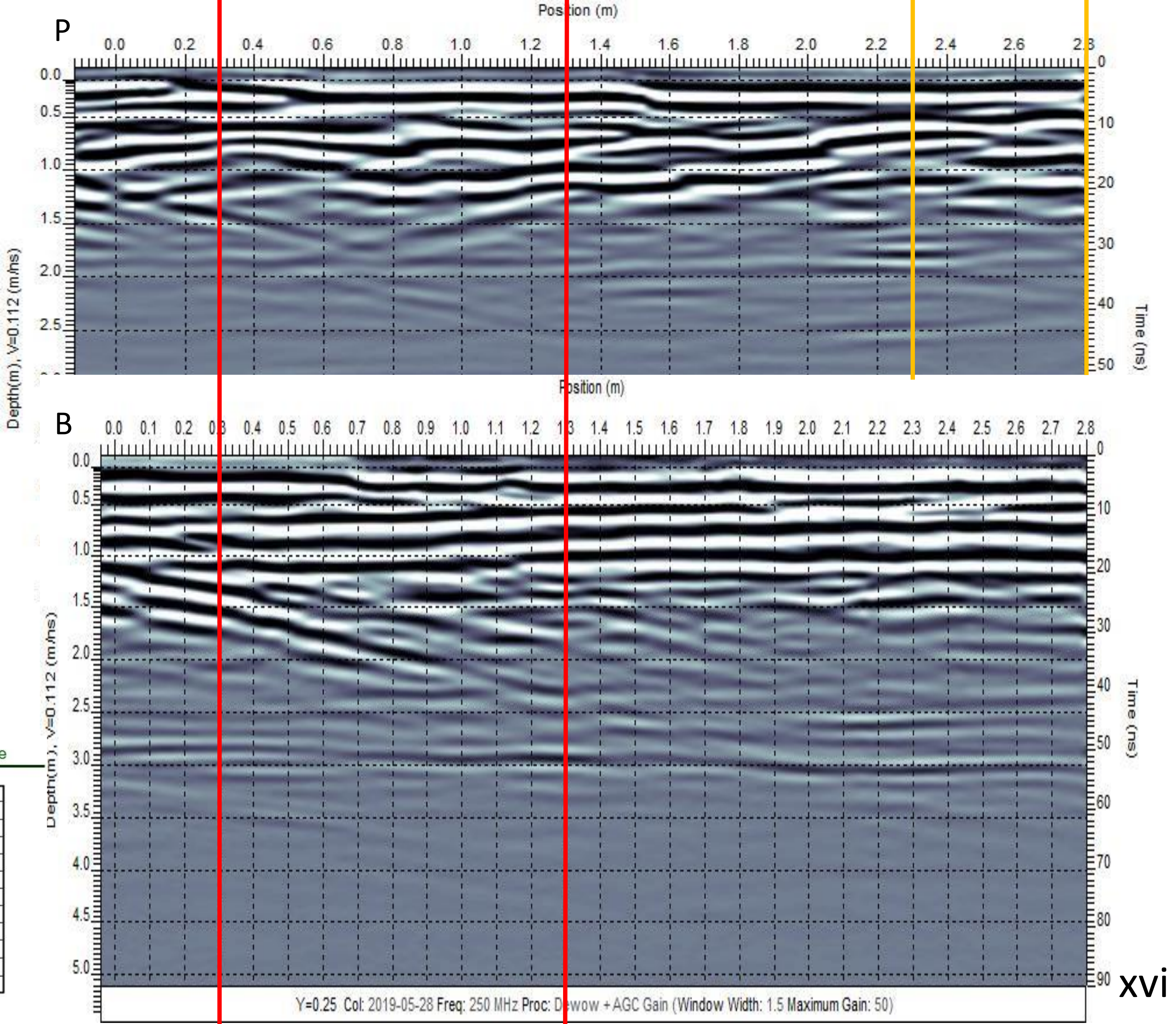

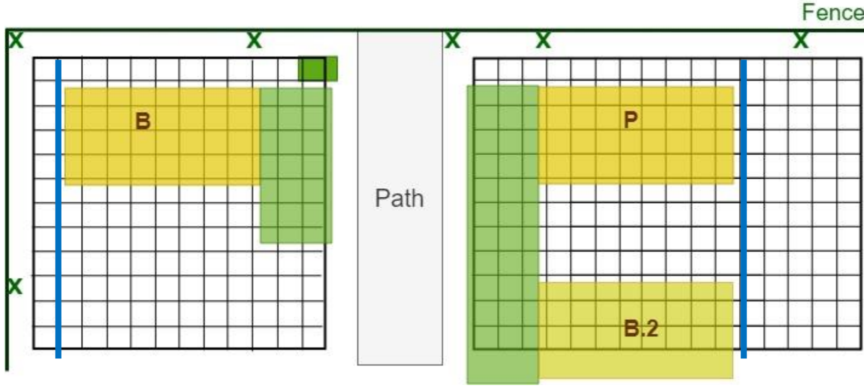

Figure A.16: Line Y=0.50 (B) and Y=2.50 (P) , 2019.

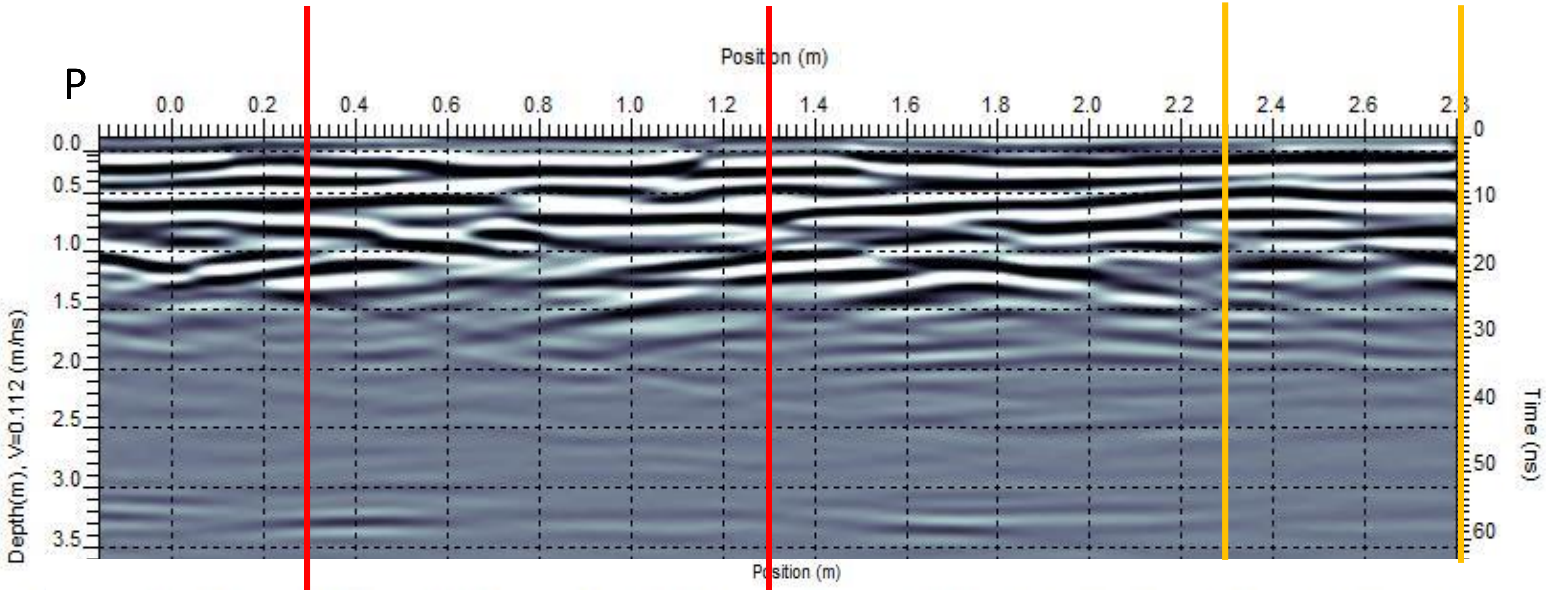

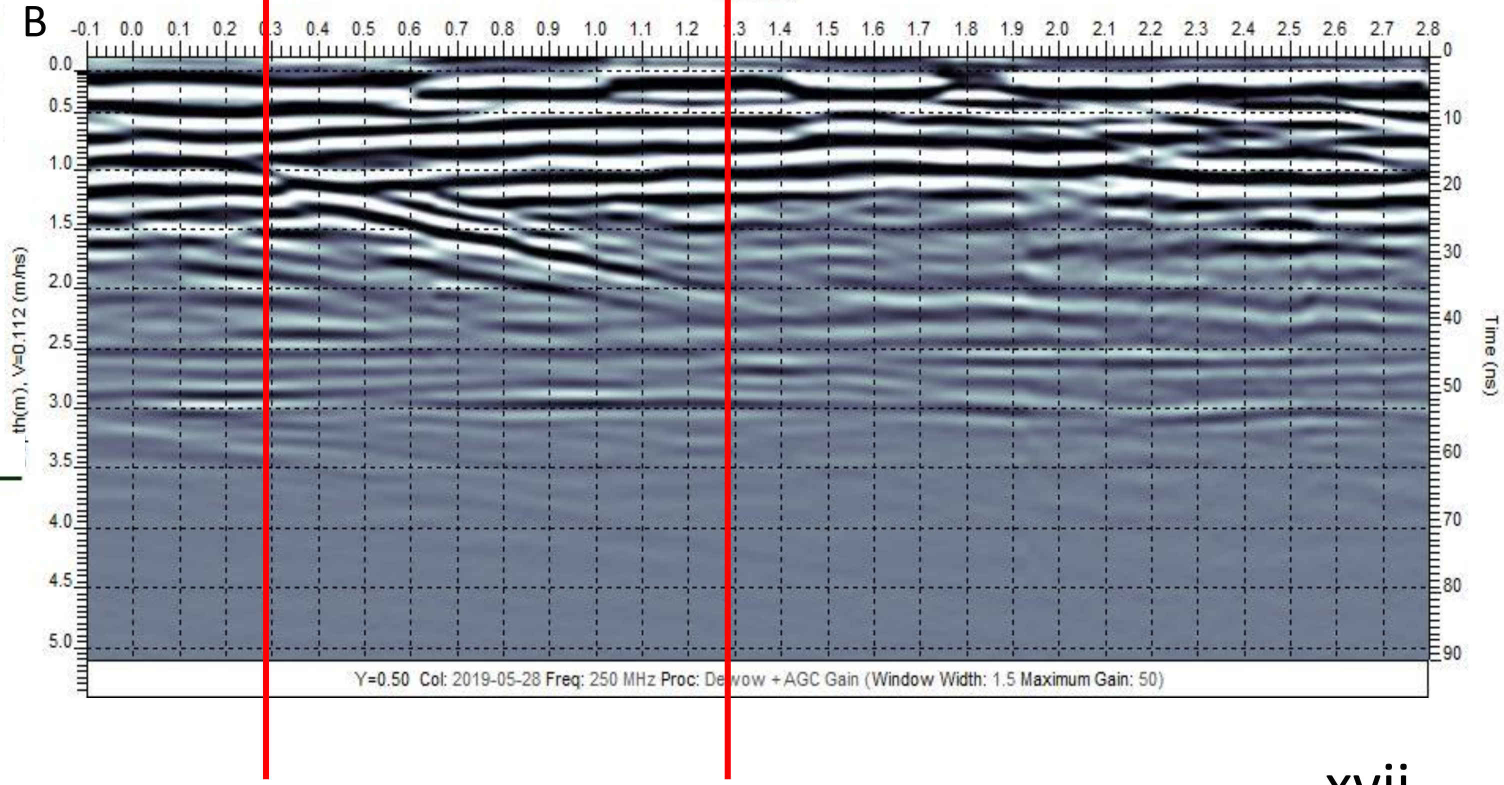

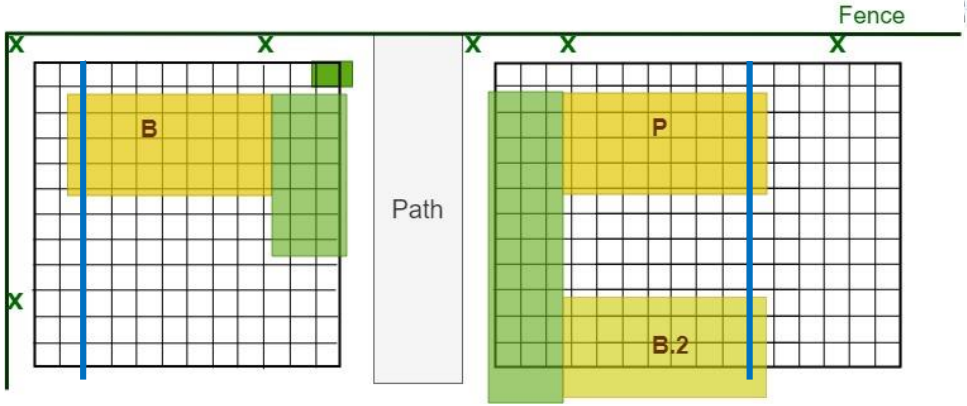

Figure A.17: Line Y=0.75 (B) and Y=2.25 (P) , 2019.

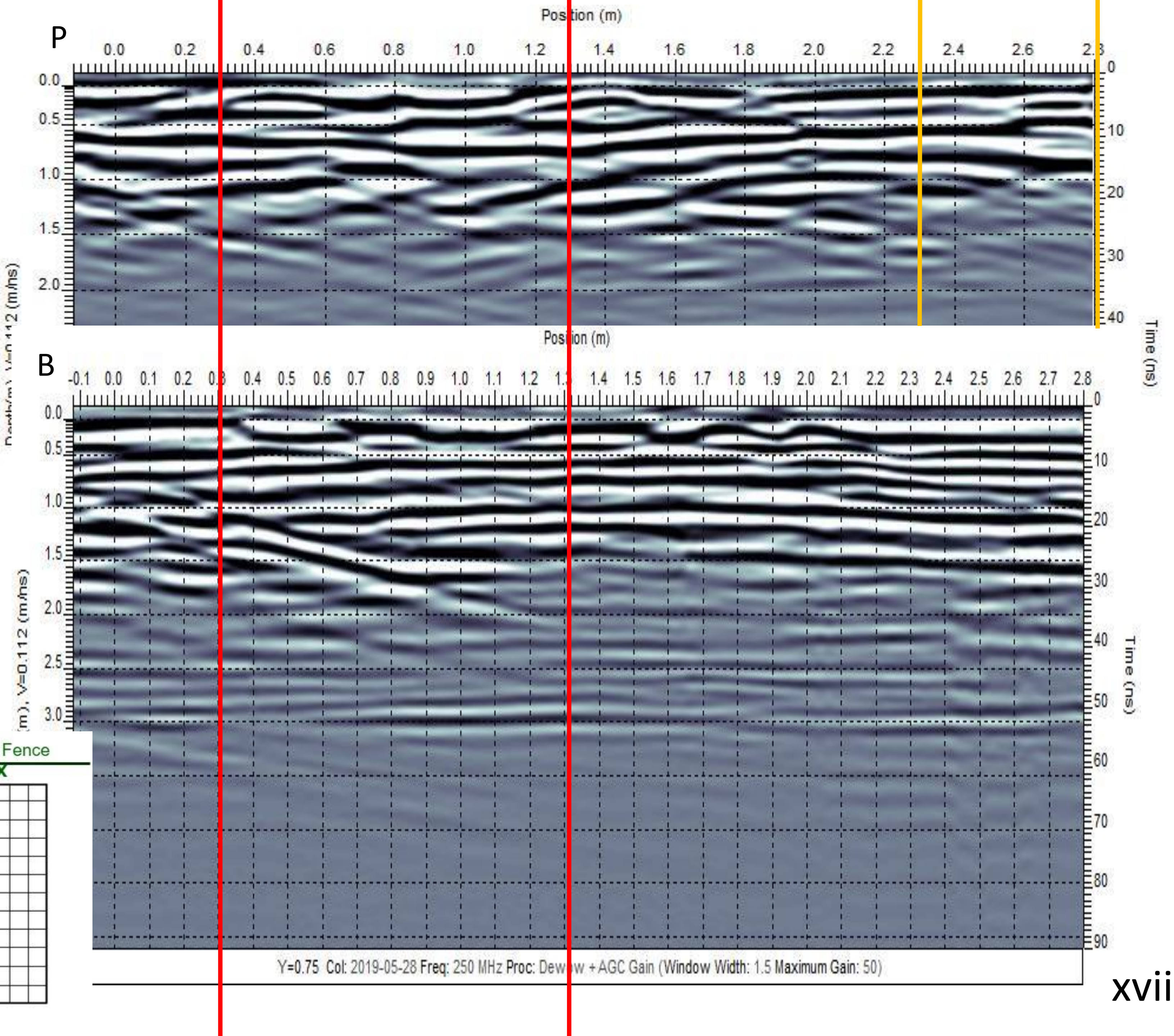

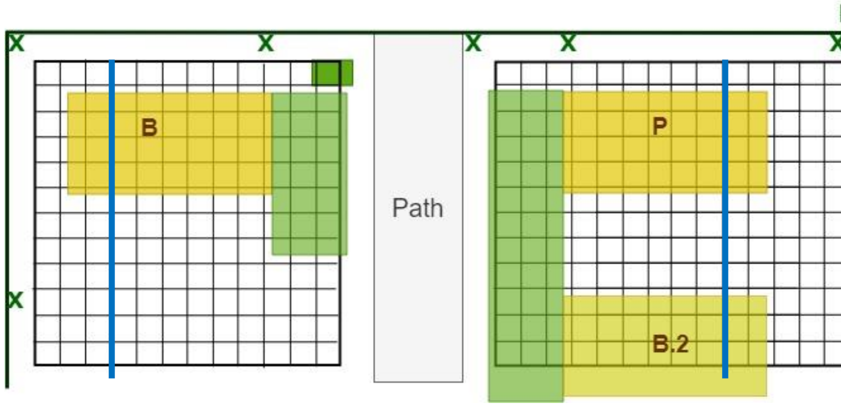

Figure A.18: Line Y=1.00 (B) and Y=2.00 (P) , 2019.

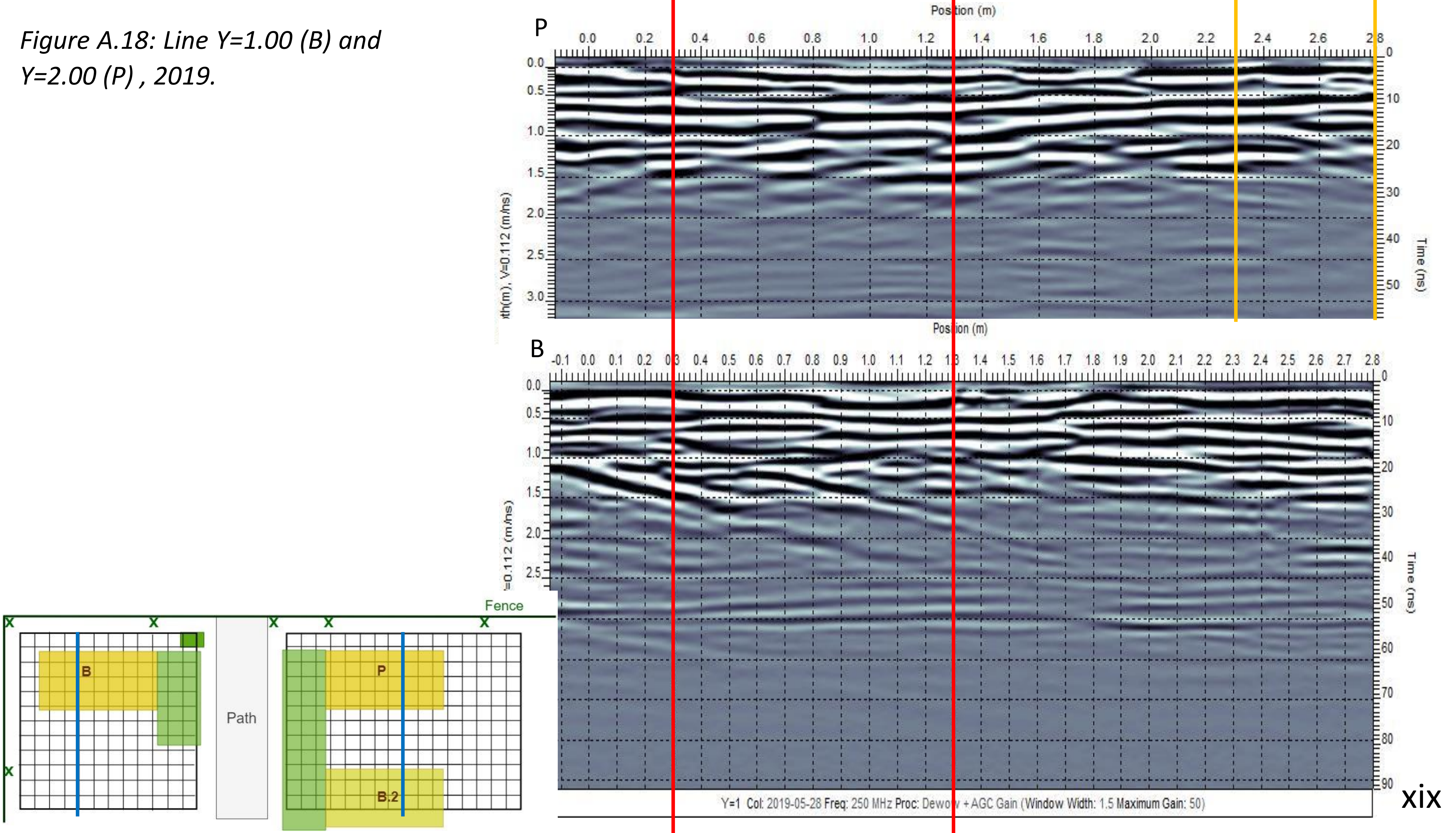

Figure A.19: Line Y=1.25 (B) and Y=1.75 (P) , 2019.

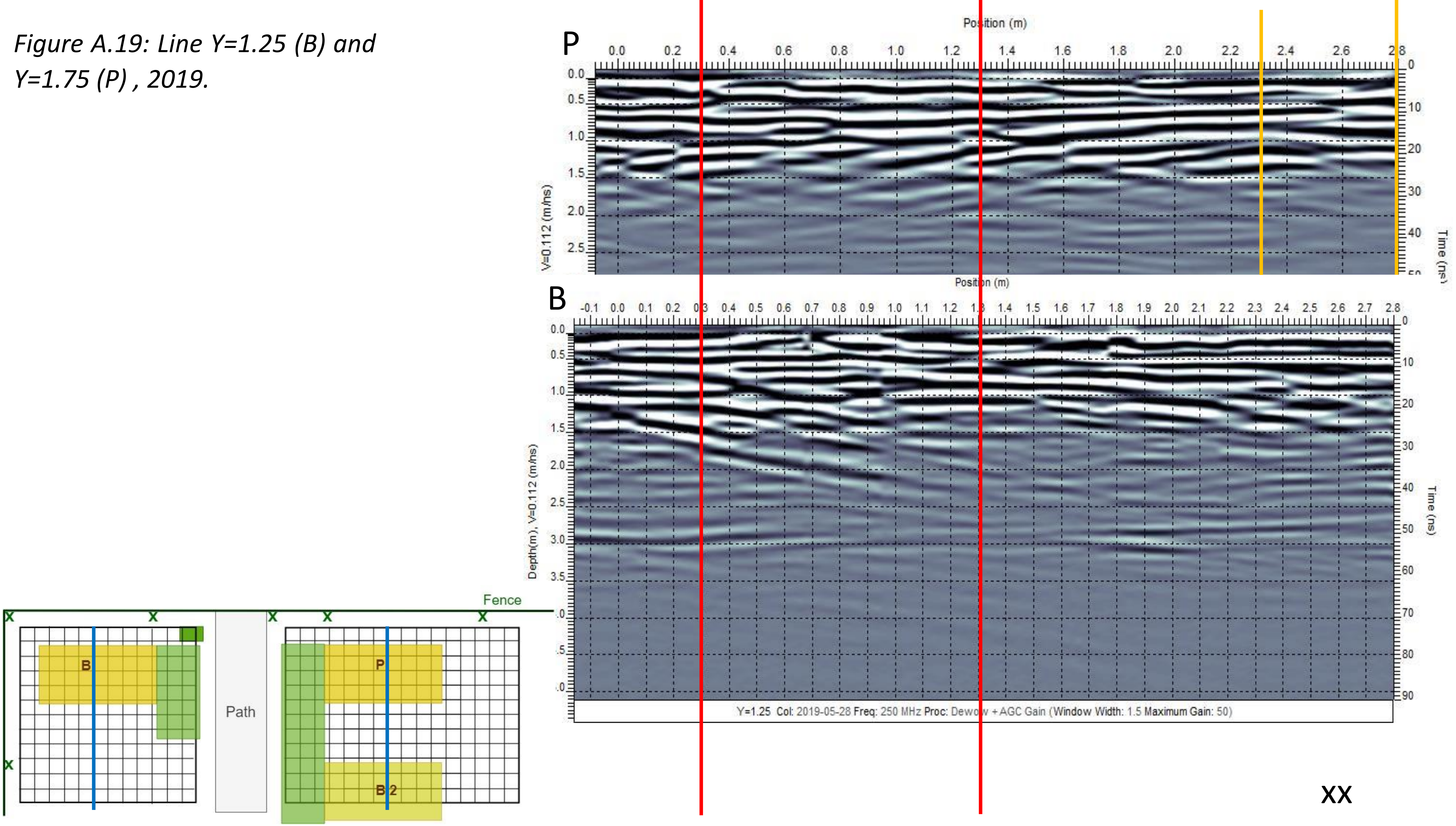

Figure A.20: Line Y=1.50 (B) and Y=1.50 (P) , 2019.

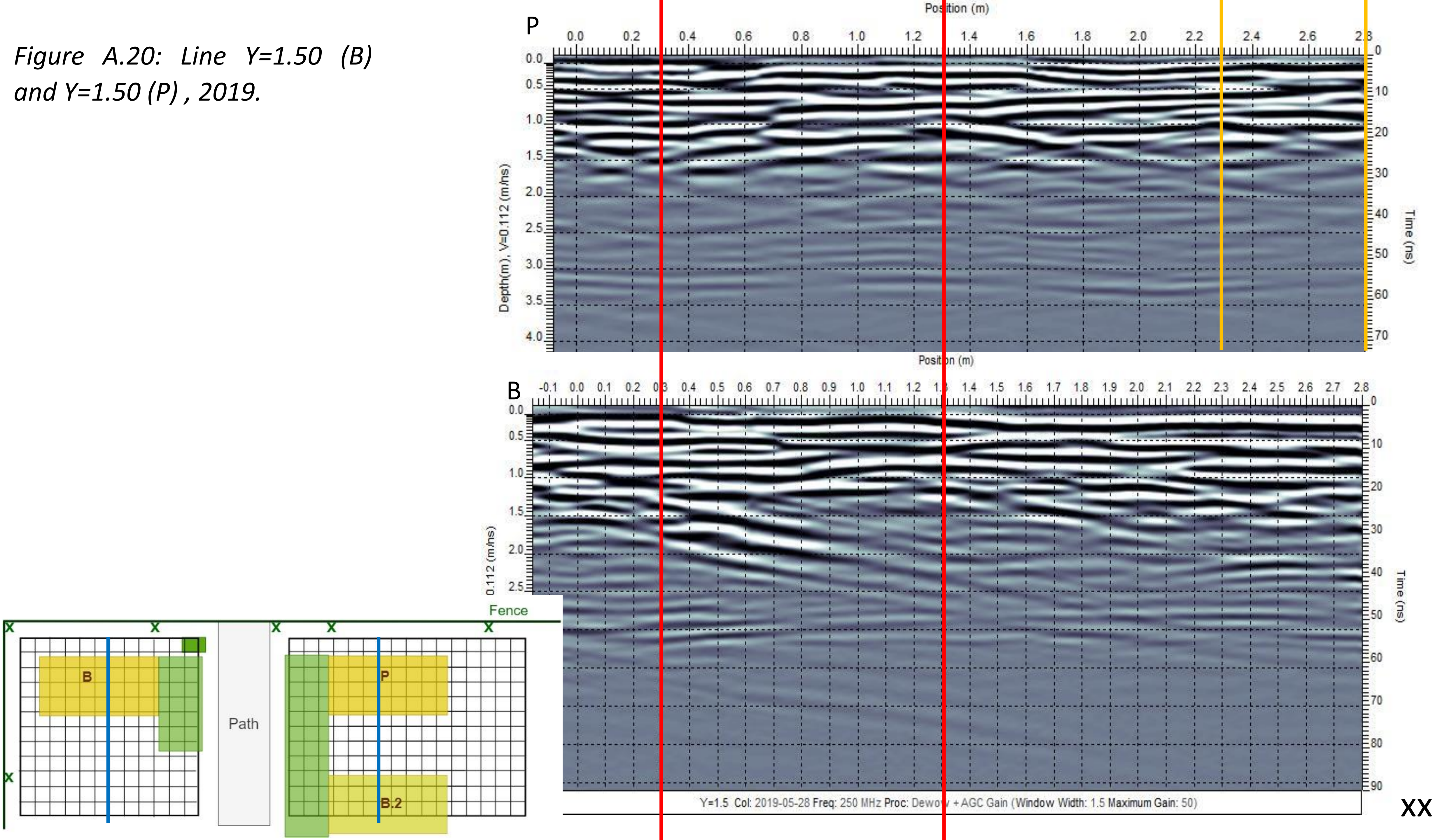

Figure A.21: Line Y=1.75 (B) and Y=1.25 (P) , 2019.

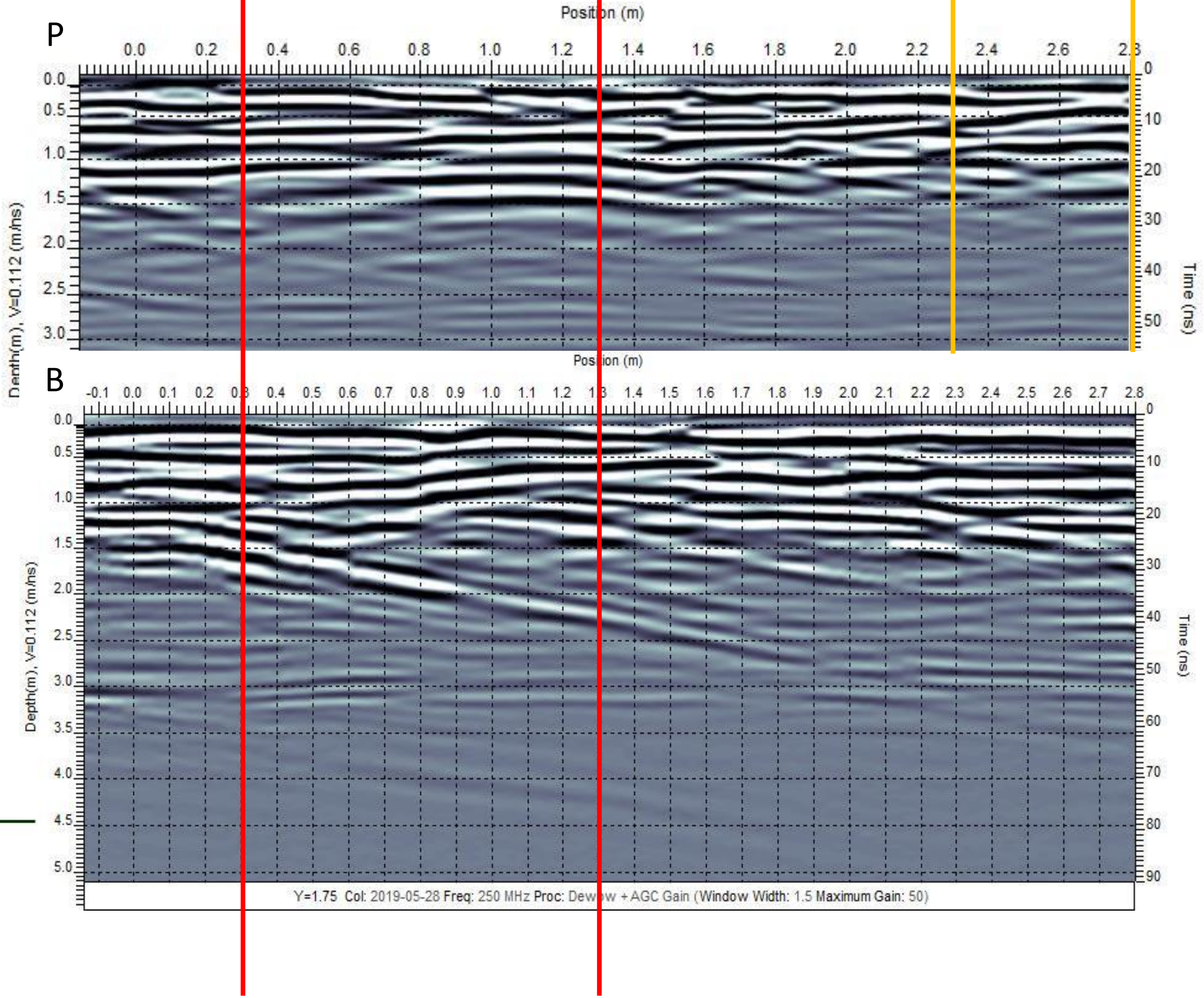

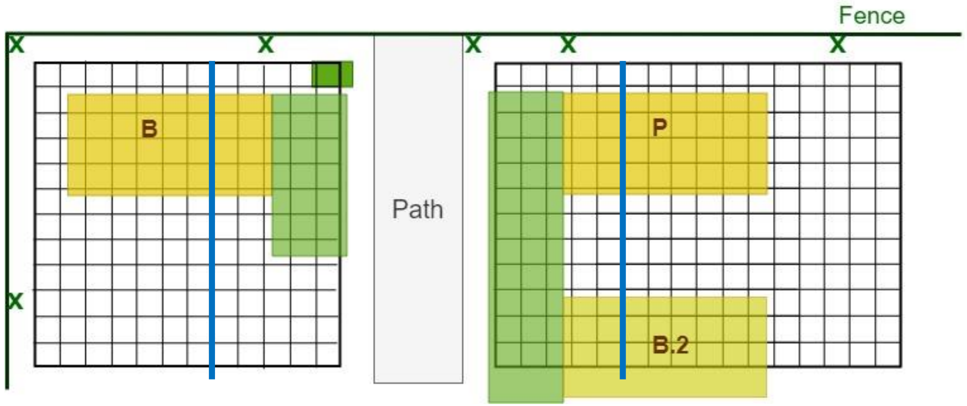

Figure A.22: Line Y=2.00 (B) and Y=1.00 (P) , 2019.

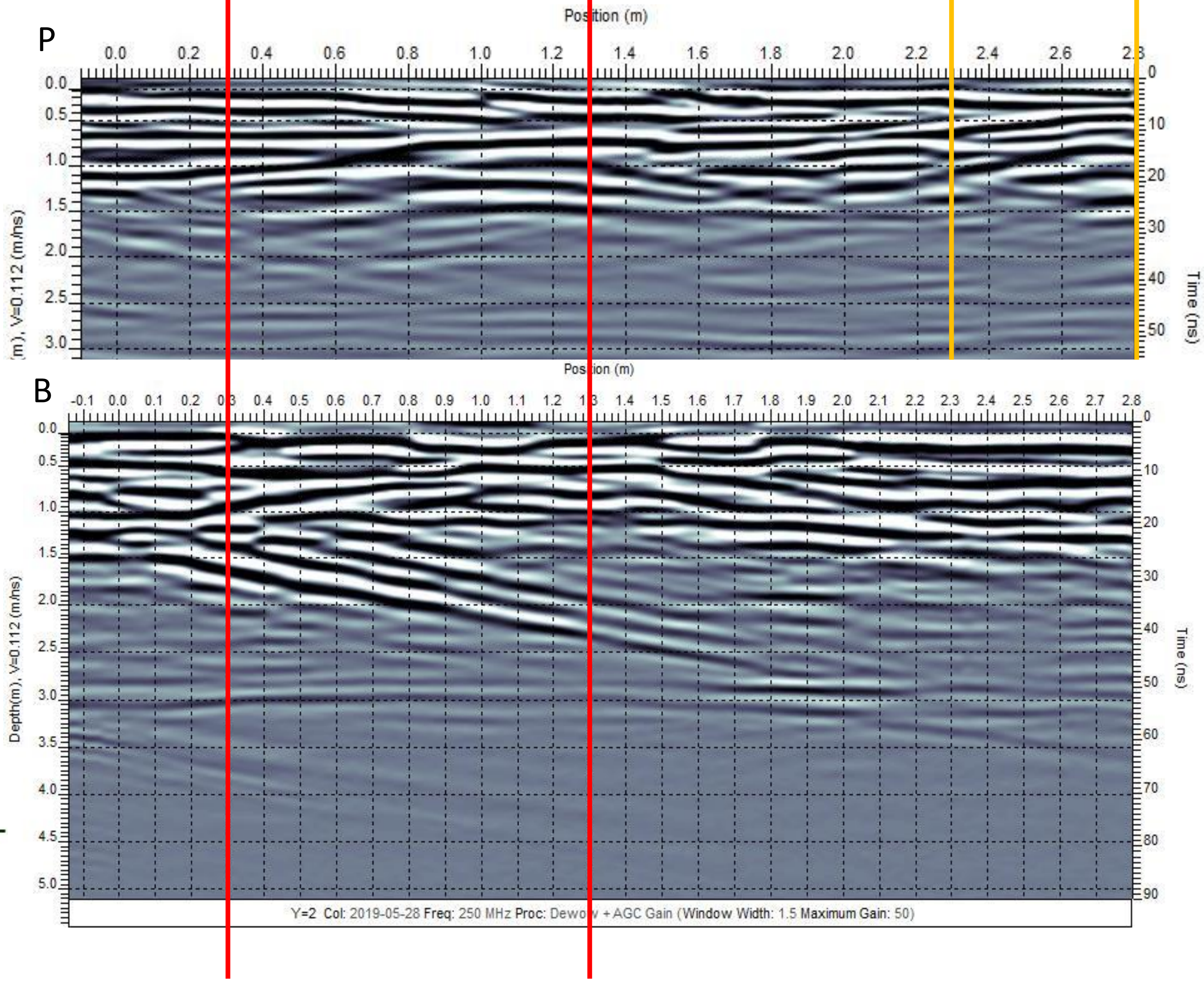

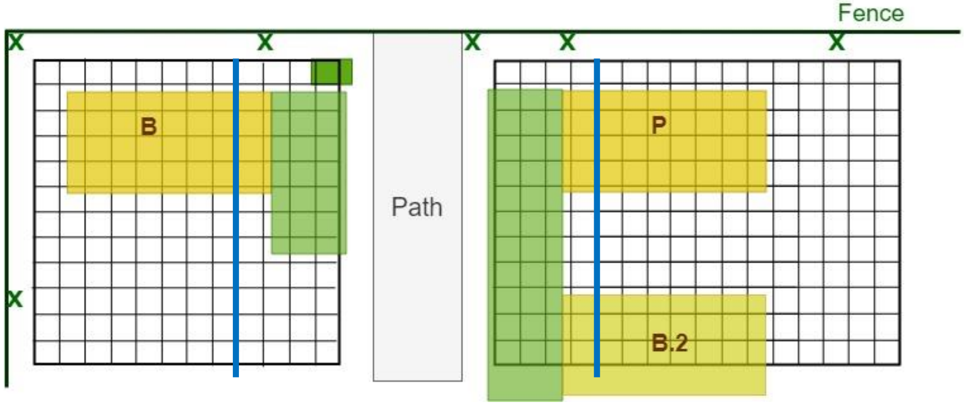

Figure A.23: Line Y=2.25 (B) and Y=0.75 (P) , 2019.

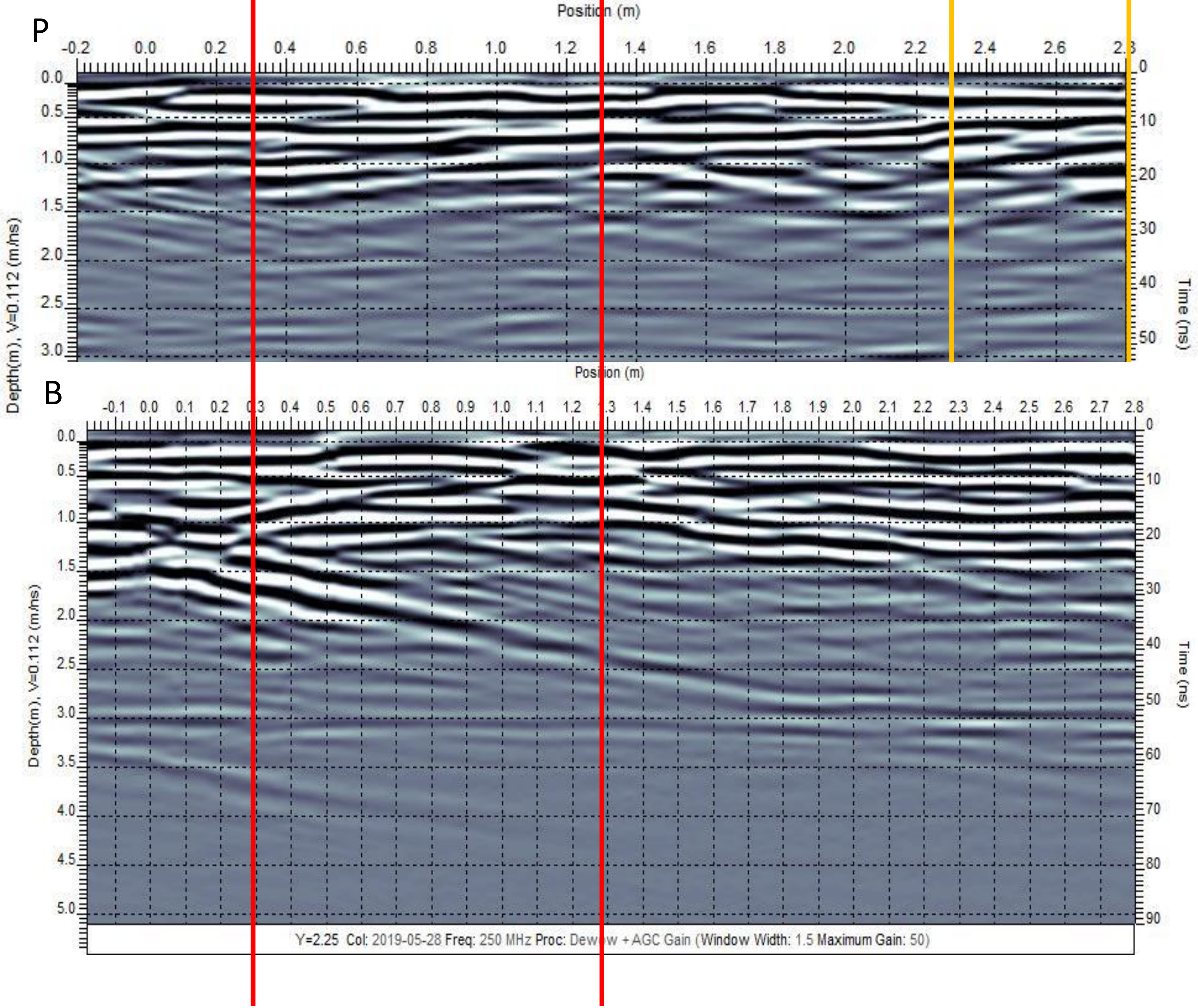

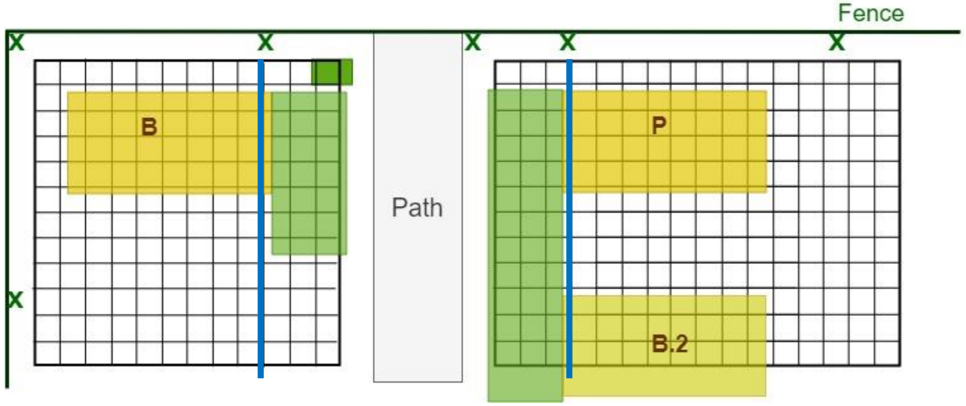

Figure A.24: Line Y=2.50 (B) and Y=0.50 (P) , 2019.

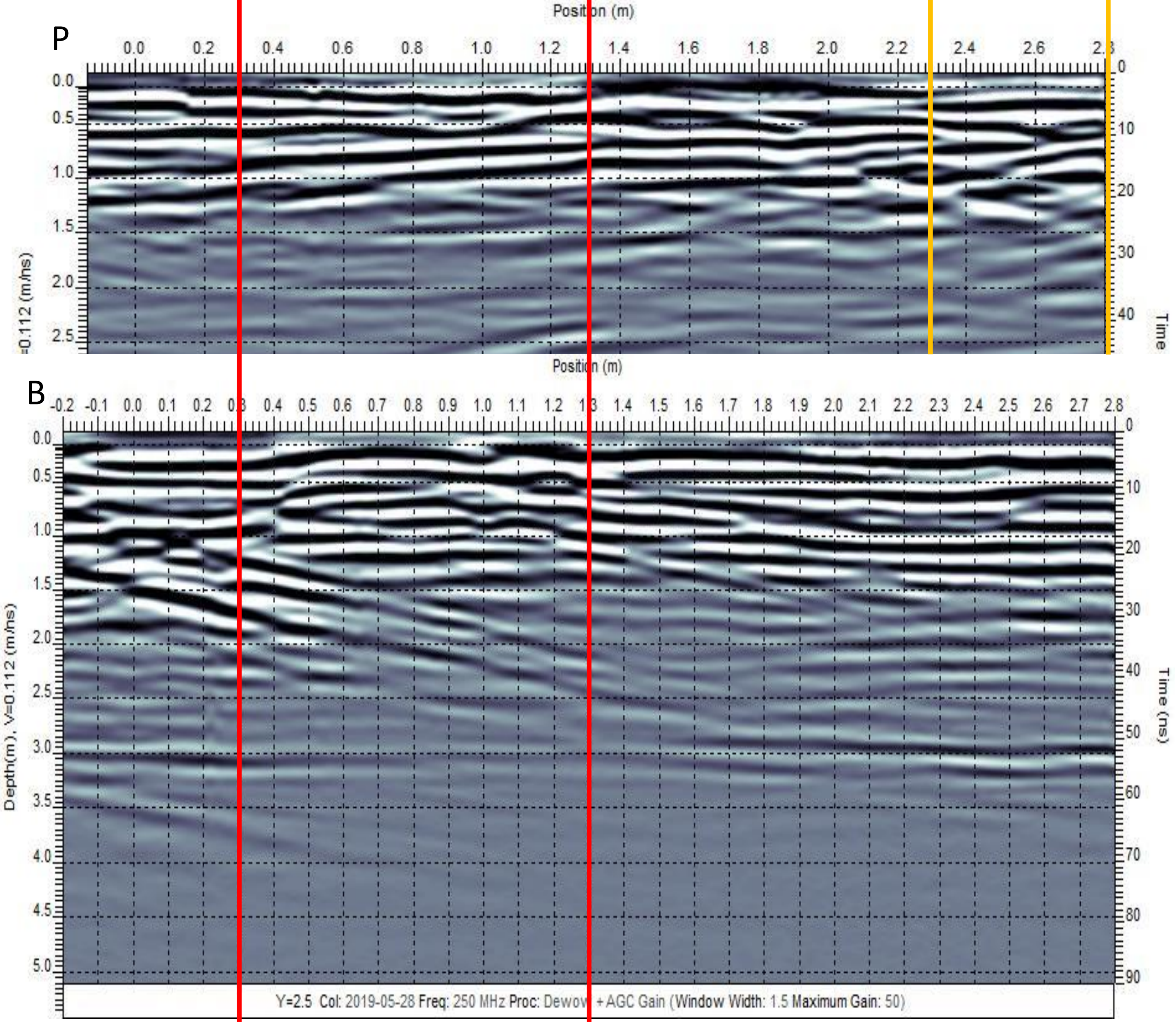

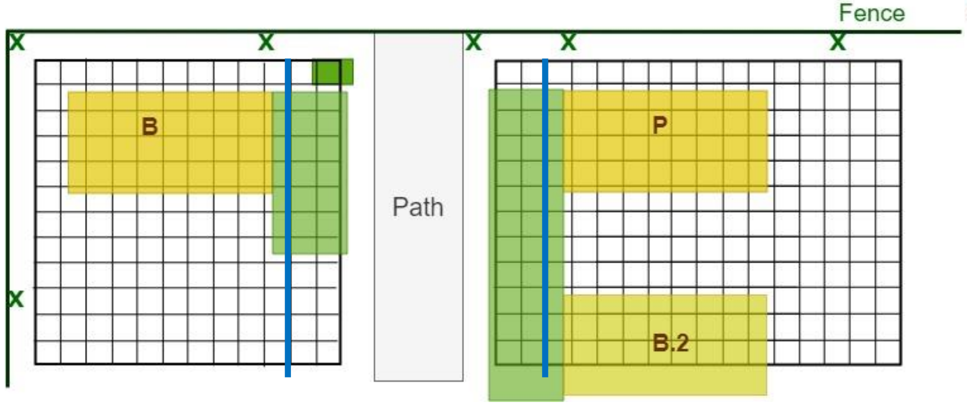

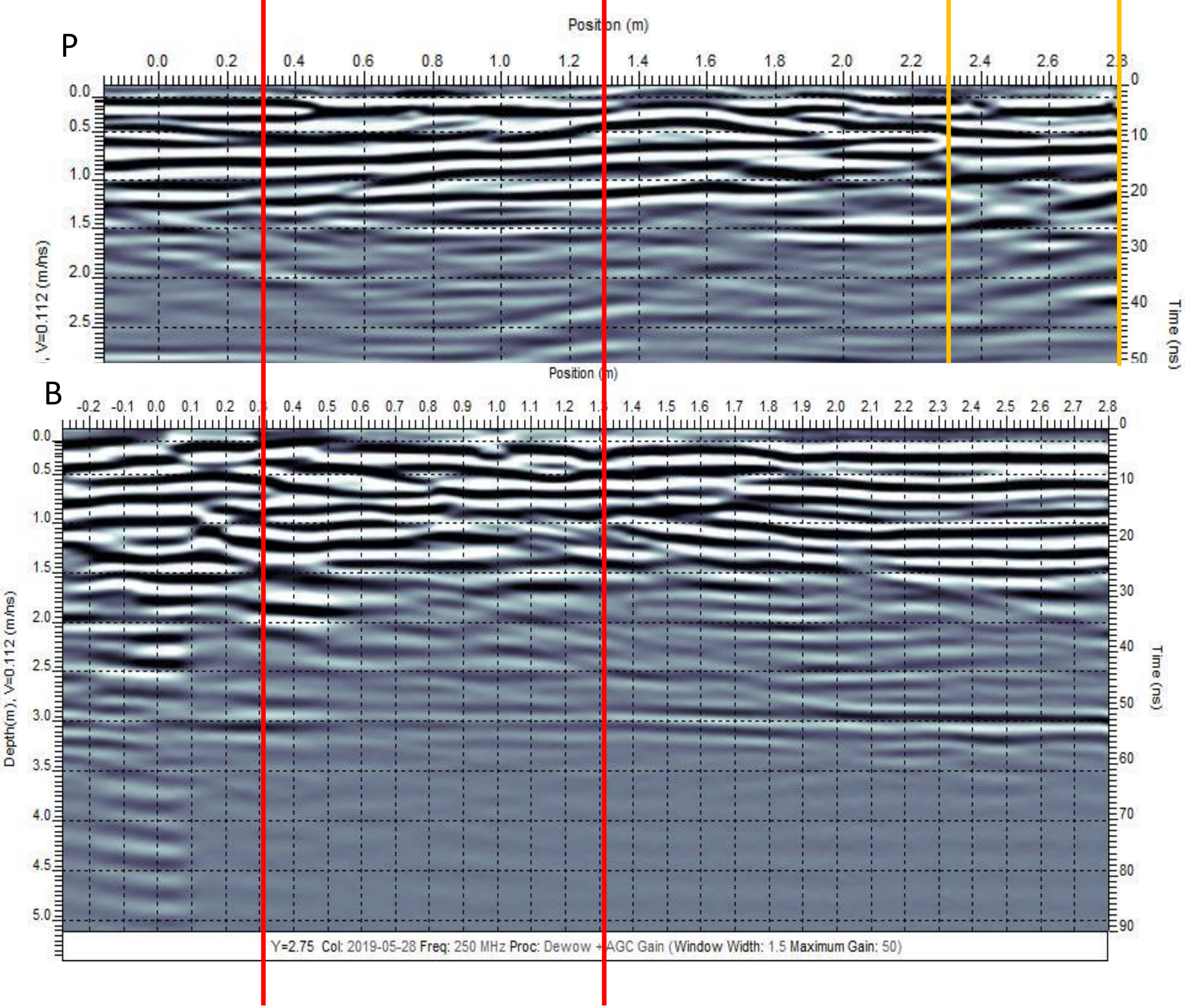

Figure A.25: Line Y=2.75 (B) and Y=0.25 (P) , 2019.

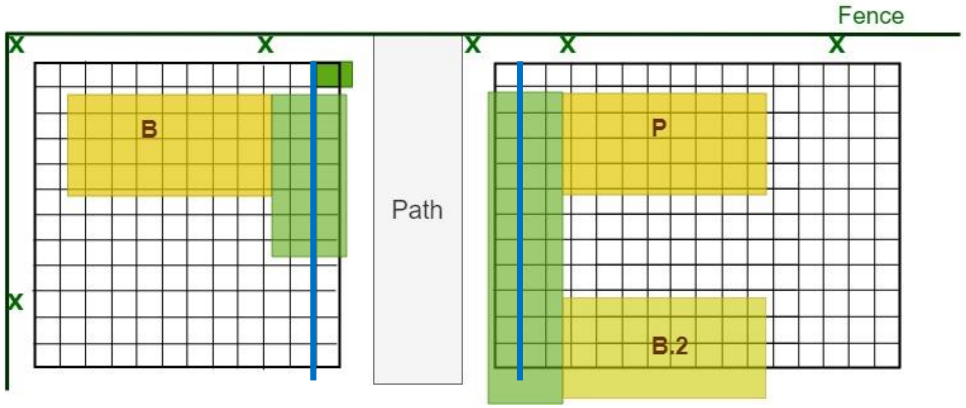

Figure A.26: Line Y=3.00 (B) and Y=0.00 (P) , 2019.

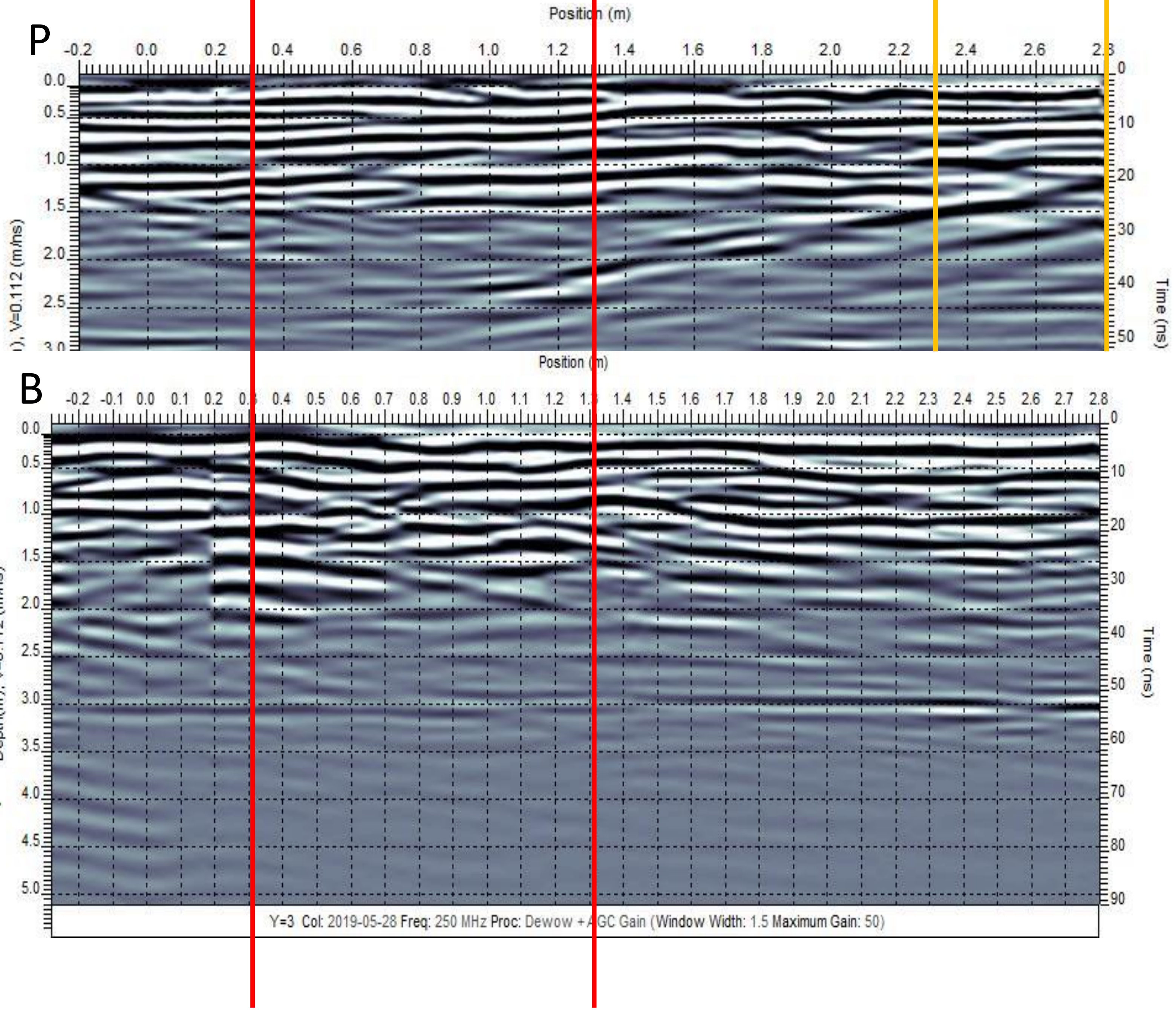

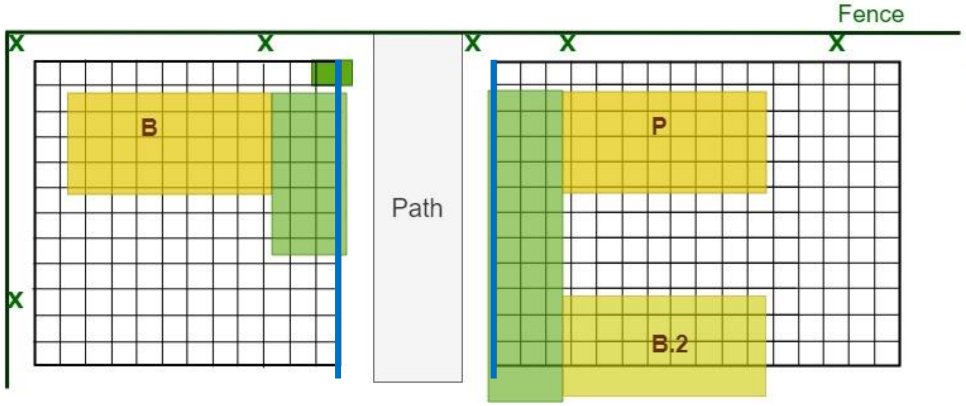

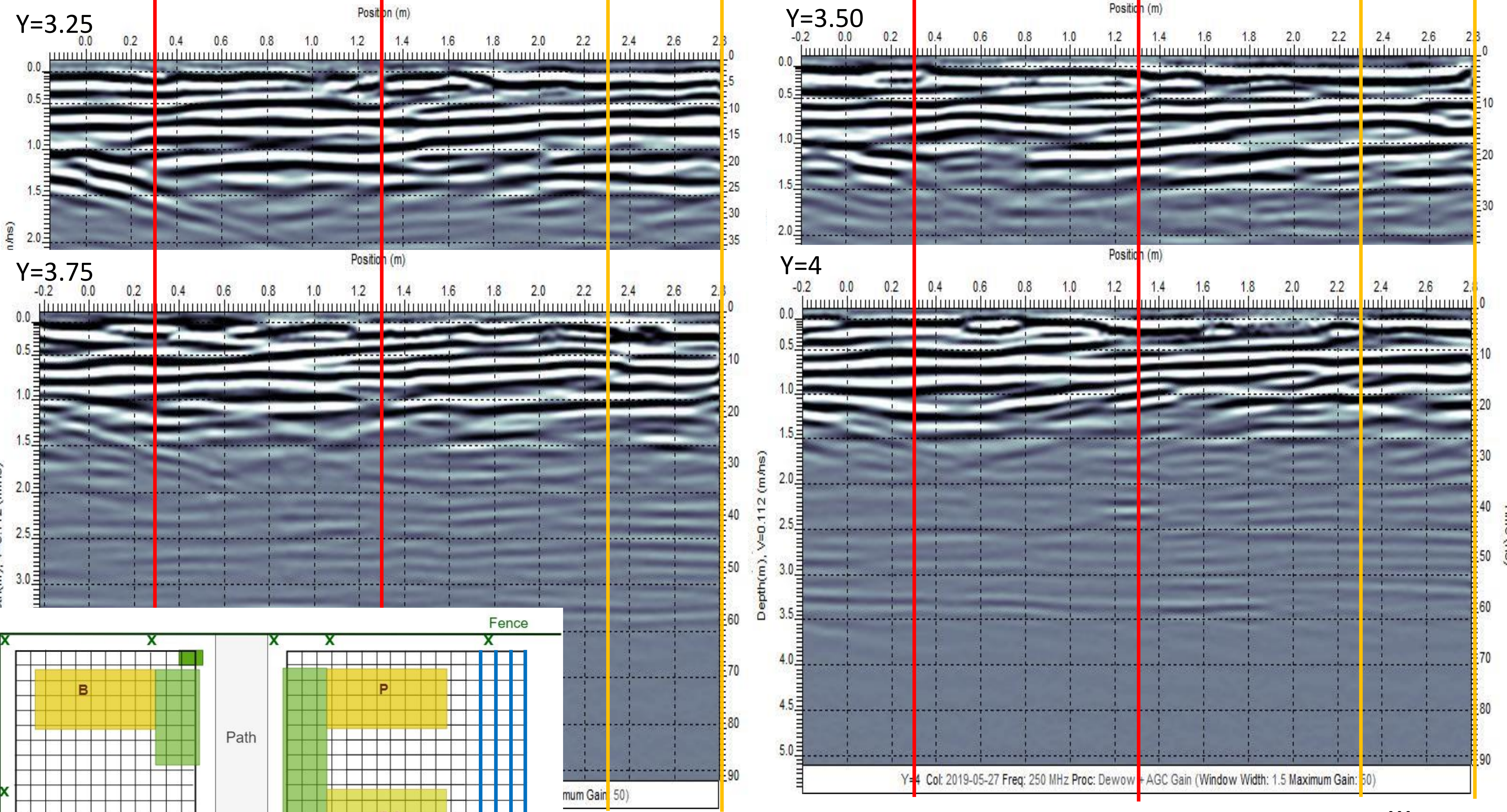

Figure A.27: Line Y=3.25, Y=3.50, Y=3.75 and Y=4.00 (P) , 2019.

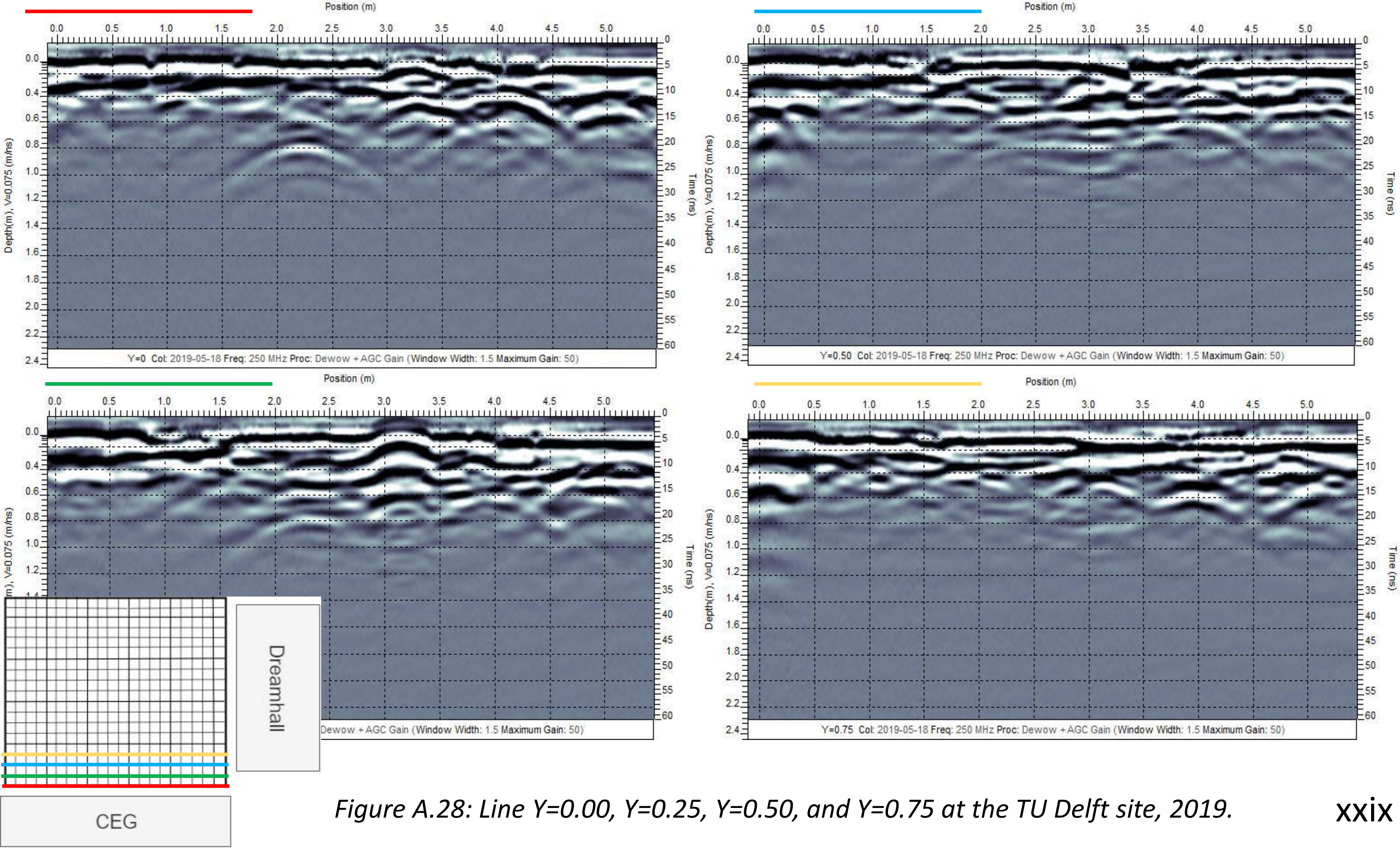

Figure A.28: Line Y=0.00, Y=0.25, Y=0.50, and Y=0.75 at the TU Delft site, 2019.

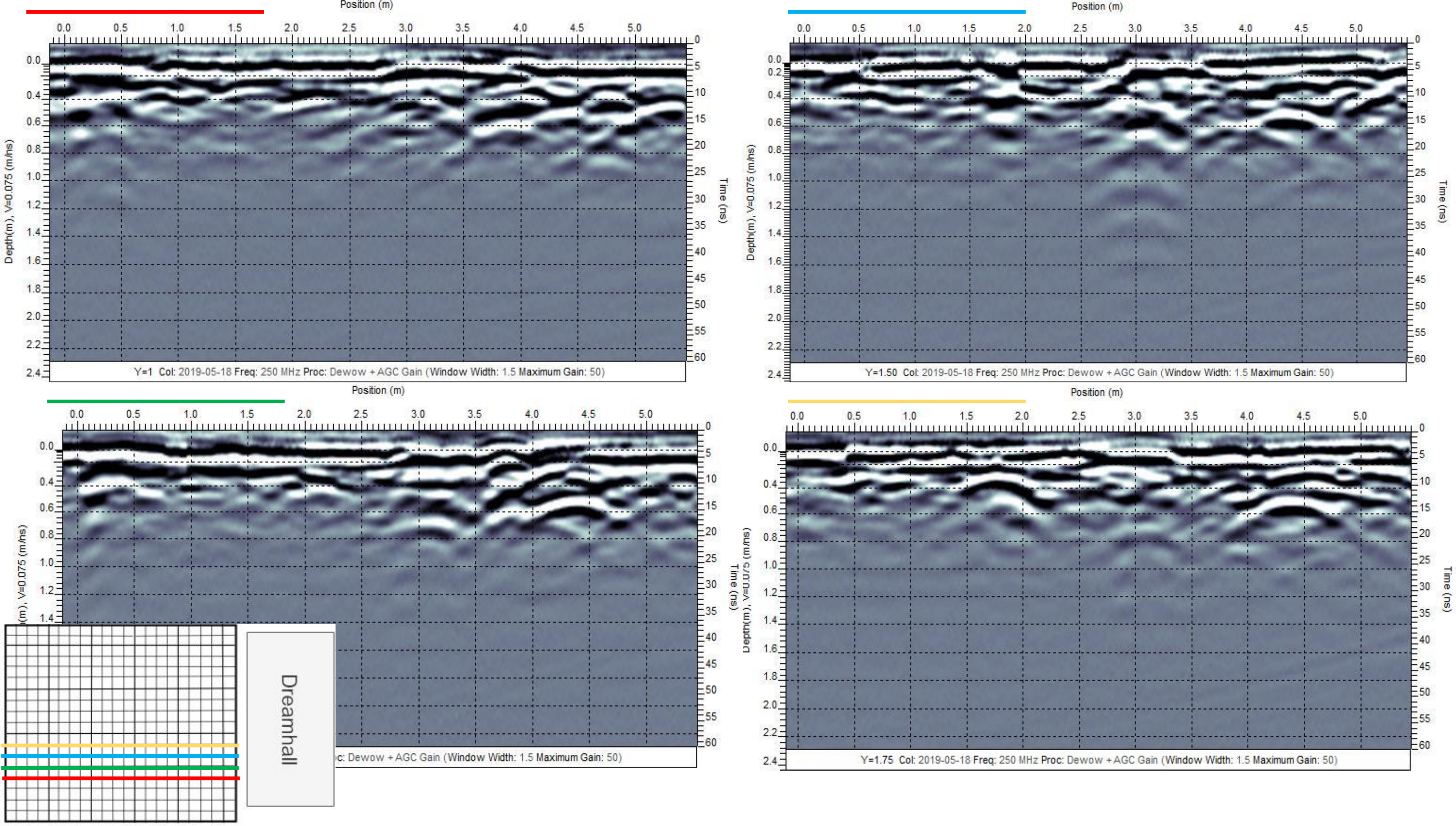

Figure A.29: Line Y=1.00, Y=1.25, Y=1.50, and Y=1.75 at the TU Delft site, 2019.

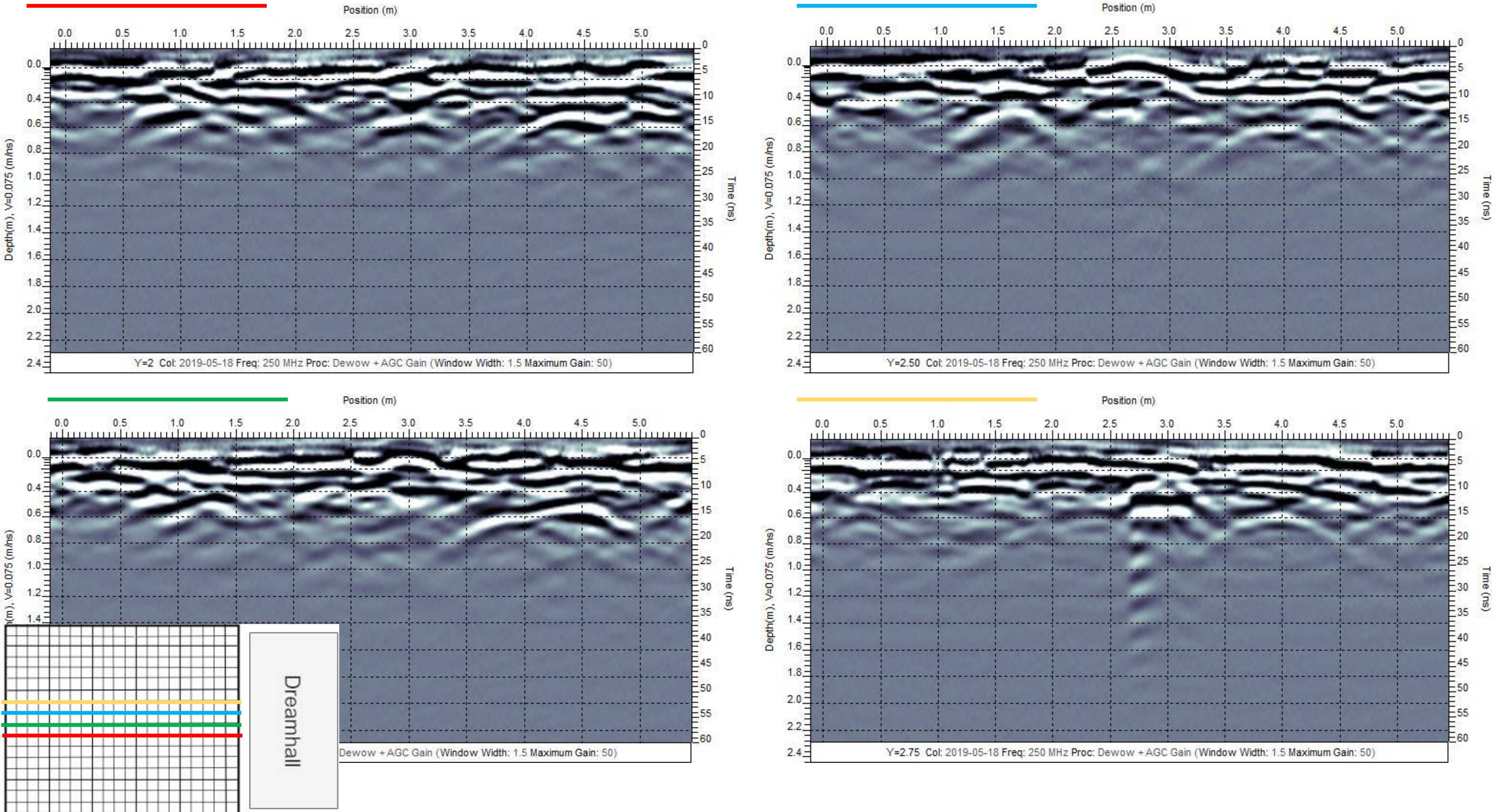

Figure A.30: Line Y=2.00, Y=2.25, Y=2.50, and Y=2.75 at the TU Delft site, 2019.

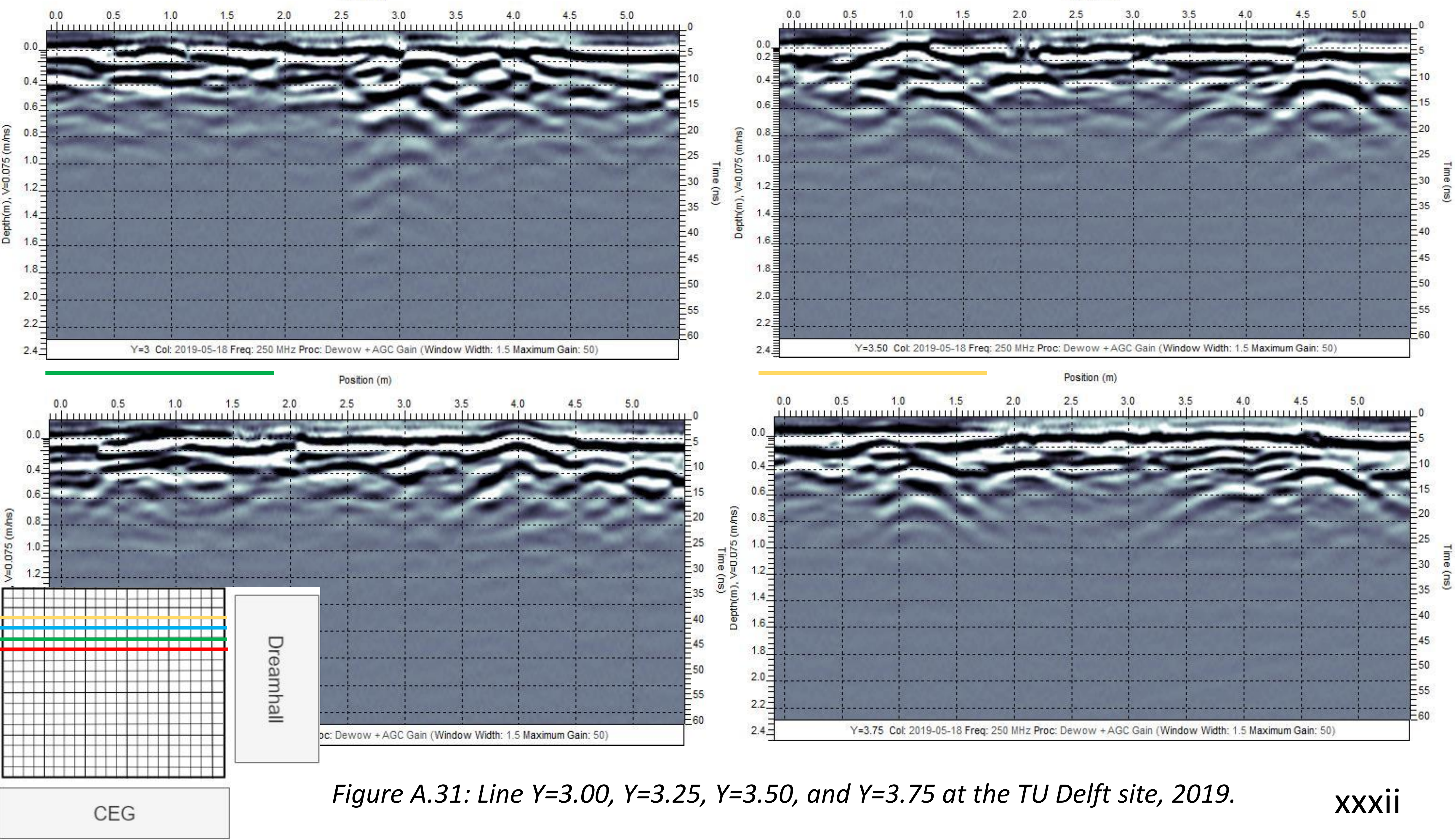

Figure A.31: Line Y=3.00, Y=3.25, Y=3.50, and Y=3.75 at the TU Delft site, 2019.

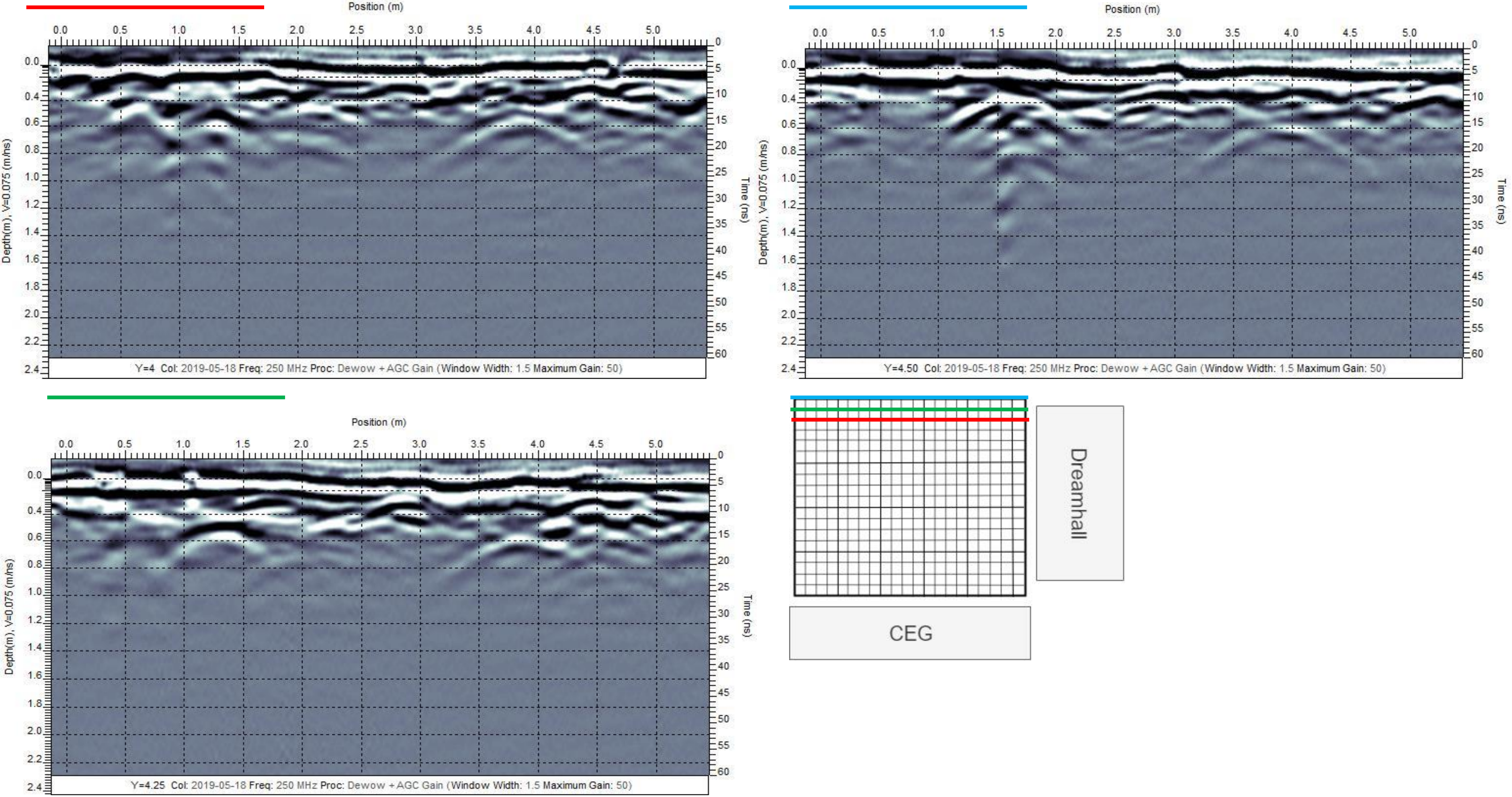

Figure A.31: Line Y=4.00, Y=4.25, and Y=4.50 at the TU Delft site, 2019.

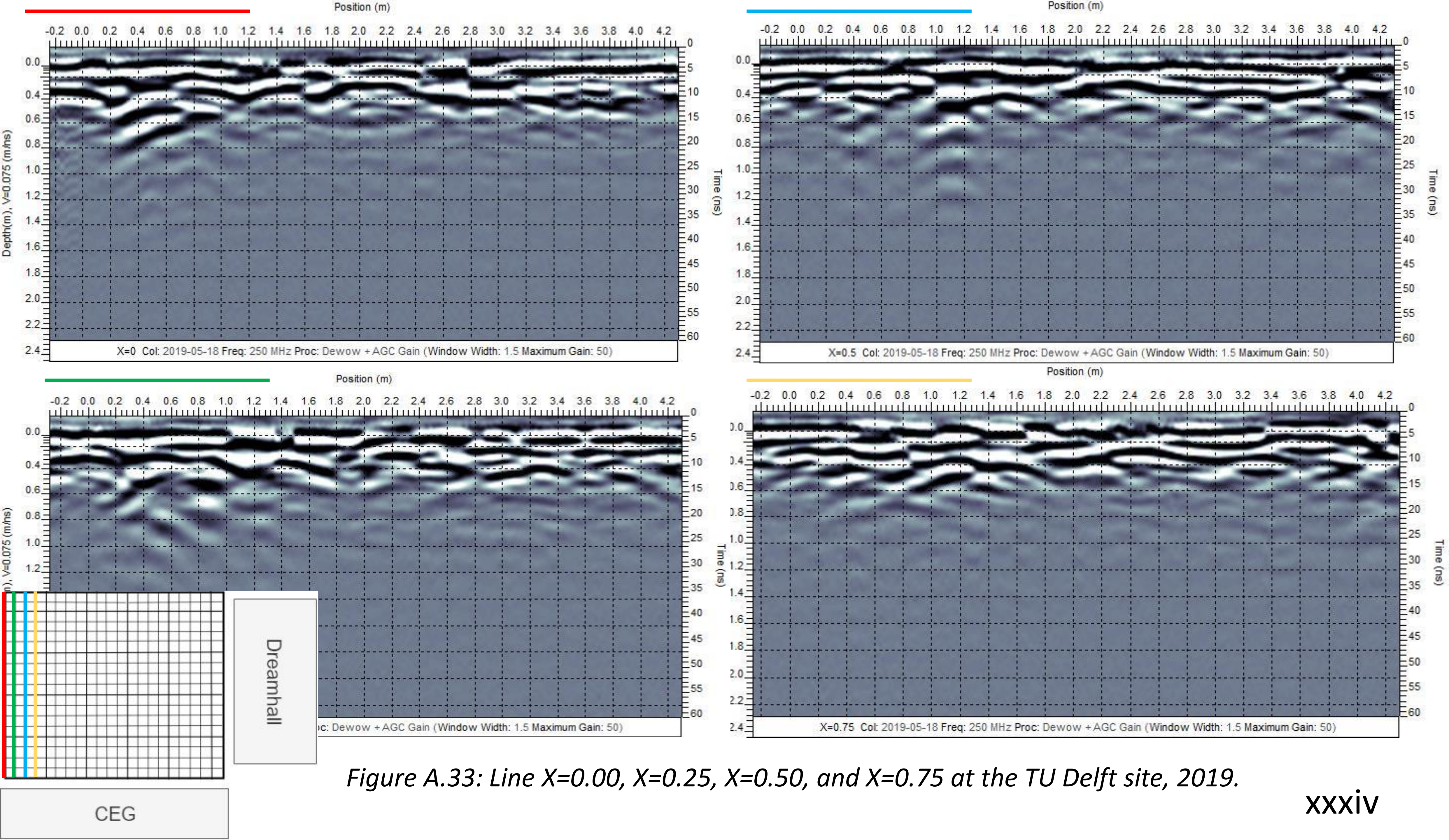

Figure A.33: Line X=0.00, X=0.25, X=0.50, and X=0.75 at the TU Delft site, 2019.

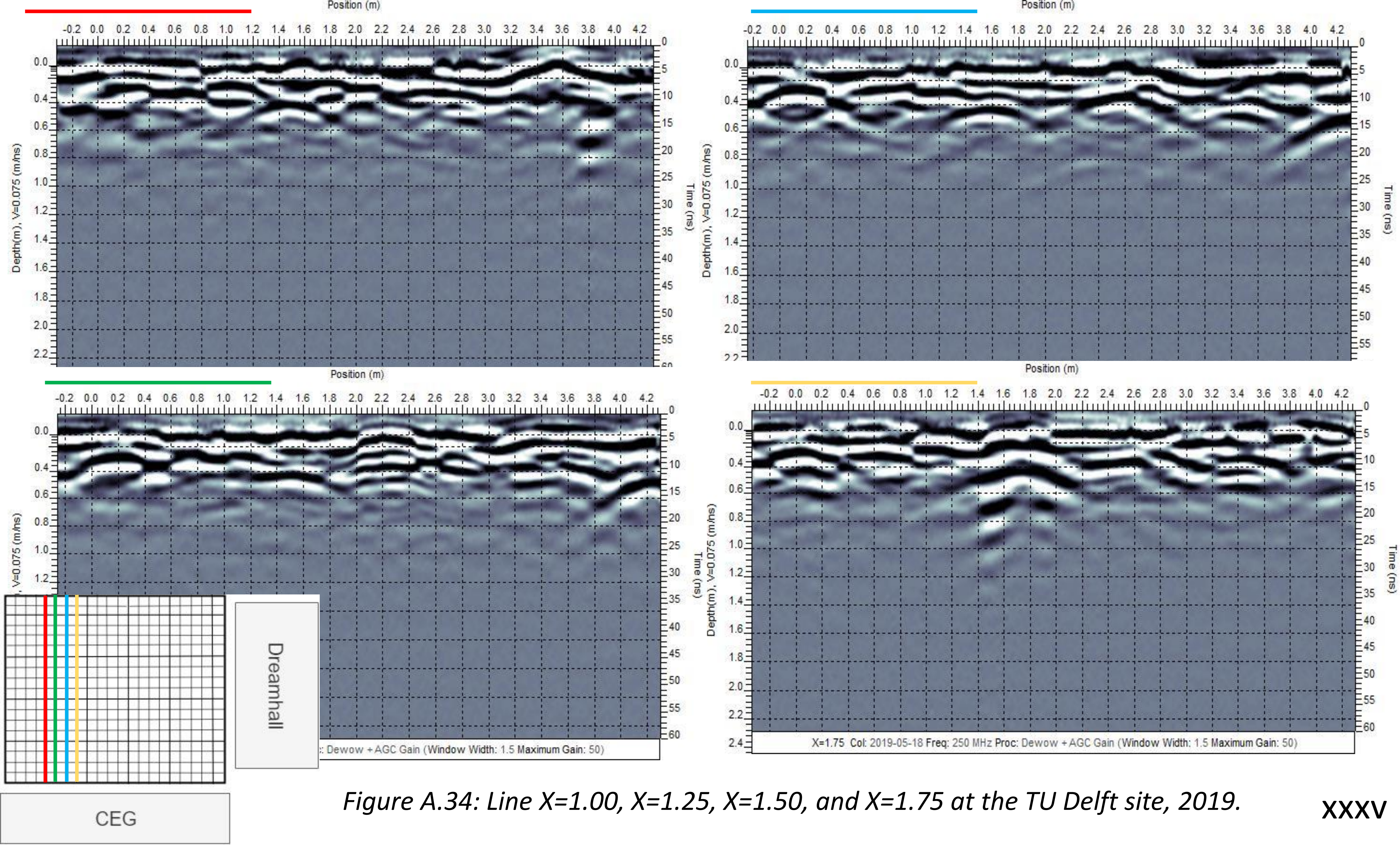

Figure A.34: Line X=1.00, X=1.25, X=1.50, and X=1.75 at the TU Delft site, 2019.

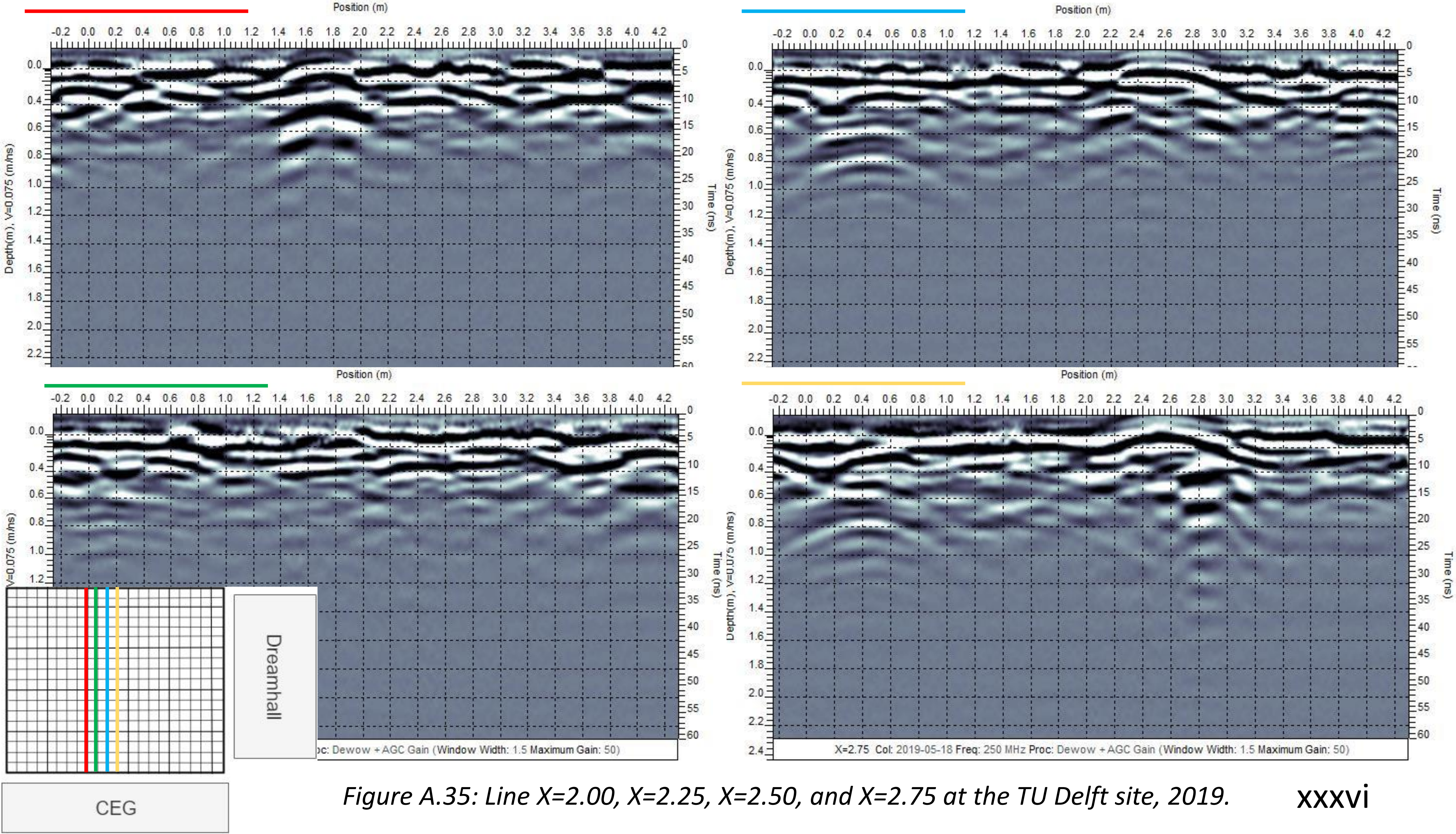

Figure A.35: Line X=2.00, X=2.25, X=2.50, and X=2.75 at the TU Delft site, 2019.

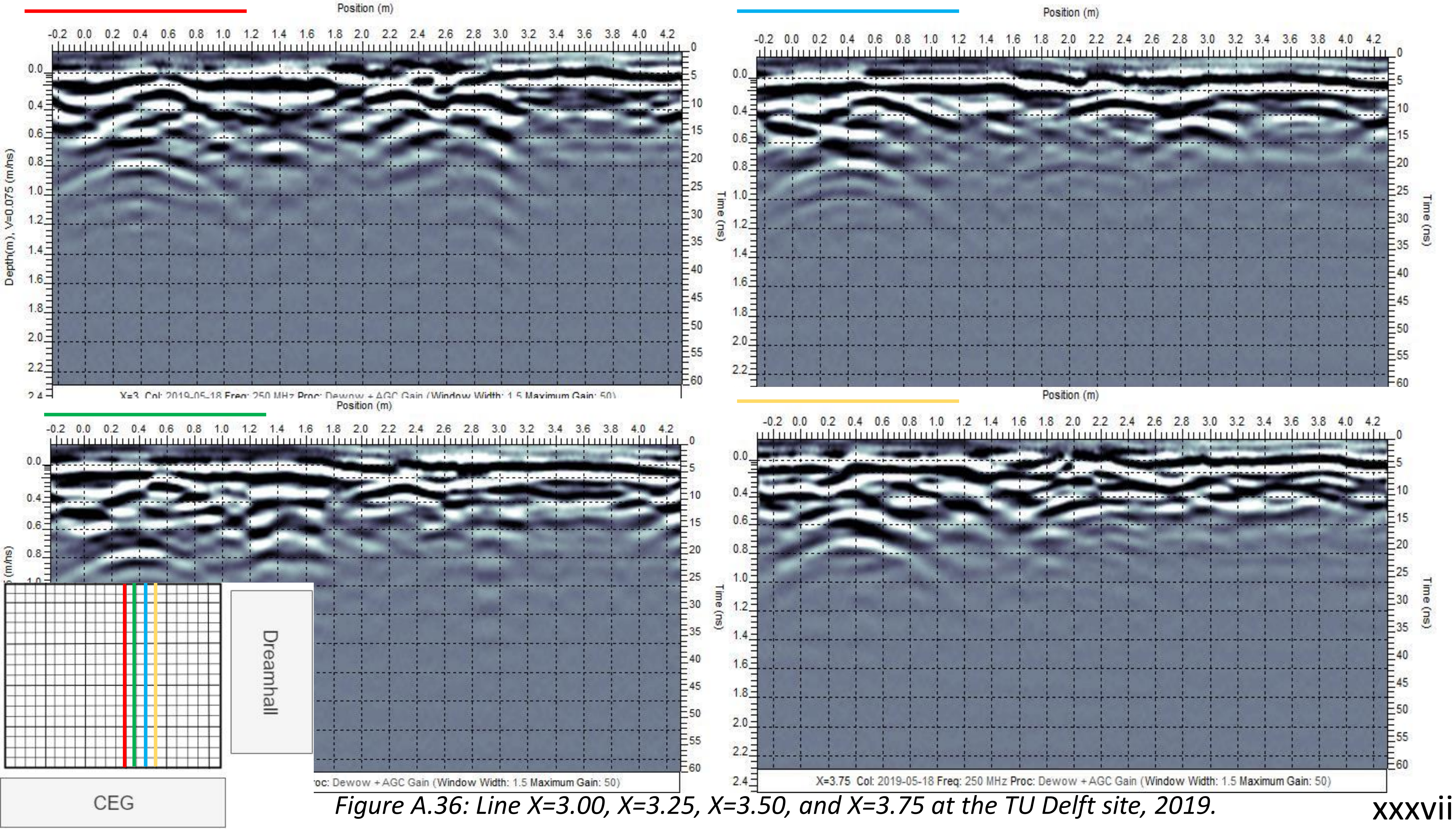

Figure A.36: Line X=3.00, X=3.25, X=3.50, and X=3.75 at the TU Delft site, 2019.

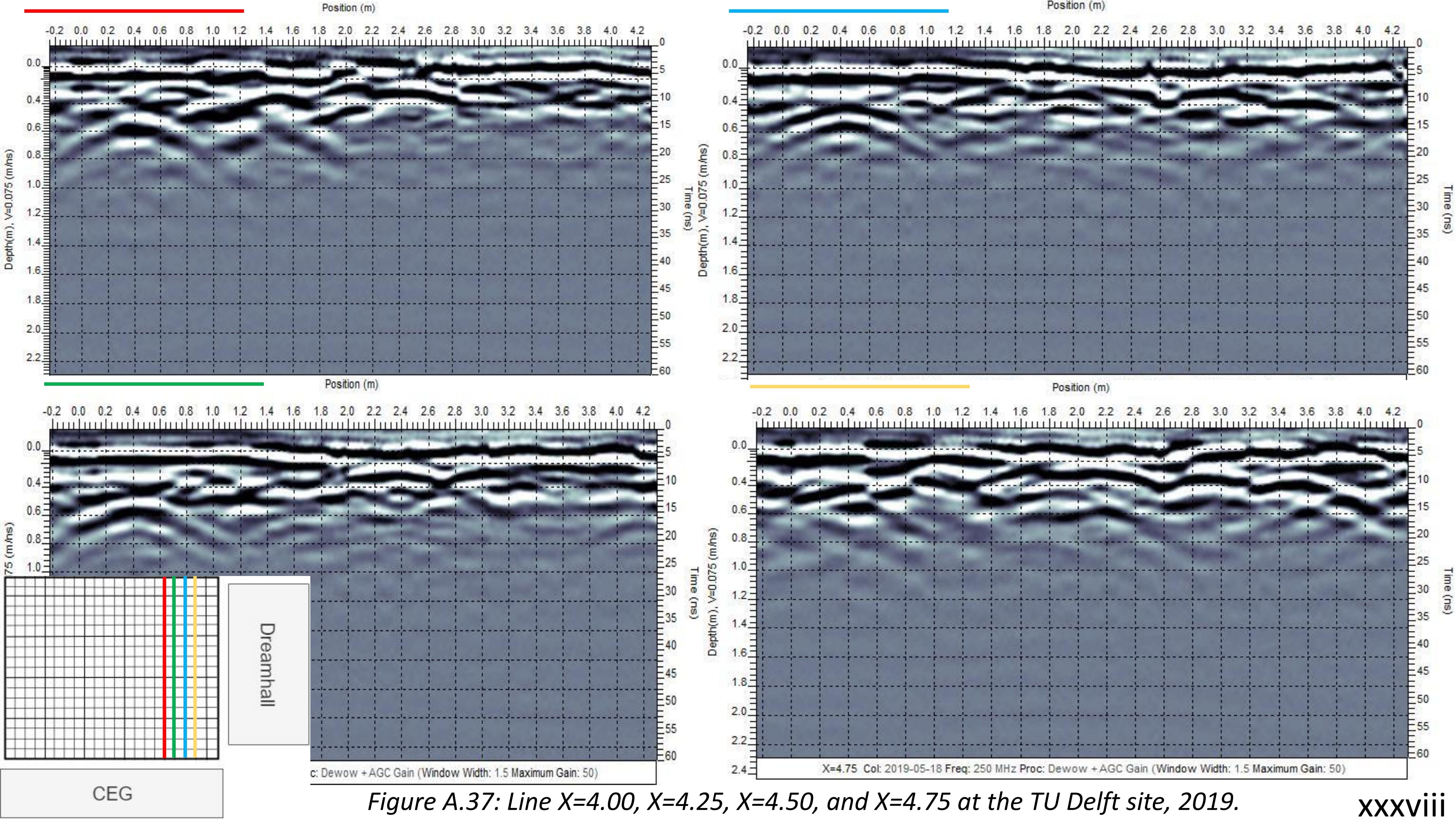

Figure A.37: Line X=4.00, X=4.25, X=4.50, and X=4.75 at the TU Delft site, 2019.

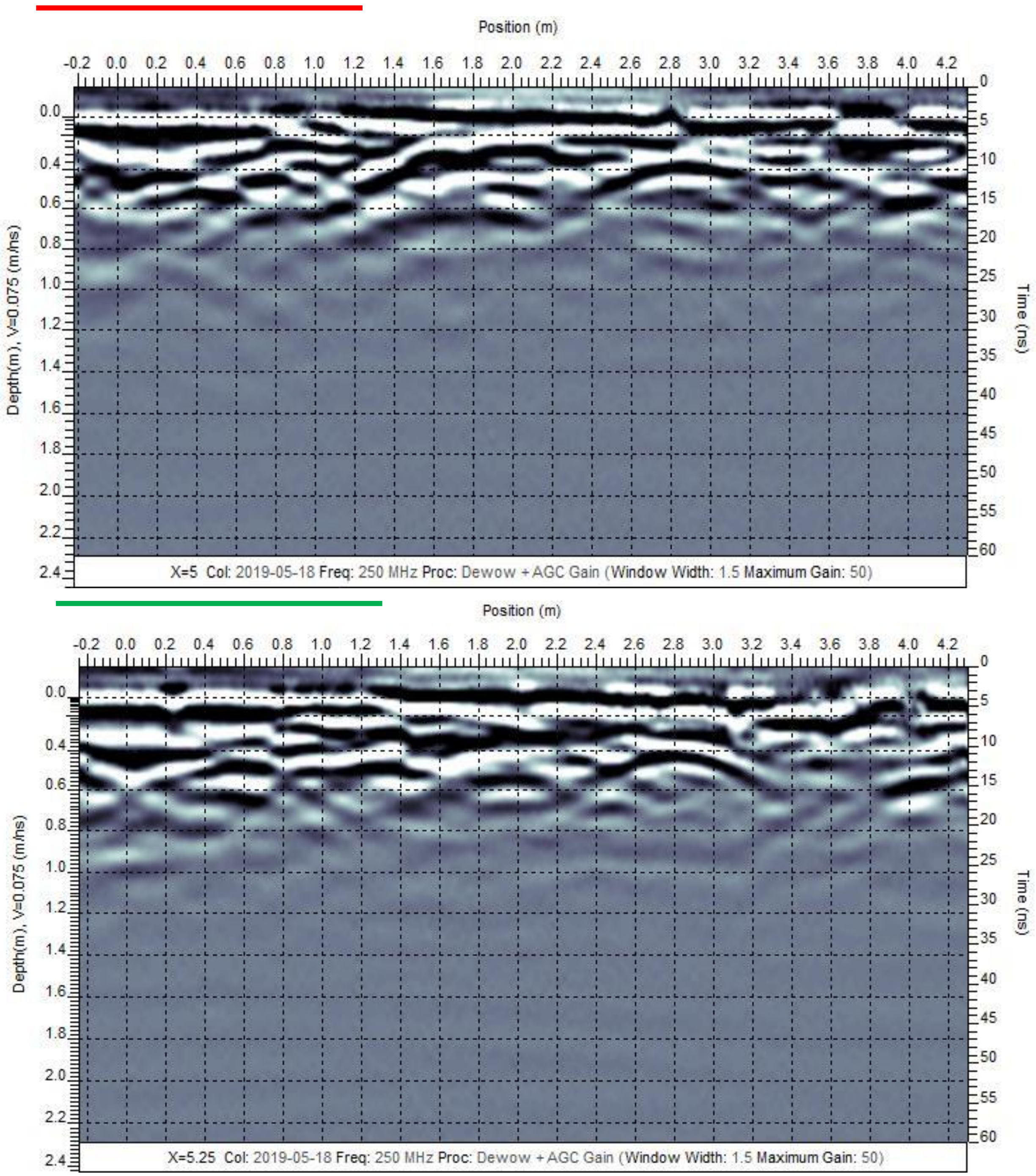

Figure A.38: Line X=5.00, and X=5.25 at the TU Delft site, 2019.

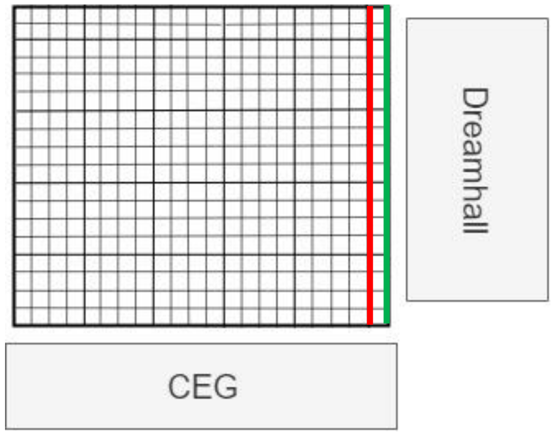

Appendix B

This appendix presents the results of each processing step for the common-offset GPR data, as well as some typical amplitude spectra for each site. Table B.1 shows the parameters used for the filters.

Table B.1: Parameters for processing common-offset data

Process	Parameters
Dewow	-
Repick timezero	1% of maximum amplitude
Background subtraction	Average of all traces
Bandpass filter	0, 50, 500, 600 MHz
AGC	Maximum 50 gain, window width 1.5

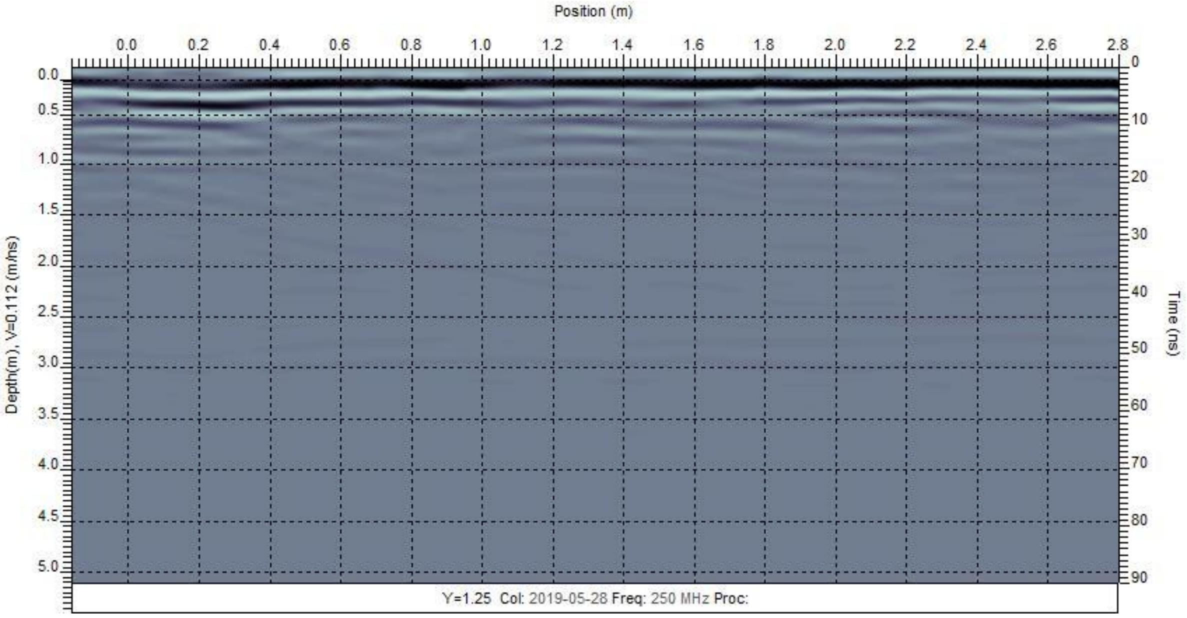

Figure B.1: Line Y=1.25 over burial at ARISTA facility with no processing.

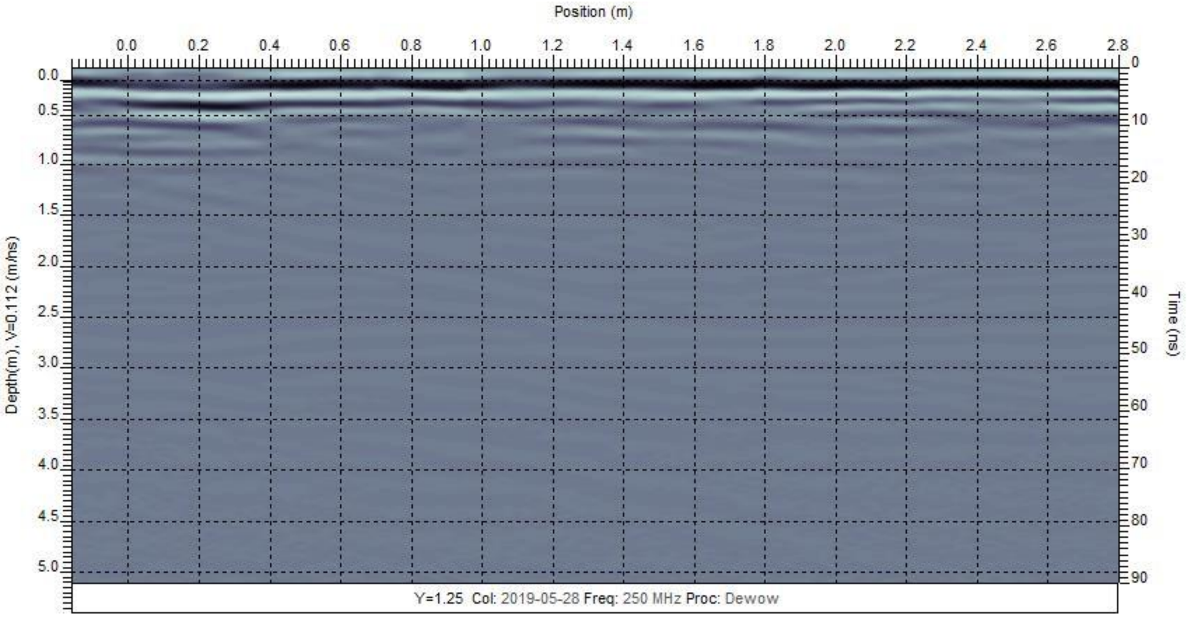

Figure B.2: Line Y=1.25 over burial at ARISTA facility after dewowing.

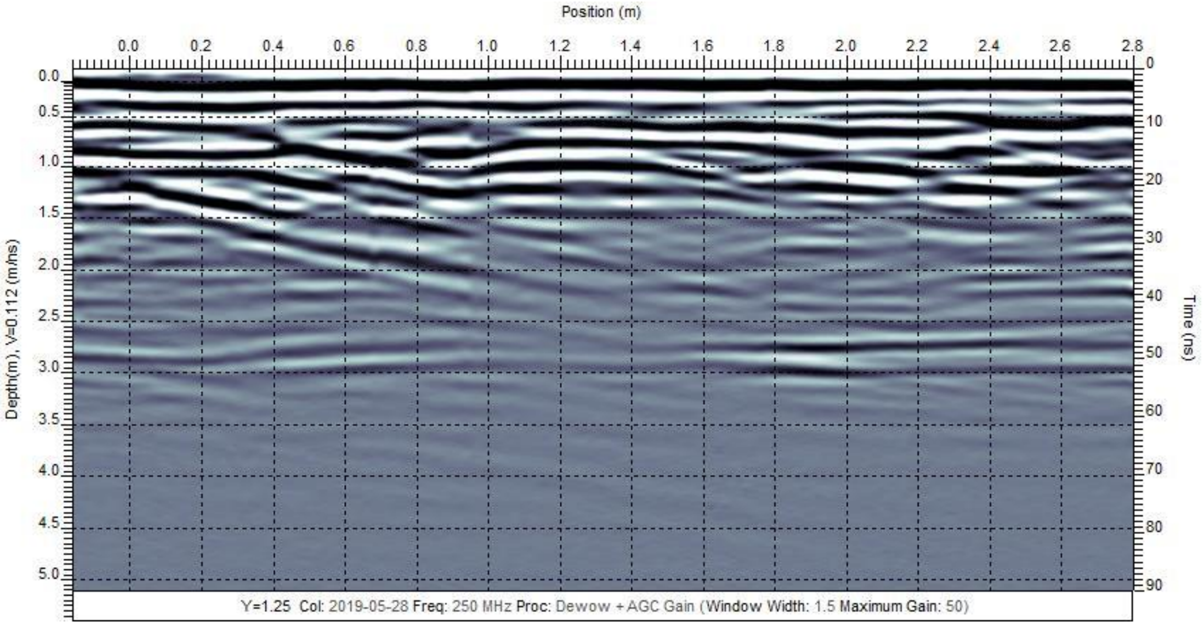

Figure B.3: Line Y=1.25 over burial at ARISTA facility with dewow and AGC.

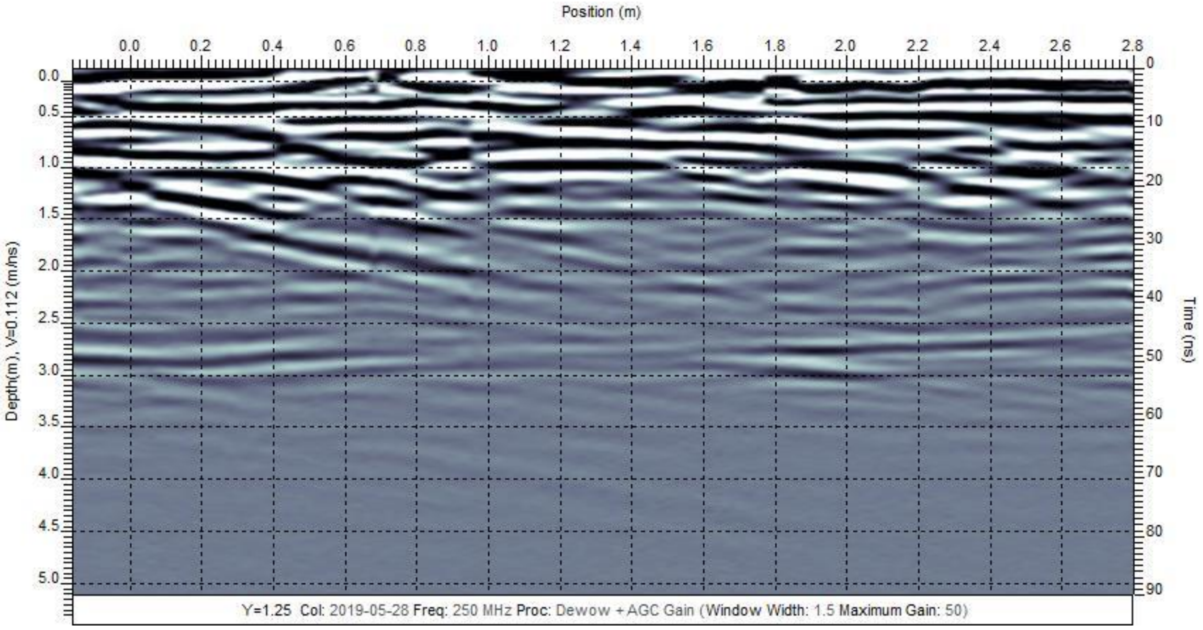

Figure B.4: Line Y=1.25 over burial at ARISTA facility with dewow, AGC and background subtraction.

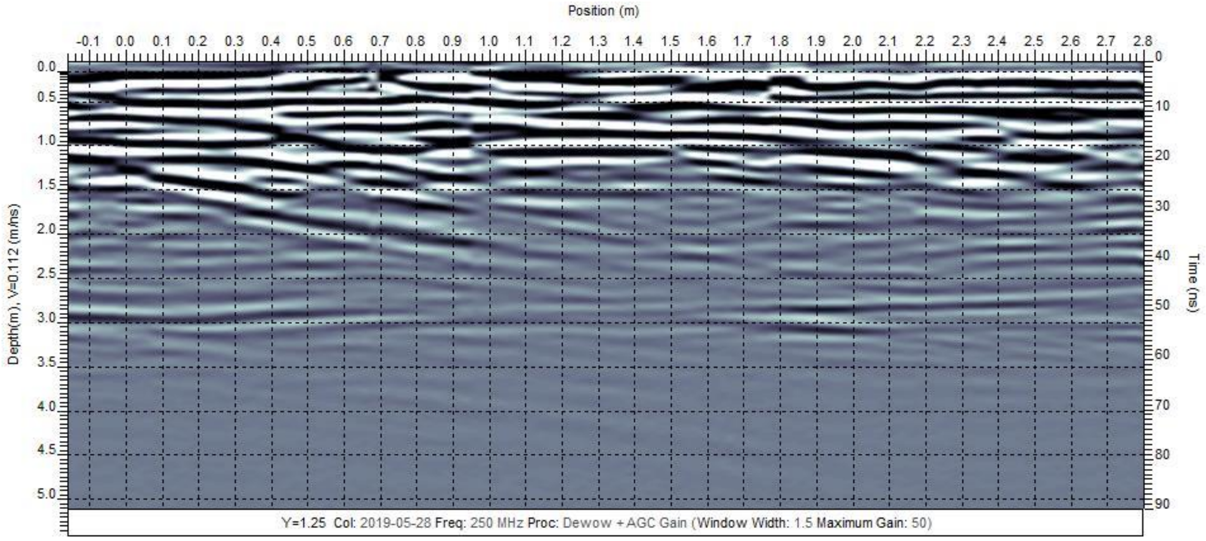

Figure B.5: Line Y=1.25 over burial at ARISTA facility with dewow, AGC, background subtraction, and bandpass filtering.

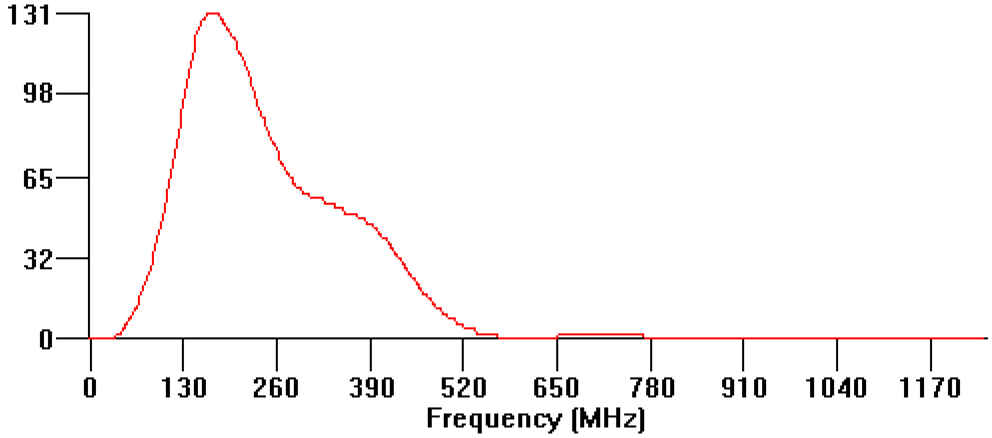

Figure B.6: A typical amplitude spectrum at the TU Delft investigation site.

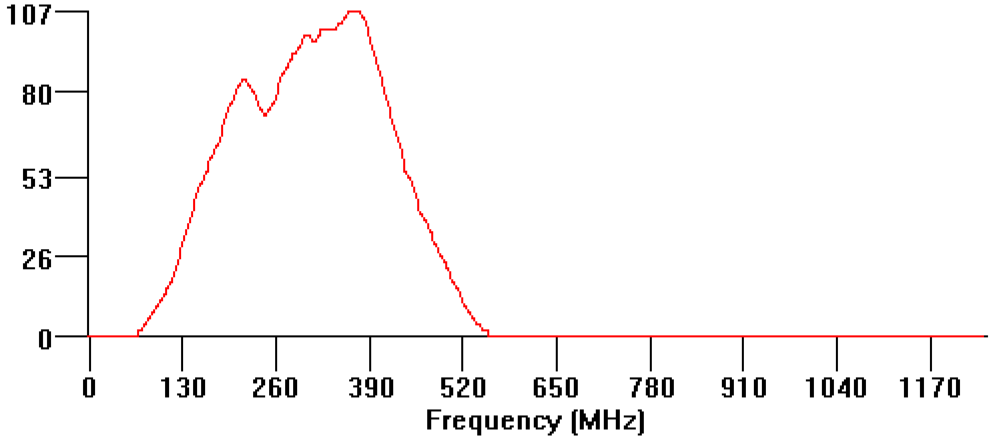

Figure B.7: A typical amplitude spectrum at the ARISTA facility.

Appendix C

This appendix presents full size images of all images from the processing and results of the multiple-offset GPR data, for easier comparison. All images are with reference to source position 10 on line Y=1.50 over the burial at the ARISTA facility.

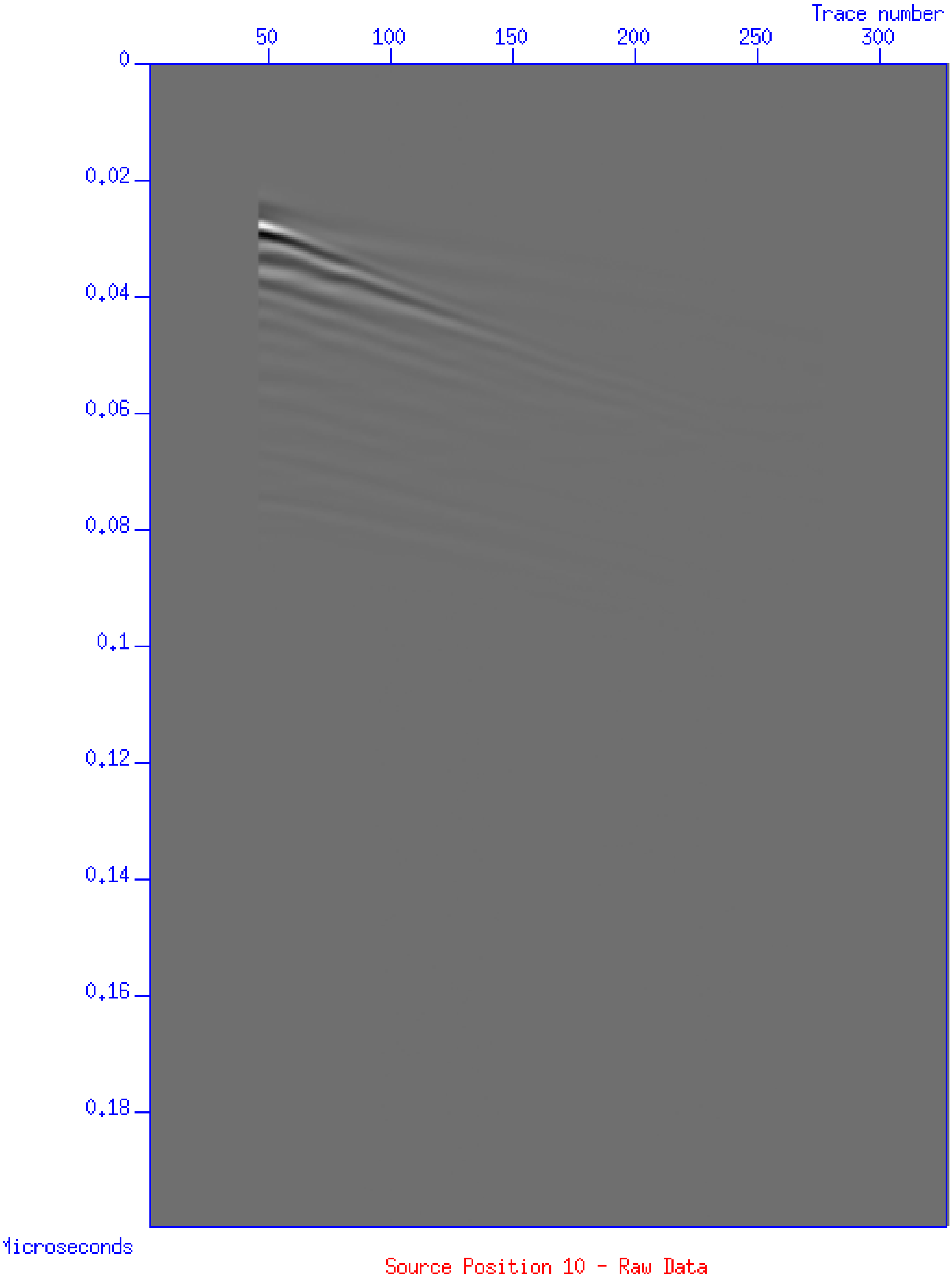

Figure C.1: Dewowed raw data

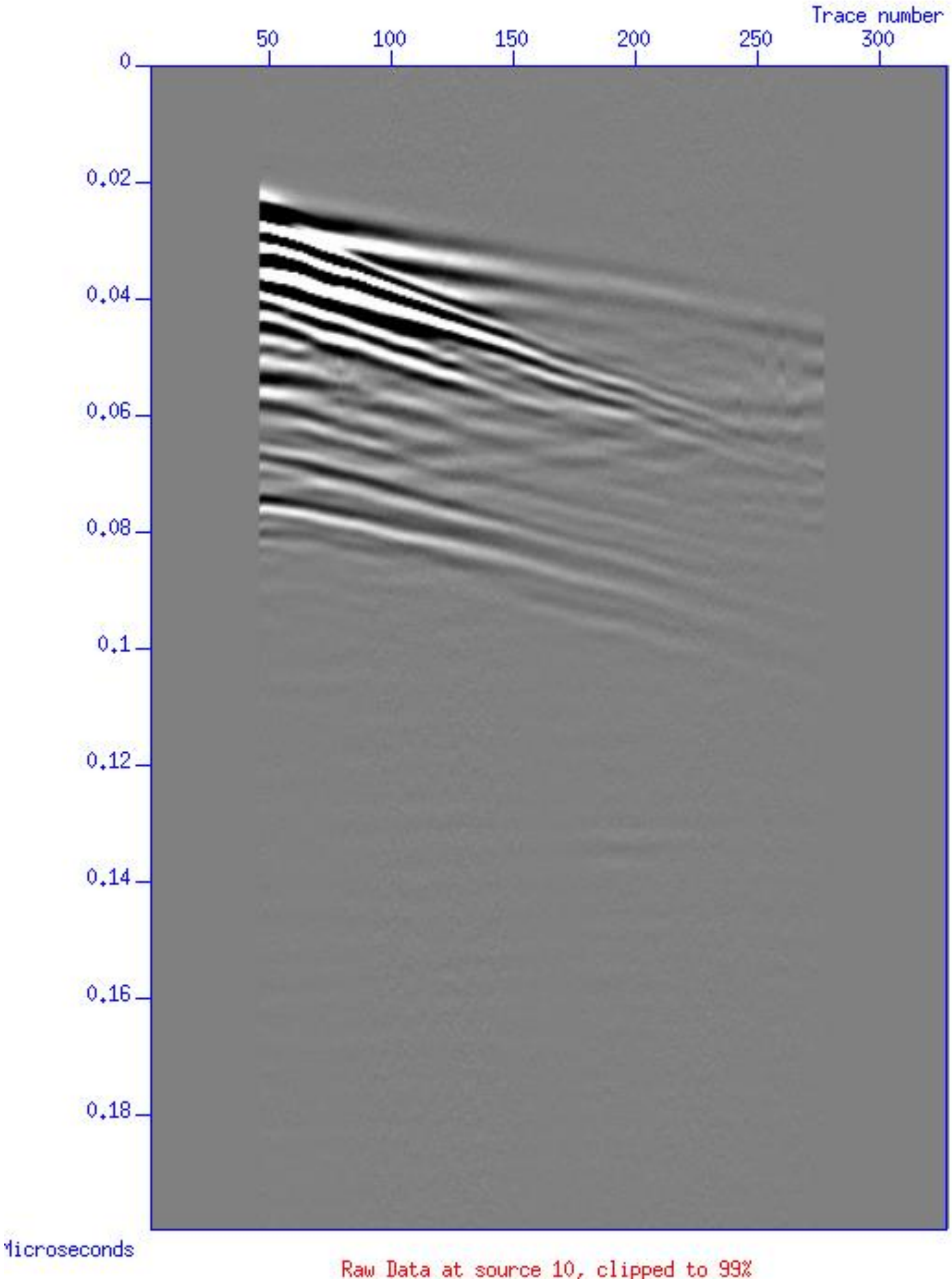

Figure C.2: Dewowed raw data clipped to 99% of maximum amplitude

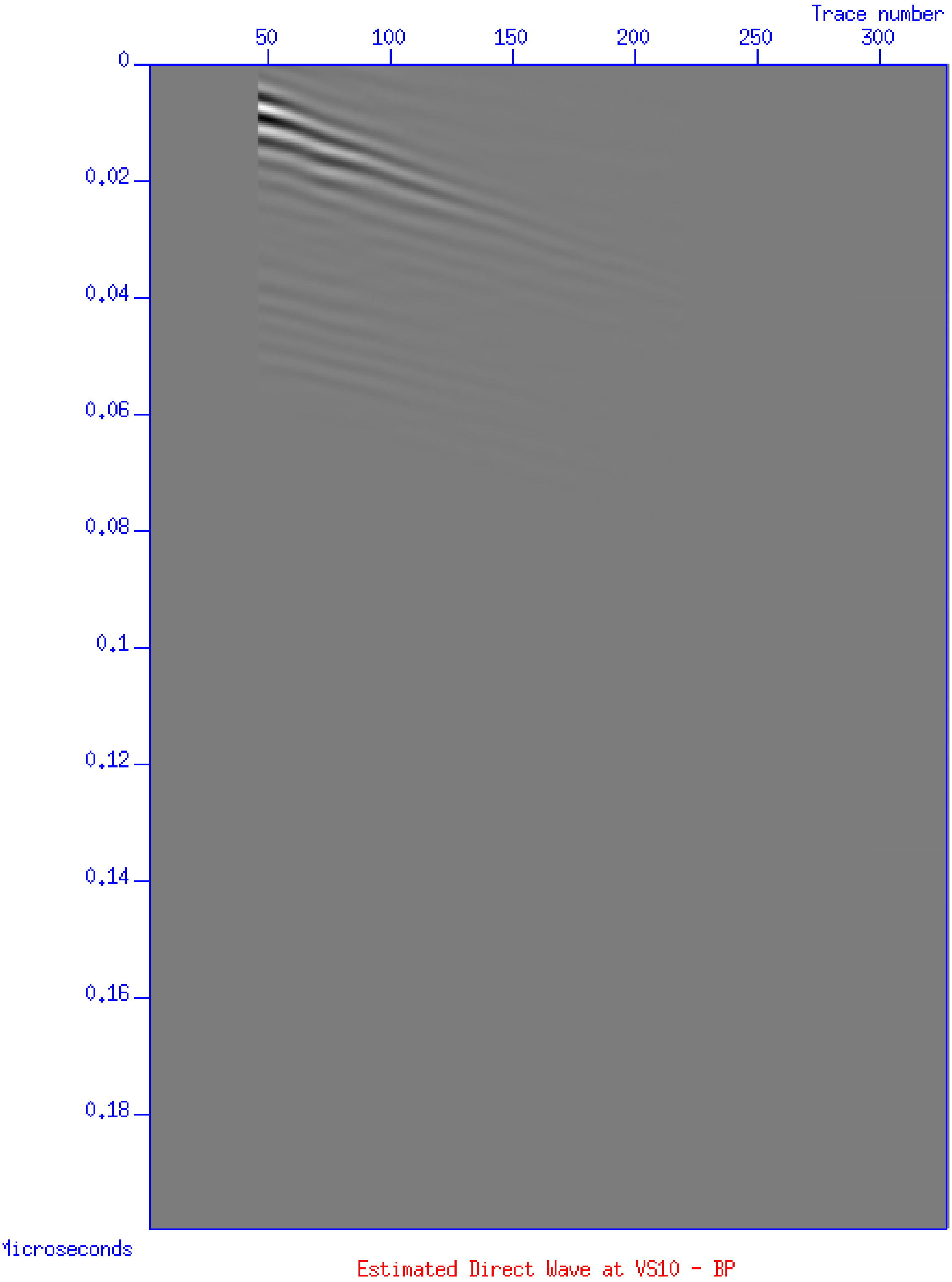

Figure C.3: Retrieved direct wave using bandpass filter isolation

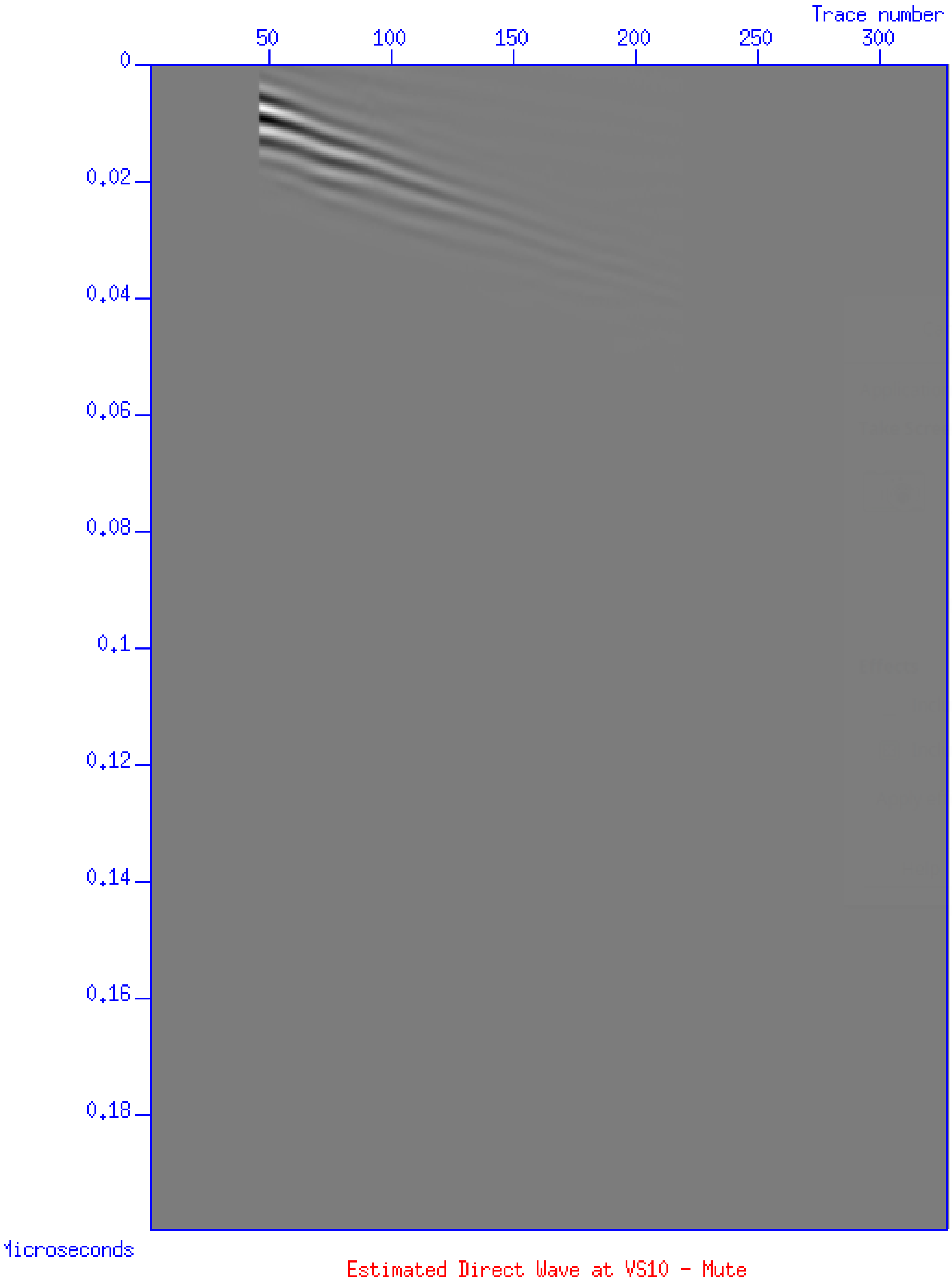

Figure C.4: Retrieved direct wave using topmute isolation

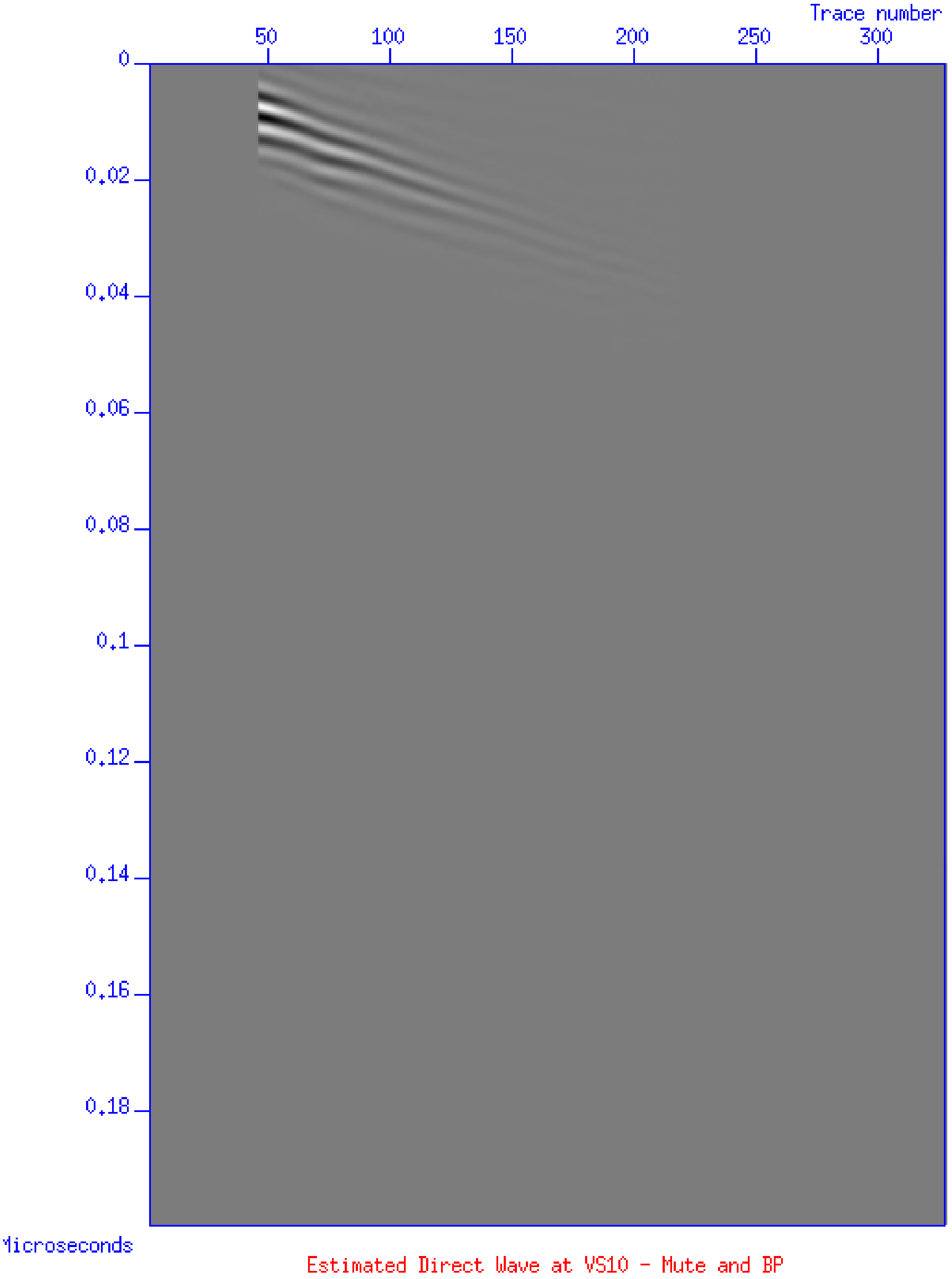

Figure C.5: Retrieved direct wave using bandpass filter and topmute isolation

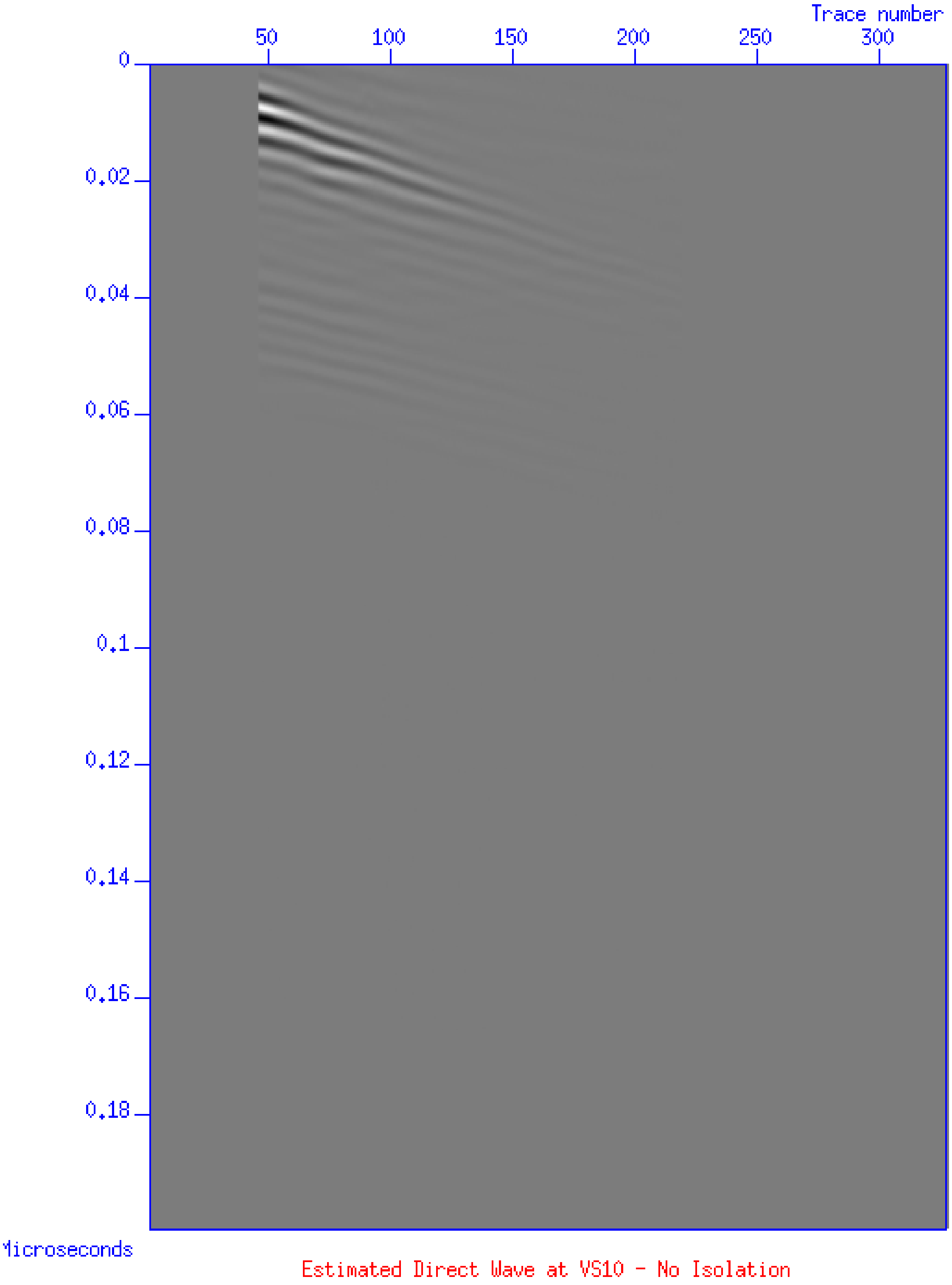

Figure C.6: Retrieved direct wave using no isolation

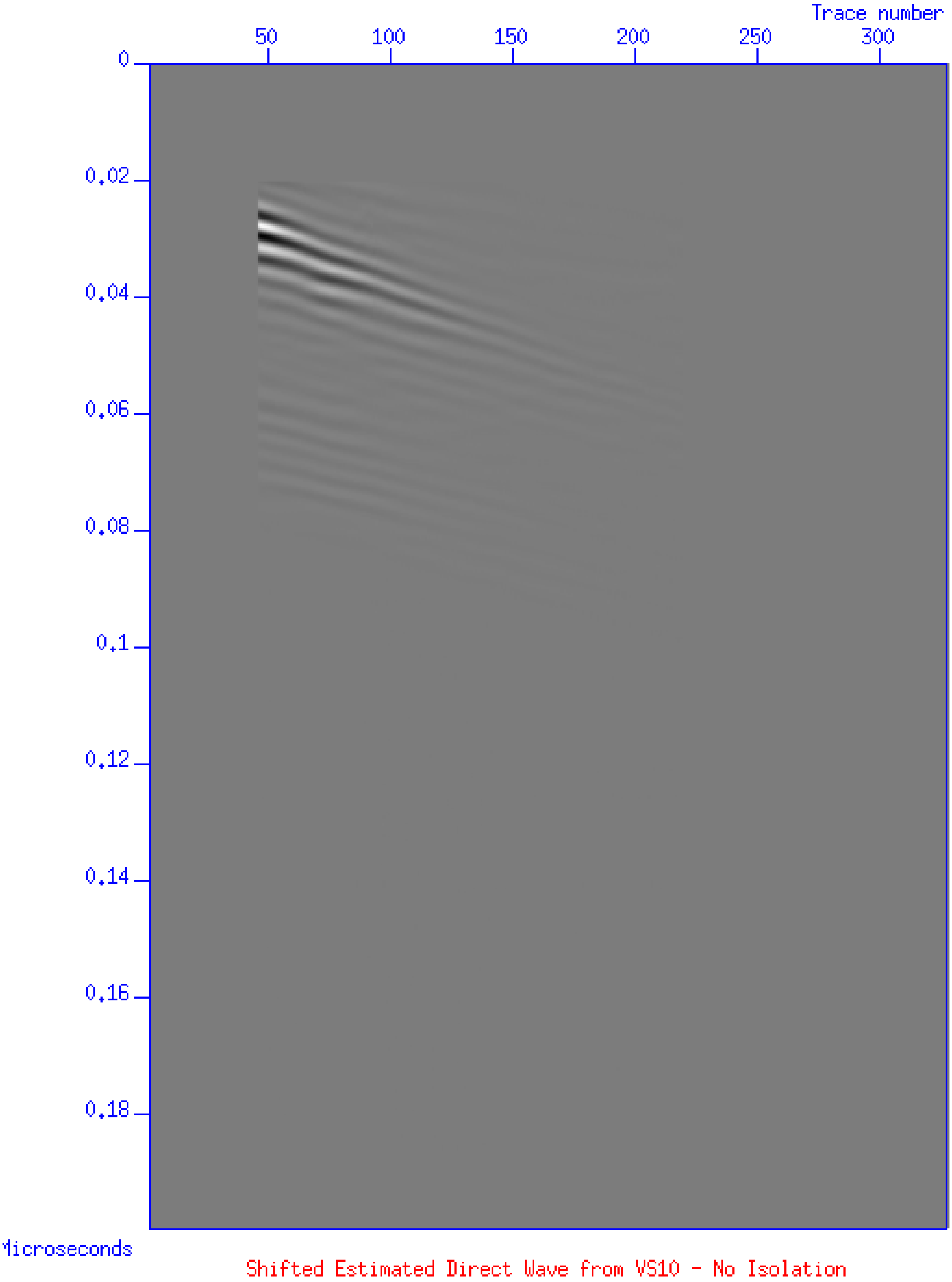

Figure C.7: Retrieved direct wave using no isolation after correcting timeshift

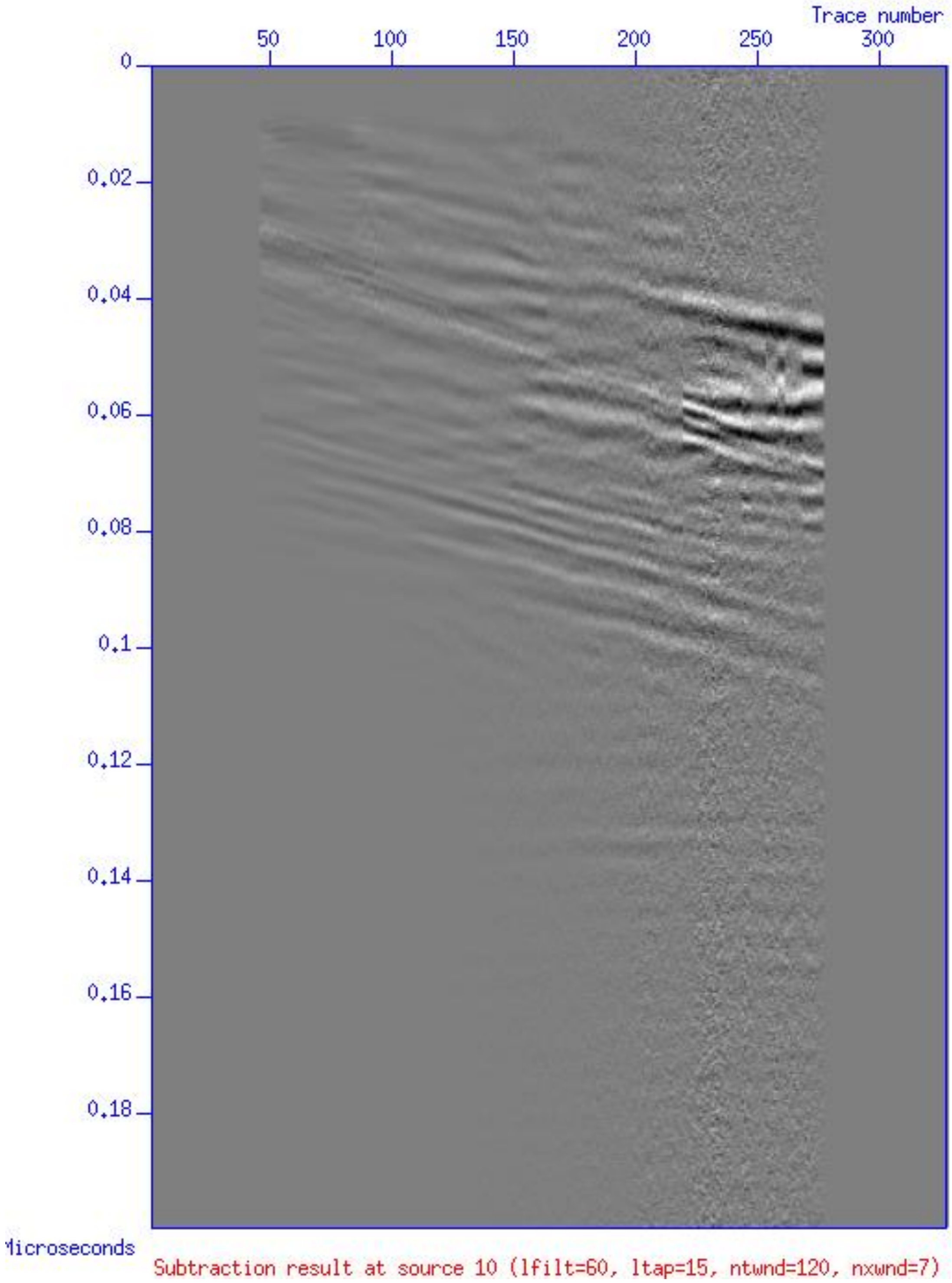

Figure C.8: Subtraction result using parameters lfilt=60, ltap=15, ntwnd=120, nxwnd=7.

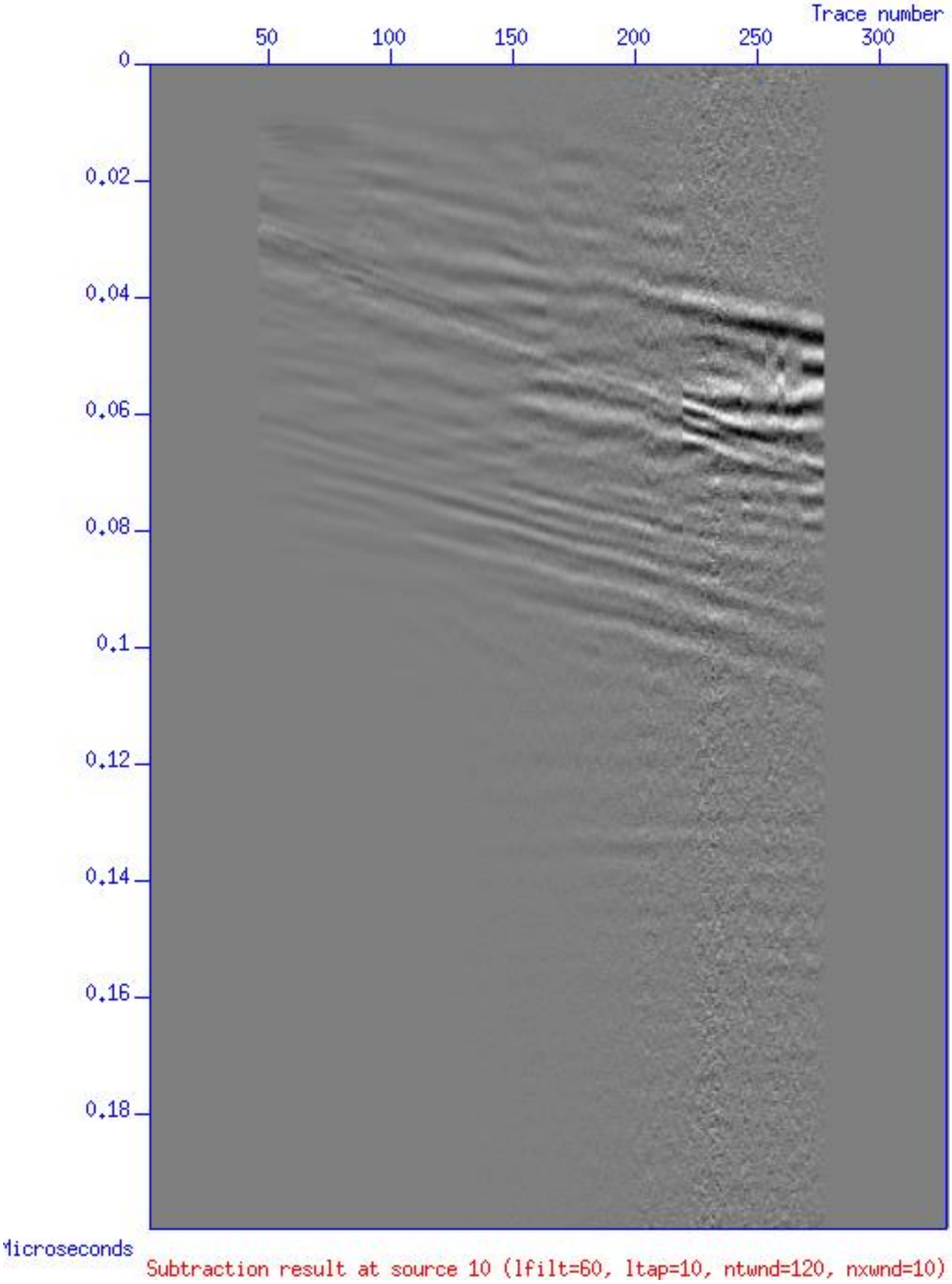

Figure C.9: Subtraction result using parameters lfilt=60, ltap=10, ntwnd=120, nxwnd=10.

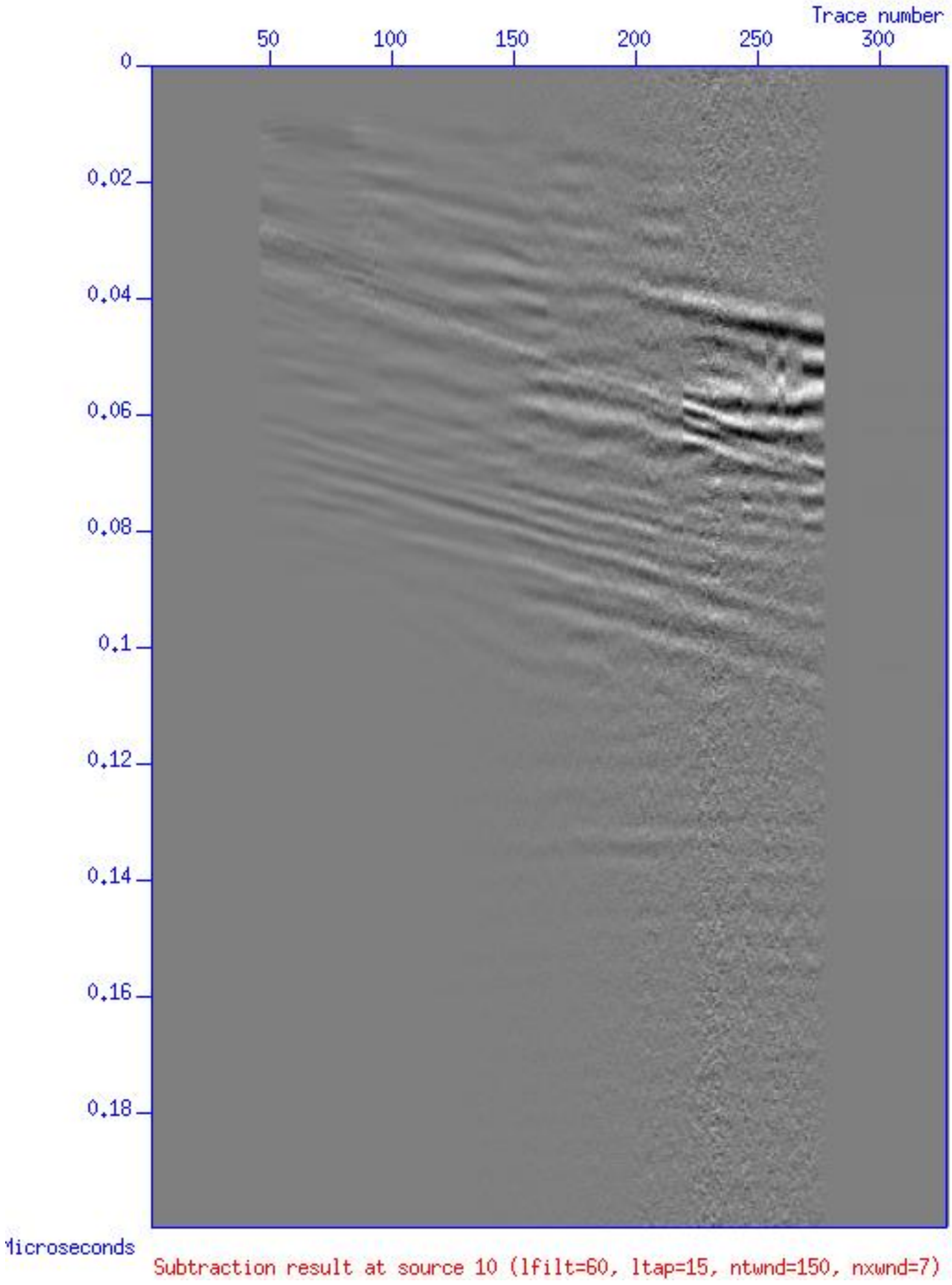

Figure C.10: Subtraction result using parameters lfilt=60, ltap=15, ntwnd=150, nxwnd=7.

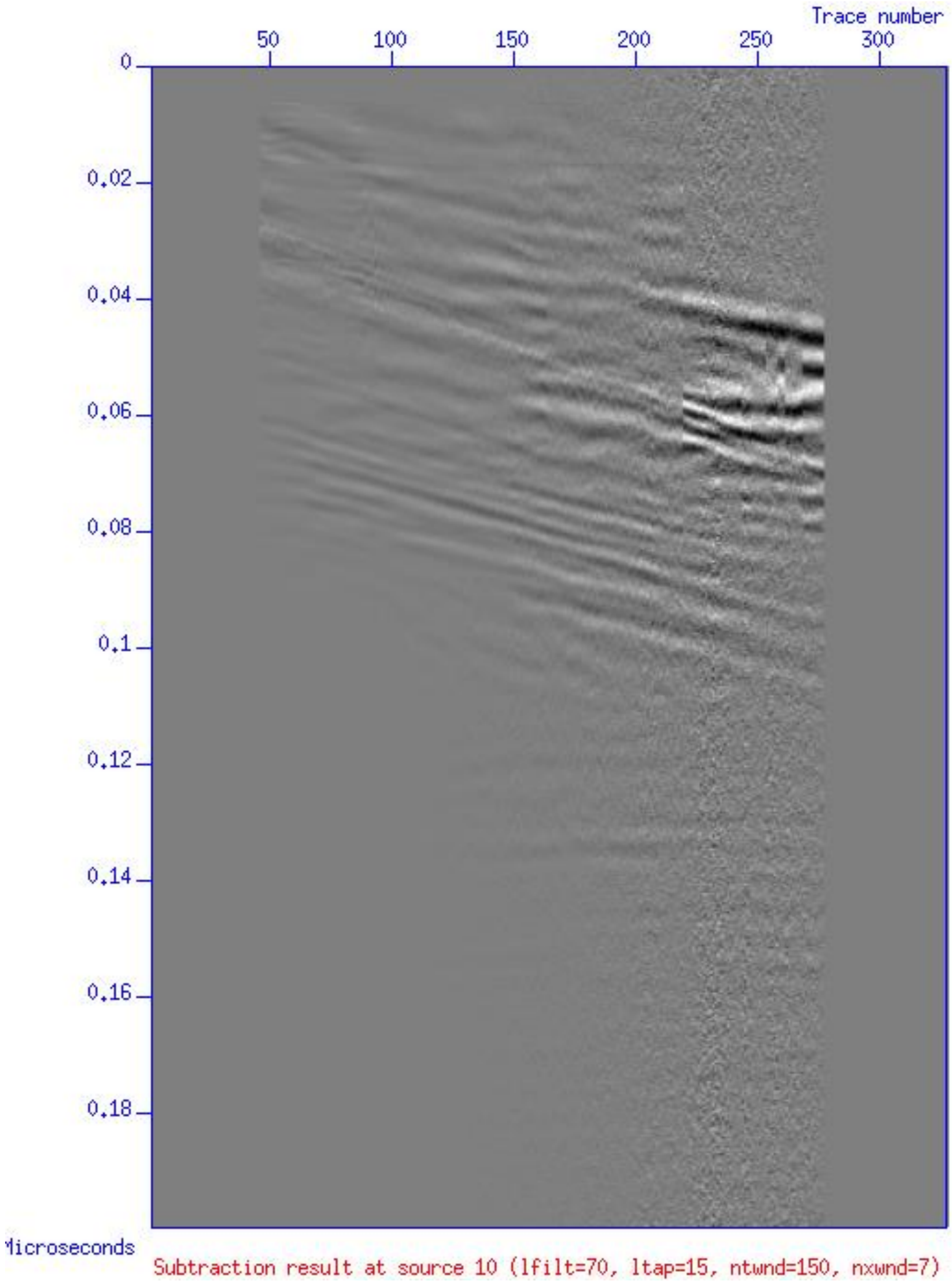

Figure C.11: Subtraction result using parameters lfilt=70, ltap=15, ntwnd=150, nxwnd=7.

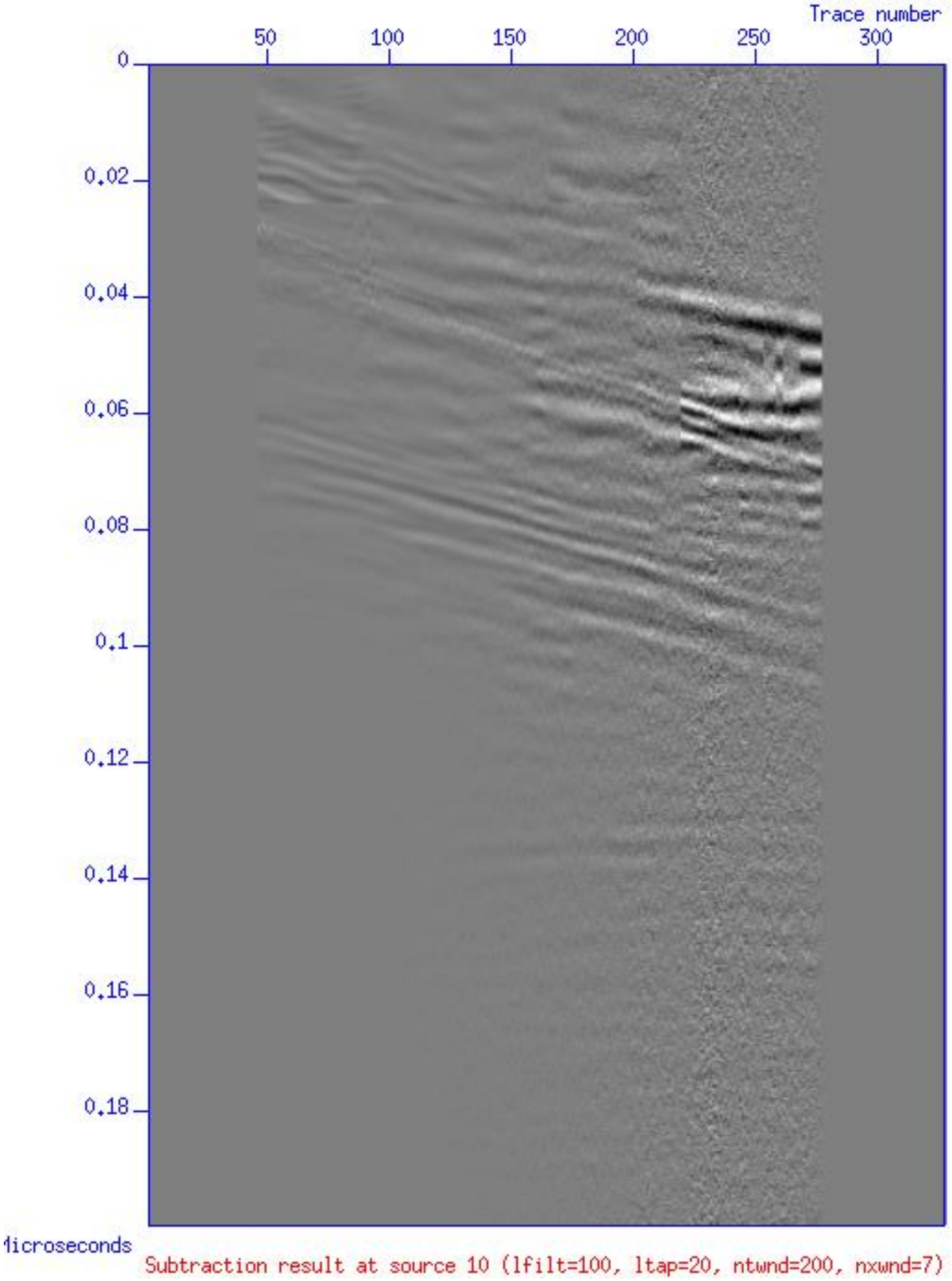

Figure C.12: Subtraction result using parameters lfilt=100, ltap=20, ntwnd=200, nxwnd=7.

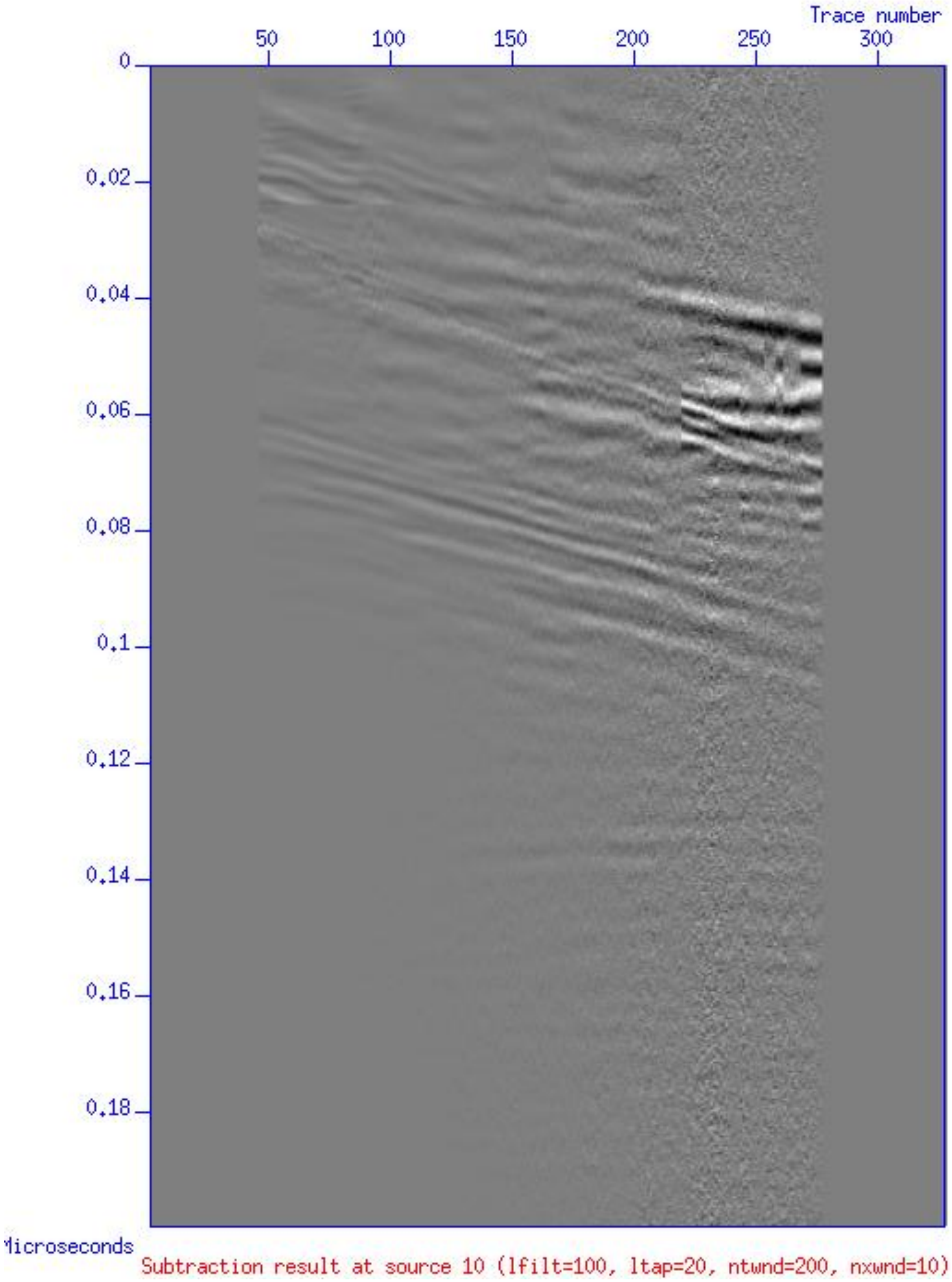

Figure C.13: Subtraction result using parameters lfilt=100, ltap=20, ntwnd=200, nxwnd=10.

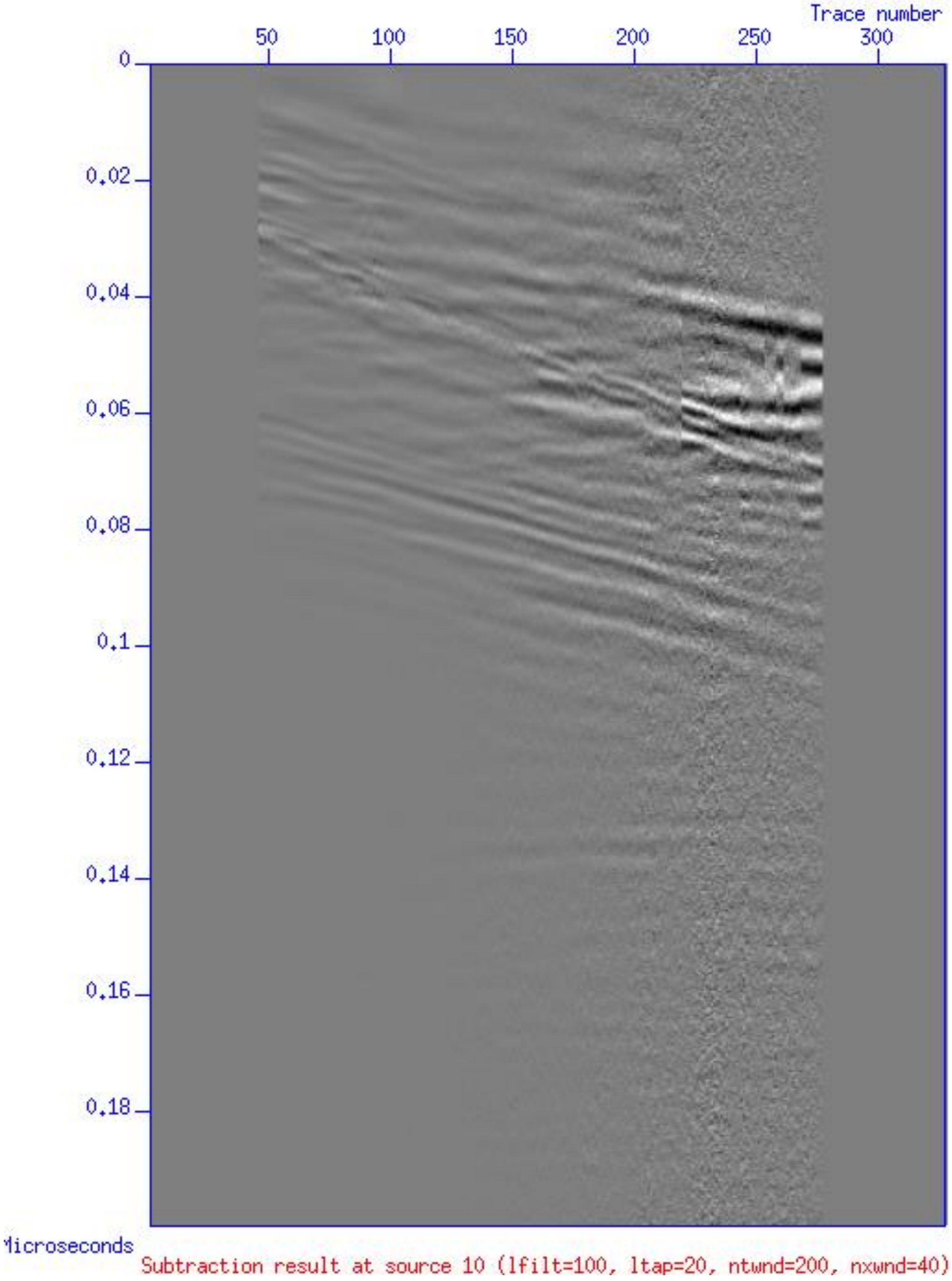

Figure C.14: Subtraction result using parameters lfilt=100, ltap=20, ntwnd=200, nxwnd=40.

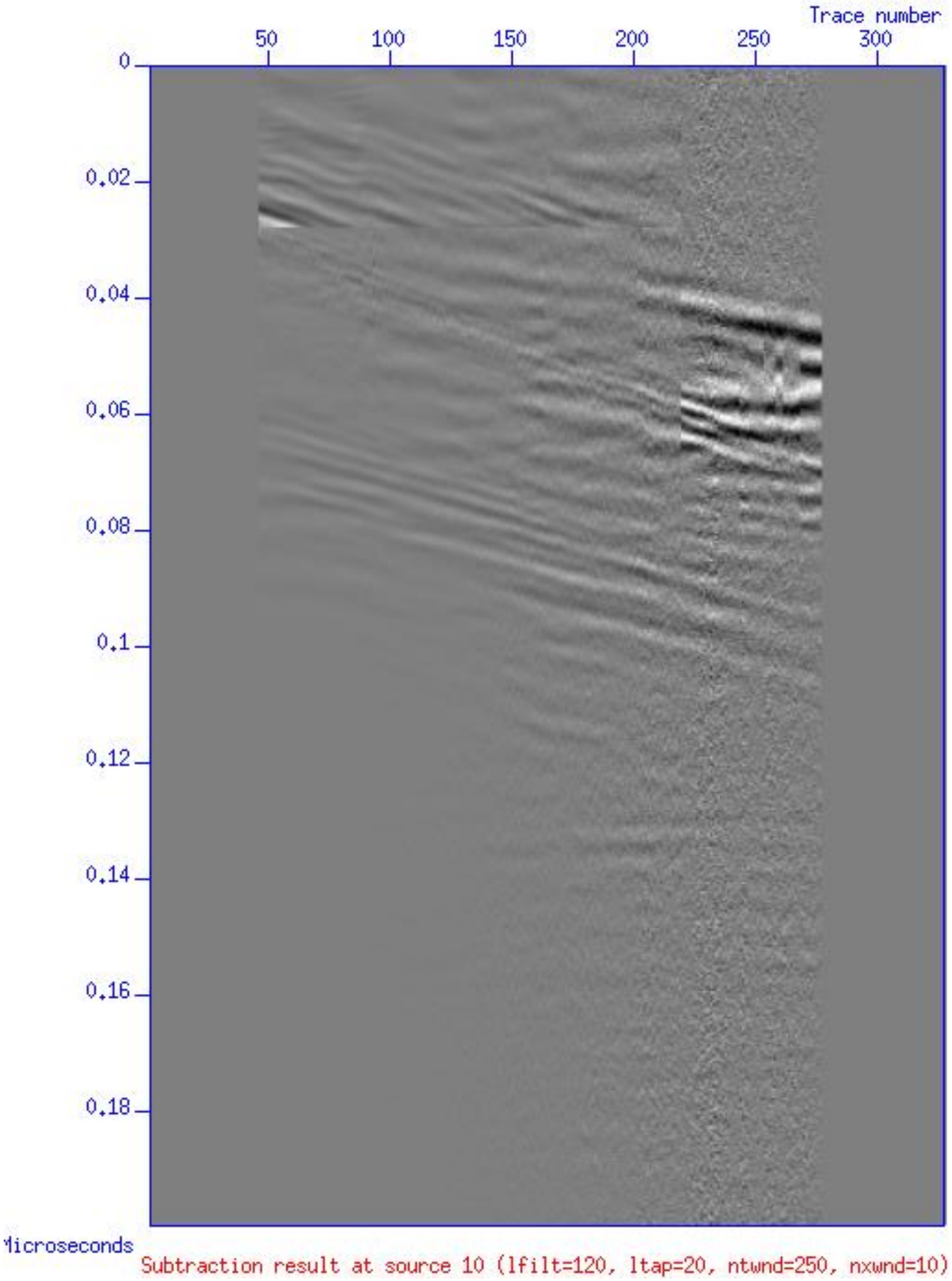

Figure C.15: Subtraction result using parameters lfilt=120, ltap=20, ntwnd=250, nxwnd=10.

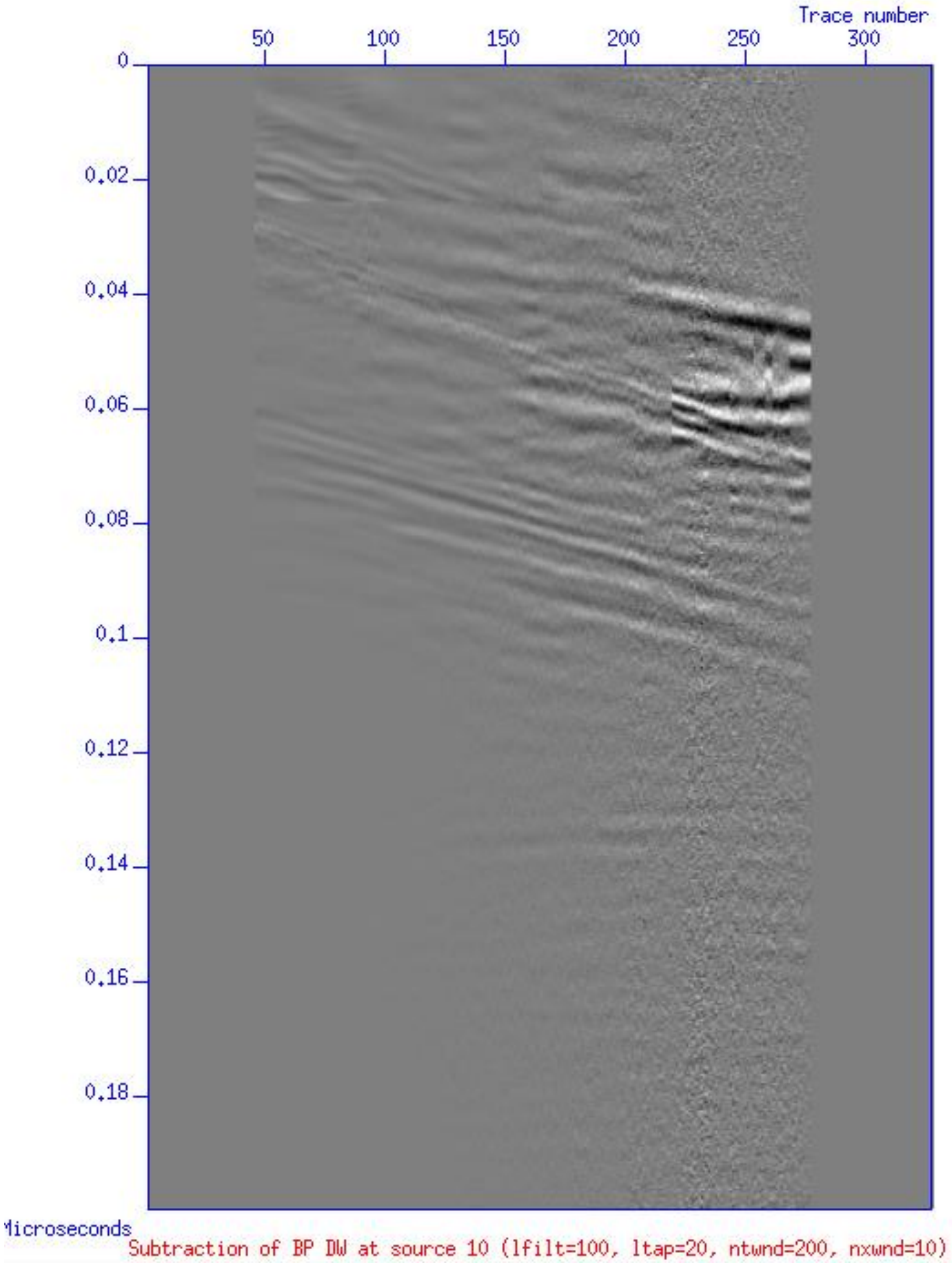

Figure C.16: Subtraction result using parameters lfilt=100, ltap=20, ntwnd=200, nxwnd=10.

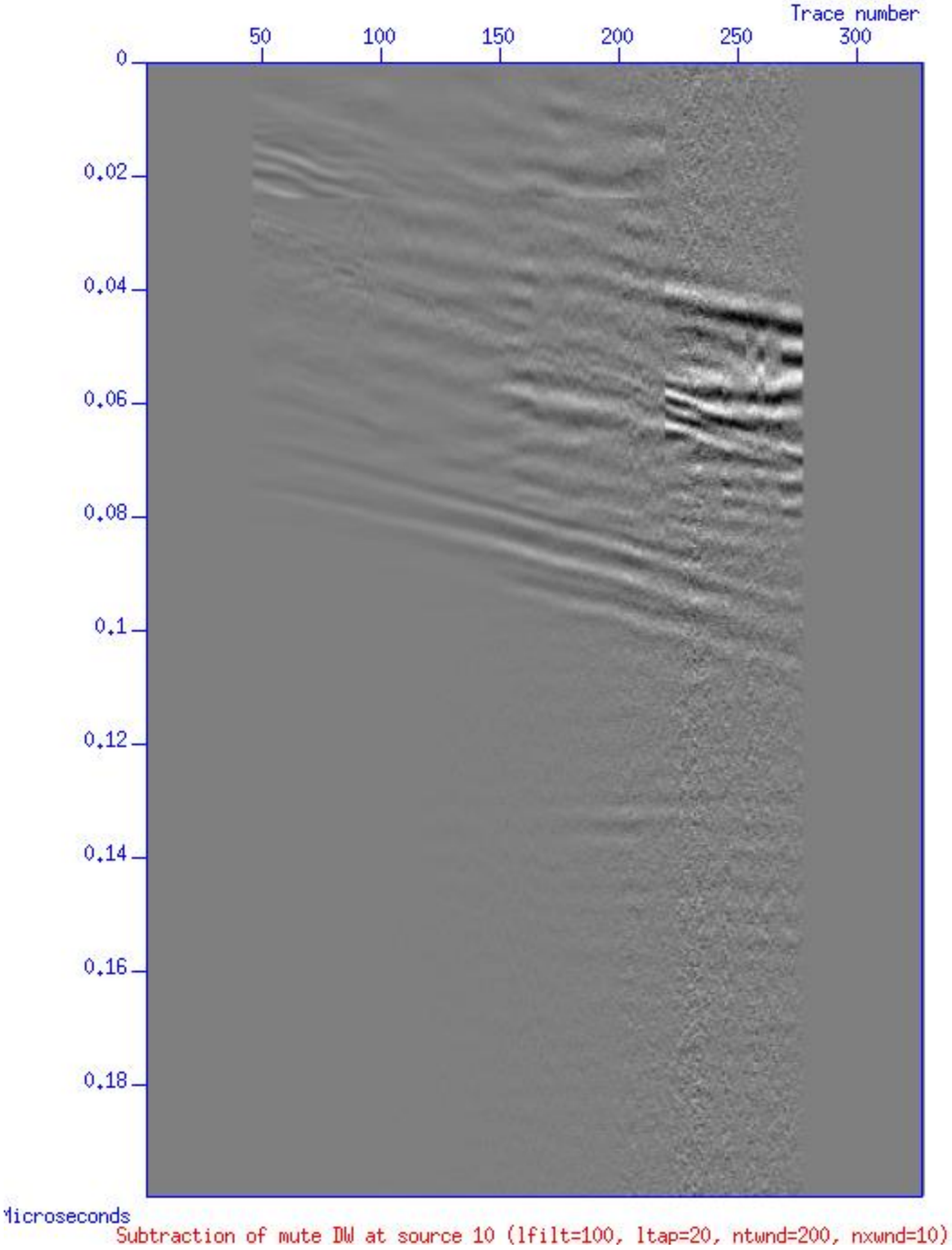

Figure C.17: Subtraction result using parameters lfilt=100, ltap=20, ntwnd=200, nxwnd=10.

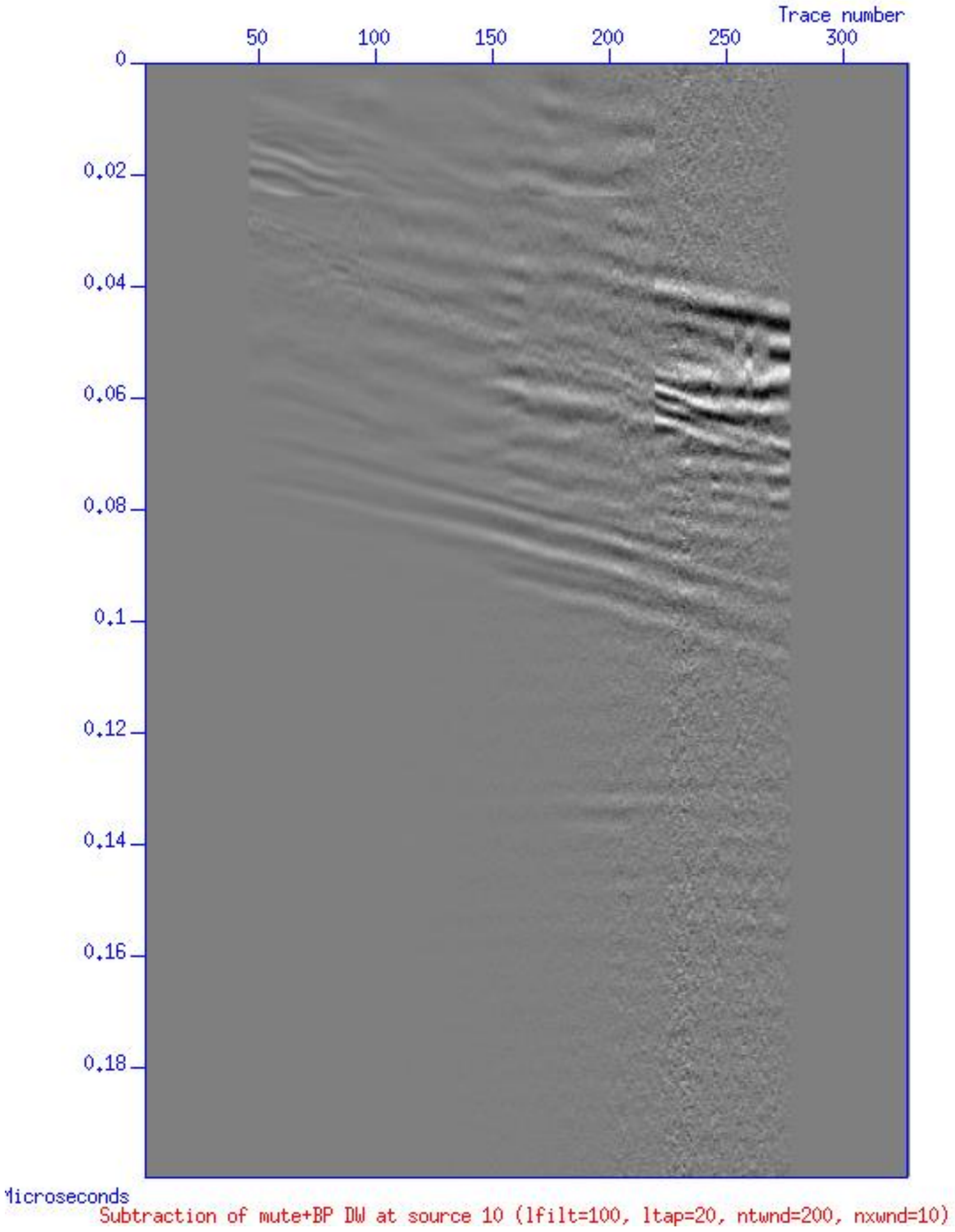

Figure C.18: Subtraction result using parameters lfilt=100, ltap=20, ntwnd=200, nxwnd=10.

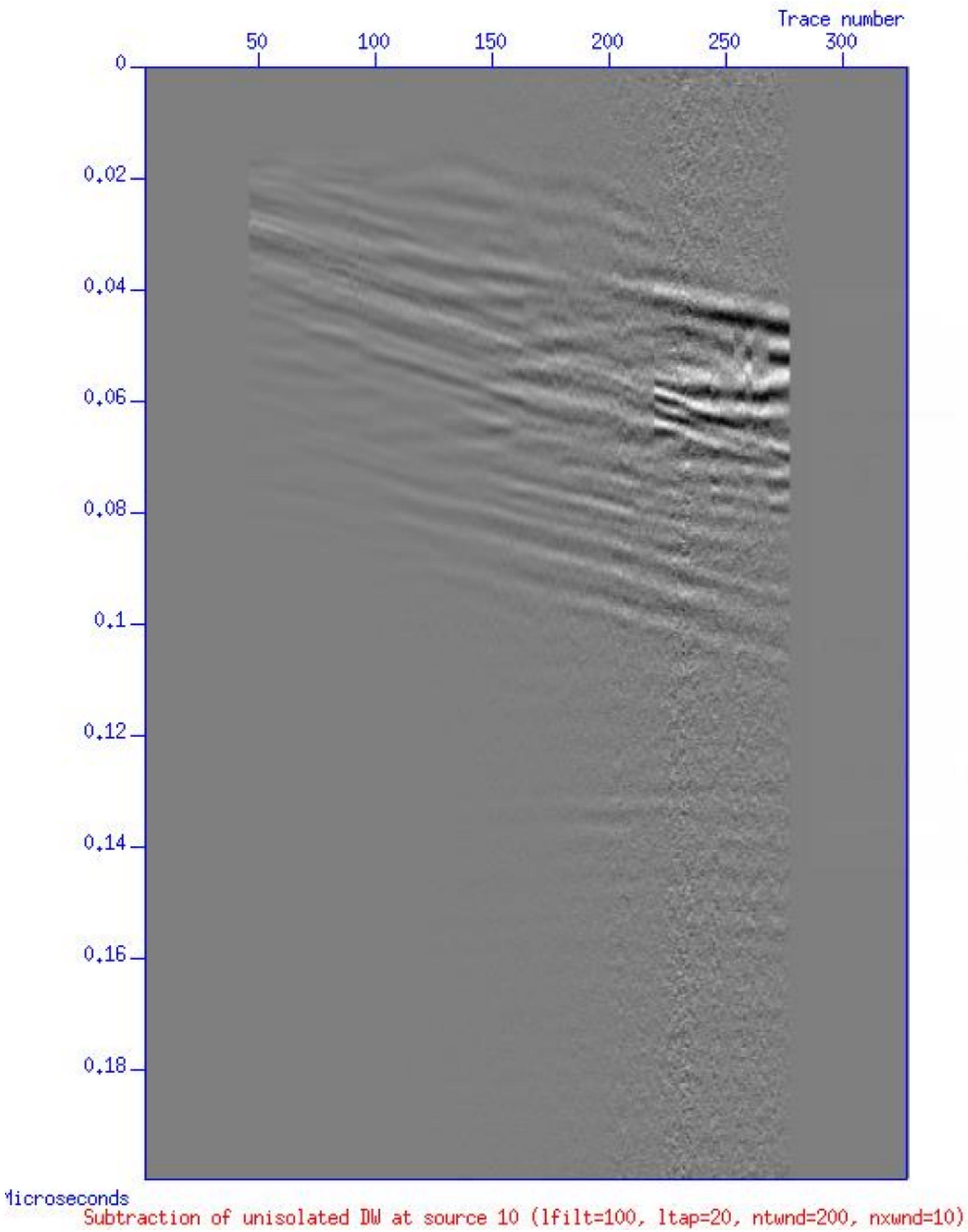

Figure C.19: Subtraction result using parameters lfilt=100, ltap=20, ntwnd=200, nxwnd=10.